



**NUMERICAL STUDIES ON FRETTING FATIGUE  
MODELLING**

**RAPHAEL ARAÚJO CARDOSO**

**TESE DE DOUTORADO EM CIÊNCIAS MECÂNICAS  
DEPARTAMENTO DE ENGENHARIA MECÂNICA**

**FACULDADE DE TECNOLOGIA  
UNIVERSIDADE DE BRASÍLIA**

UNIVERSIDADE DE BRASÍLIA  
FACULDADE DE TECNOLOGIA  
DEPARTAMENTO DE ENGENHARIA MECÂNICA

TESE DE DOUTORADO EM CIÊNCIAS MECÂNICAS

**NUMERICAL STUDIES ON FRETTING FATIGUE  
MODELLING**

**RAPHAEL ARAÚJO CARDOSO**

**ORIENTADOR: JOSÉ ALEXANDER ARAÚJO**

**COORIENTADOR: DAVID NÉRON**

**PUBLICAÇÃO ENM-DT 59/2019**

**Brasília, 28 de janeiro de 2019**

UNIVERSIDADE DE BRASÍLIA  
FACULDADE DE TECNOLOGIA  
DEPARTAMENTO DE ENGENHARIA MECÂNICA

## TESE DE DOUTORADO EM CIÊNCIAS MECÂNICAS

### NUMERICAL STUDIES ON FRETTING FATIGUE MODELLING

**RAPHAEL ARAÚJO CARDOSO**

Tese de doutorado submetida ao Departamento de Engenharia Mecânica da Faculdade de Tecnologia da Universidade de Brasília como parte dos requisitos para a obtenção do título de Doutor.

#### **Banca Examinadora**

Prof. José Alexander Araújo, D.Phil.	(orientador)
Prof. David Néron, Ph.D.	(coorientador)
Prof. Sylvie Pommier, Ph.D.	(examinadora)
Prof. Anthony Gravouil, Ph.D.	(examinador)
Prof. Jaime Tupiassú Pinho de Castro, Ph.D.	(examinador)
Prof. Hachmi Ben Dhia, Ph.D.	(examinador)
Prof. Thiago de Carvalho Rodrigues Doca, Ph.D.	(examinador)
Dr. Claudio Montebello, Ph.D.	(examinador)

Brasília, 28 de janeiro de 2019

## FICHA CATALOGRÁFICA

CARDOSO, RAPHAEL ARAÚJO

NUMERICAL STUDIES ON FRETTING FATIGUE MODELLING. [Distrito Federal] 2019.

102p., 210 x 297 mm (ENM/FT/UnB, Doutor, Ciências Mecânicas, 2019)

Tese de Doutorado – Universidade de Brasília. Faculdade de Tecnologia.

Departamento de Engenharia Mecânica.

- |                               |                             |
|-------------------------------|-----------------------------|
| 1. Fadiga por <i>Fretting</i> | 2. X-FEM                    |
| 3. Modelo de Redução de Ordem | 4. Desgaste                 |
| I. ENM/FT/UnB                 | II. Título (ENM-DT 59/2019) |

## REFERÊNCIA BIBLIOGRÁFICA

CARDOSO, R. A., (2019) Numerical studies on fretting fatigue modelling. Tese de doutorado, Publicação ENM-DM 59/2019, Departamento de Engenharia Mecânica, Universidade de Brasília, DF, 102p.

## CESSÃO DE DIREITOS

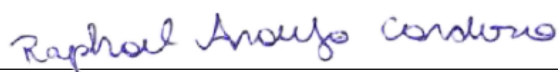
AUTOR: Raphael Araújo Cardoso.

TÍTULO: Numerical studies on fretting fatigue modelling.

GRAU: Doutor

ANO: 2019

É concedida à Universidade de Brasília permissão para reproduzir cópias desta tese de doutorado e para emprestar ou vender tais cópias somente para propósitos acadêmicos e científicos. O autor reserva outros direitos de publicação e nenhuma parte dessa tese de doutorado pode ser reproduzida sem autorização por escrito do autor.



Raphael Araújo Cardoso

Correio Eletrônico: rapha\_2213@hotmail.com

# Resumo

Esse trabalho foi realizado no contexto de uma cooperação de pesquisa internacional entre a Universidade de Brasília, a Agência Espacial Brasileira (AEB), a ENS Paris-Saclay e o grupo SAFRAN. O principal objetivo desta cooperação é a investigação do fenômeno de fadiga por fretting, problema de contato associado a cargas de fadiga que é responsável por reduzir consideravelmente a vida em fadiga de componentes mecânicos devido às elevadas concentrações de tensão, o desgaste e as condições de carregamento não proporcionais envolvidas nestes problemas. Levando-se em consideração o elevado custo computacional presente quando avalia-se aplicações industriais, um dos objetivos deste trabalho é melhorar a performance de simulações de fretting através do uso de uma abordagem de enriquecimento. A ideia é aproveitar-se do fato de que os campos mecânicos ao redor das bordas de contatos cilíndricos sob condições de fretting são similares aqueles encontrados nas proximidades da ponta da trinca em problemas de mecânica da fratura linear elástica. Essa semelhança torna atrativa a ideia de enriquecer simulações de fretting via elementos finitos fazendo-se o uso do X-FEM (Método dos Elementos Finitos Estendidos), que permite o uso de malhas mais grosseiras enquanto se mantém uma boa precisão dos resultados. Como será mostrado neste trabalho, fazendo-se o uso da técnica de enriquecimento é possível trabalhar com malhas até 10 vezes mais grosseiras quando comparadas com o método dos elementos finitos convencional, o que permite uma forte melhora na performance computacional.

Esse trabalho também investigará a influência de se considerar os efeitos do desgaste na predição da vida em fadiga sob condições de fretting. Portanto, simulações de fretting via método dos elementos finitos foram conduzidas considerando a atualização das superfícies de contato devido a remoção de material e os resultados foram comparados com dados experimentais e simulações onde o efeito de desgaste é desprezado (hipótese simplificadora comumente adotada quando avalia-se problemas de fadiga por fretting). Critérios convencionais de fadiga multiaxial associados à Teoria das Distâncias Críticas foram utilizados a fim de estimar vida. Os resultados mostraram que, para os dados investigados, onde ensaios de fretting foram conduzidos em uma liga Ti-6Al-4V sob condições de escorregamento parcial, considerar o desgaste nas análises pode ligeiramente melhorar a precisão nas estimativas de vida. Entretanto, essa ligeira melhora pode não ser justificável ao se considerar os elevados custos computacionais quando comparado com abordagens padrões onde o efeito de desgaste é desprezado.

# Abstract

This work has been undertaken in the context of an international research cooperation between the University of Brasilia, the Brazilian Space Agency (AEB), the ENS Paris-Saclay and the SAFRAN group. The main subject of this cooperation is the investigation of fretting fatigue, which is a contact problem in conjunction with fatigue loads responsible for reducing considerably components' fatigue life due to the high stress concentration, wear and non-proportional loading conditions involved in such problems. Regarding the high computational costs involved when assessing industrial applications, one of the aims of this work is to improve the performance of fretting simulations making use of an enrichment approach. The idea is to take advantage of the fact that the mechanical fields around the contact edges in cylindrical contact configurations under fretting conditions are similar to the ones found close to the crack tip in linear elastic fracture mechanics problems. This similarity makes attractive the idea of enriching finite element fretting simulations through the X-FEM framework, which enables us to work with coarser meshes while keeping a good accuracy. As it will be shown in this work, it is possible to work with meshes up to 10 times coarser than it should be if a conventional FE method was used allowing a strong improvement of the computational performances.

This work will also investigate the influence of considering wear effects in the prediction of fretting fatigue lives. Therefore, fretting fatigue FE simulations have been carried considering the geometry update due to the material removal and results were compared to both experimental data and FE simulations where wear effects were neglected (simplifying strategy usually adopted when evaluating fretting fatigue problems). Conventional multiaxial fatigue criteria in association with the Theory of Critical Distances have been used in order to predict life. Results have shown that, for the data here assessed, where fretting fatigue tests were conducted on a Ti-6Al-4V alloy under partial slip conditions, considering wear effects might slightly increase the accuracy of life predictions. However, this slight improvement may not be worthwhile regarding the increase in the computational cost when compared to standard approaches where wear is neglected.

# Acknowledgements

I would like to acknowledge the financial support of Safran Aircraft Engines to this project in the context of the international research group COGNAC. I also would like to acknowledge the scholarship granted by the Brazilian National Council for Scientific and Technological Development (CNPq) and the Brazilian Aerospace Agency (AEB), specially professor Carlos Alberto Gurgel Veras the Director of the AEB. Thanks as well for the last year of funding provided by the The Coordenação de Aperfeiçoamento de Pessoal de Nível Superior (CAPES).

In addition, I am sincerely thankful for the support and contributions to my research given by my supervisors David Néron and José Alexander Araújo. Contributions of professor Sylvie Pommier were also relevant to this work.

Last but not least, a few words in order to thanks the unconditional support of my wife, family (specially my mother) and friends over the past three years.

# Publications and Conferences

Cardoso, R.A., Néron, D., Pommier, S., Araújo, J.A. (2018). An enrichment-based approach for the simulation of fretting problems. *Computational Mechanics*, 62(6):1529-1542.

Cardoso, R.A., Doca, T., Néron, D., Pommier, S., Araújo, J.A. (2019). Wear numerical assessment for partial slip fretting fatigue conditions. (**under submission**).

Cardoso, R.A., Néron, D., Pommier, S., Araújo, J.A. (2017). An enrichment-based approach for the simulation of fretting problems. 13ème colloque national en calcul des structures (CSMA), Giens, France.

Cardoso, R.A., Néron, D., Pommier, S., Araújo, J.A. (2018). Simulation of fretting problems through an enrichment-based approach. 13<sup>th</sup> world congress on computational mechanics (WCCM), New York, USA.



# Contents

<b>Contents</b>	<b>i</b>
<b>List of Figures</b>	<b>iv</b>
<b>List of Tables</b>	<b>viii</b>
<b>Nomenclature</b>	<b>ix</b>
<b>1 Introduction</b>	<b>1</b>
<b>2 Literature review</b>	<b>5</b>
2.1 Fretting fatigue . . . . .	5
2.2 Numerical modelling of fretting fatigue . . . . .	7
2.3 Fretting fatigue experimental testing . . . . .	8
2.4 Wear aspects in the context of fretting fatigue . . . . .	11
2.5 Fatigue of materials . . . . .	12
2.5.1 Crack initiation and propagation . . . . .	13
2.5.2 Wöhler diagram . . . . .	13
2.5.3 Uniaxial fatigue and the influence of the mean stress . . . . .	14
2.5.4 Miner linear cumulative damage law . . . . .	15
2.5.5 Multiaxial fatigue . . . . .	16
2.6 Theory of critical distances (TCD) . . . . .	20
2.7 Basic contact mechanics . . . . .	21
2.7.1 Surface tractions distributions . . . . .	22
2.7.2 Bulk load effect on the shear traction distribution . . . . .	25
2.7.3 Sub-surface stress distributions . . . . .	26
<b>3 A new multiscale approach for the simulation of fretting problems</b>	<b>28</b>

3.1	Reduced basis (spatial modes) and crack analogy . . . . .	28
3.2	Enrichment technique . . . . .	33
3.3	Contact aspects . . . . .	35
3.3.1	Penalty method . . . . .	37
3.3.2	Lagrange multipliers method . . . . .	38
3.3.3	Contact formulation adopted in this chapter . . . . .	39
3.4	Results and discussions . . . . .	43
3.4.1	Fretting under partial slip conditions . . . . .	43
3.4.2	Enrichment radius sensitivity . . . . .	48
3.4.3	Fretting under gross slip conditions . . . . .	48
3.4.4	Contact status identification through nonlocal intensity factors . . .	50
3.4.5	PGD strategy to enhance performance . . . . .	53
3.5	Chapter highlights . . . . .	55
<b>4</b>	<b>Wear effects on fretting fatigue life estimate</b>	<b>56</b>
4.1	Contextualization . . . . .	56
4.2	Wear numerical modelling and damage accumulation . . . . .	56
4.3	Contact surface update . . . . .	58
4.4	Experimental data available . . . . .	66
4.5	Finite element modelling of wear . . . . .	68
4.6	Multiaxial fatigue life assessment . . . . .	69
4.7	Results . . . . .	72
4.8	Chapter highlights . . . . .	78
<b>5</b>	<b>Conclusion and perspectives</b>	<b>79</b>
5.1	Main conclusions . . . . .	79
5.2	Suggestions for future work . . . . .	80
	<b>Bibliography</b>	<b>82</b>
	<b>Appendix A Velocity fields and spatial reference fields computation</b>	<b>93</b>
	<b>Appendix B Proper orthogonal decomposition</b>	<b>95</b>
	<b>Appendix C Enrichment technique formulation</b>	<b>98</b>

<b>Appendix D Maximum Rectangular Hull (MRH)</b>	<b>102</b>
--	------------

# List of Figures

- 1.1 Dovetail joint in an aeronautical LEAP engine (Safran Aircraft Engines). . . . . 2
- 1.2 Micro-slip spectrum during a flight. . . . . 2
- 1.3 Cylinder-plane configuration often used to assess the fretting fatigue phenomenon. . . . . 2
  
- 2.1 Fretting map: wear (thick line) and fatigue life as function of slip amplitude (Vingsbo and Söderberg, 1988). . . . . 6
- 2.2 Fretting fatigue test configurations: (a) bridge pads, (b) cylindrical pads. . . . . 8
- 2.3 Dovetail fretting fatigue apparatus. . . . . 9
- 2.4 Failed blade specimen from the biaxial dovetail apparatus (Rajasekaran and Nowell, 2006). . . . . 9
- 2.5 Schematic view of the fretting fatigue apparatus with two independent actuators at the University of Brasilia. . . . . 10
- 2.6 Fretting fatigue apparatus with only one actuator at the University of Brasilia. . . . . 11
- 2.7 Illustration of the crack initiation/propagation process. . . . . 13
- 2.8 Typical S-N curves. . . . . 14
- 2.9 Schematic representation of Haigh diagram for a constant life. . . . . 15
- 2.10 Loading history at different stress levels. . . . . 16
- 2.11 Modified Wöhler curves. . . . . 18
- 2.12 Material plane  $\Delta$  and stress vector decomposition. . . . . 19
- 2.13 Different definitions for the shear stress amplitude, adapted from (Castro et al., 2009): (a) Minimum Radius Circle; (b) Minimum F-norm Ellipse; (c) Maximum Rectangular Hull. . . . . 20
- 2.14 TCD averaging regions in its simplified 2D versions (point,line and area). . . . . 21
- 2.15 Schematic representation of the cylinder on plane contact configuration. . . . . 23
- 2.16 Variation of the tangential load  $Q$  over time. . . . . 24
- 2.17 Shear traction distributions during a tangential cycle,  $Q_{max}/\mu P = 0.6$ . . . . . 24

2.18	Shear traction distributions during a fretting cycle, $Q_{max}/\mu P = 0.6$ and $\sigma_{b,max}/\mu p_0 = 0.8$ . . . . .	26
3.1	Analogy between complete contact under fretting condition (a) and double-edge cracked plate (b). . . . .	29
3.2	FE model used to extract the spatial modes and the nonlocal intensity factors. . . . .	30
3.3	(a) Comparison between the radial evolution of $\underline{d}^s$ and the radial evolution of the displacement field nearby a crack tip (mode I), (b) Comparison between the angular evolution of $\underline{d}^s$ and the angular evolution of the displacement field nearby a crack tip (mode I). . . . .	31
3.4	(a) Comparison between the radial evolution of $\underline{d}^a$ and the radial evolution of the displacement field nearby a crack tip (mode II), (b) Comparison between the angular evolution of $\underline{d}^a$ and the angular evolution of the displacement field nearby a crack tip (mode II). . . . .	32
3.5	Comparison of $\underline{g}^a(\theta)$ for different geometries obtained varying the pad radius. . . . .	32
3.6	Enrichment scheme. . . . .	35
3.7	Contact problem two deformable bodies. . . . .	36
3.8	Local contact formulation. . . . .	37
3.9	LATIN scheme. . . . .	40
3.10	(a) Fretting model under partial slip, (b) fretting under partial slip load history. . . . .	44
3.11	Directions of stress evaluation. . . . .	44
3.12	Reference solution of the fretting problem: (a) FE model and von Mises contour at $u_x = u_{x,max}$ , (b) comparison between analytical and reference solution of the problem investigated for the $\sigma_{xy}$ stress component along the contact surface ( $u_x = u_{x,max}$ ). . . . .	45
3.13	Gauss points integration scheme. . . . .	46
3.14	(a) $\sigma_{xx}$ stress component ( $y = 0, u_x = u_{x,max}$ ), (b) $\sigma_{xy}$ stress component ( $y = 0, u_x = u_{x,max}$ ). . . . .	46
3.15	(a) $\sigma_{xx}$ stress component ( $x = -a, y < 0, u_x = u_{x,max}$ ), (b) $\sigma_{xy}$ stress component ( $x = -a, y < 0, u_x = u_{x,max}$ ). . . . .	46
3.16	(a) numerical error expressed by means of the size of mesh, (b) numerical error expressed by means of the elapsed time in each simulation. . . . .	47
3.17	Variation of $\sigma_{xx}$ when $u_x = u_{x,max}$ against distance from the surface ( $x/a = -1$ ) for different enrichment radii. . . . .	48
3.18	(a) Prescribed displacement history in gross slip, $\sigma_{xy}$ stress component at time steps (b) A, (c) B, (d), C and (e) D. . . . .	49

3.19	(a) Prescribed displacement history used to check the nonlocal intensity factors behaviour under gross slip conditions, (b) contact slip zone semi-width over time, (c) nonlocal intensity factors evolution over time, (d) $ I^a / I^s $ over time. . . . .	51
3.20	$\sigma_{xy}$ stress component along the contact surface for different time steps when gross slip is predominantly observed. . . . .	52
3.21	Reference frame PGD description. . . . .	54
3.22	PGD error in terms of the number of functional pairs. . . . .	54
4.1	Illustration of the methodology used in order to transfer the cumulative damage from a previous fretting cycle simulation to the next. . . . .	58
4.2	FE-based model for wear analysis using the remeshing technique. . . . .	59
4.3	FE-based model for wear analysis using the ALE adaptive technique. . . . .	60
4.4	FE model used to validate wear implementations. . . . .	61
4.5	Contact pressure distributions under partial slip conditions ( $P = 120$ N/mm, $u_x = 2.5 \mu\text{m}$ , $R = 6$ mm) for different number of fretting cycles: (a) considering the remeshing technique and (b) the adaptive mesh. . . . .	62
4.6	Contact pressure distributions under partial slip conditions for different number of fretting cycles (Ding et al., 2004). . . . .	62
4.7	Contact pressure distributions under gross sliding conditions ( $P = 120$ N/mm, $u_x = 10 \mu\text{m}$ , $R = 6$ mm) for different number of fretting cycles: (a) considering the remeshing technique and (b) the adaptive mesh. . . . .	63
4.8	Contact pressure distributions under gross conditions sliding for different number of fretting cycles (Ding et al., 2004). . . . .	64
4.9	Worn profile under partial slip conditions ( $P = 120$ N/mm, $u_x = 2.5 \mu\text{m}$ , $R = 6$ mm): (a) pad, (b) specimen. . . . .	65
4.10	Worn profile under gross sliding conditions ( $P = 120$ N/mm, $u_x = 10 \mu\text{m}$ , $R = 6$ mm): (a) pad, (b) specimen. . . . .	65
4.11	Schematic representation of the Group-2 tests: (a) Group-2a tests with the same slip zone areas for different contact widths, (b) Group-2b tests with different slip zone areas. . . . .	67
4.12	Finite element model used in order to carry out fretting fatigue/wear simulations. . . . .	68
4.13	Comparison between analytical and FE solution: (a) pressure and (b) shear traction distribution (loading conditions from test T2 in Table 4.1). . . . .	69
4.14	Uniaxial fatigue data for the Ti-6Al-4V (Kallmeyer et al., 2002). . . . .	70
4.15	Uniaxial fatigue data for the Ti-6Al-4V (Kallmeyer et al., 2002) expressed in terms of the SWT parameter. . . . .	70

4.16 Uniaxial fatigue data for the Ti-6Al-4V (Kallmeyer et al., 2002) expressed in terms of the Findley parameter. . . . .	71
4.17 Uniaxial fatigue data for the Ti-6Al-4V (Kallmeyer et al., 2002) expressed in terms of the MWCM. . . . .	71
4.18 Specimen’s worn profile for different number of fretting fatigue cycles considering loading conditions from test T1. . . . .	72
4.19 Contact traction distribution for different number of fretting fatigue cycles considering loading conditions from test T1: (a) pressure ( $Q(t) = 0$ ) and (b) shear traction ( $Q(t) = Q_{max}$ ). . . . .	73
4.20 TCD applied to fretting problems when wear effects are neglected. . . . .	74
4.21 TCD applied to fretting problems when wear is taken into account. . . . .	74
4.22 Estimated and observed fretting fatigue lives reported in (Ferry, 2017). . . . .	76
4.23 Damage distribution inward the contact at $L/2$ for the load configuration T1: (a) considering and (b) neglecting wear effects. . . . .	77
A.1 Reference frame velocity field computation. . . . .	93
A.2 Spatial fields extracted from FE modelling: (a) $\underline{d}^s$ on the x direction, (b) $\underline{d}^s$ on the y direction, (c) $\underline{d}^a$ on the x direction, $\underline{d}^a$ on the y direction. . . . .	94
B.1 POD application example. . . . .	97
C.1 Schematic view of the asymptotic fretting enrichment functions. . . . .	98
C.2 Reference frame contact edge. . . . .	99
C.3 Schematic view of the asymptotic fretting enrichment functions. . . . .	101
D.1 Maximum Rectangular Hull (MRH) method. . . . .	102

# List of Tables

- 2.1 Solutions for  $\gamma$  based on the ratio of fatigue strength for two stress states. . 17
  
- 3.1 Solution of the local stage. . . . . 43
  
- 4.1 Group-2 fretting fatigue data for the Ti-6Al-4V (Ferry, 2017) (pad radius  $R = 70$  mm). . . . . 66
- 4.2 Mechanical properties of the Ti-6Al-4V alloy (Le Biavant-Guerrier, 2000). . 68
- 4.3 Life estimates considering wear effects. . . . . 75
- 4.4 Life estimates neglecting wear effects. . . . . 75
- 4.5 Estimated errors considering (a) and neglecting wear effects (b). . . . . 76



# Nomenclature

$\underline{d}^s$ : symmetric spatial reference field,  
 $\underline{d}^a$ : antisymmetric spatial reference field,  
 $\underline{d}^c$ : complementary spatial reference field,  
 $I^s$ : Intensity factor (symmetric part),  
 $I^a$ : Intensity factor (antisymmetric part),  
 $I^c$ : Intensity factor (complementary part),  
 $\underline{v}$ : velocity field expressed in the reference frame attached to the contact edge,  
 $P$ : normal force applied to the cylindrical pad,  
 $Q$ : fretting tangential force applied to the cylindrical pad,  
 $F_b$ : bulk fatigue load applied to the rectangular specimen,  
 $\underline{u}$ : displacement field,  
 $u_x$ : tangential displacement imposed on the cylindrical pad,  
 $u_y$ : vertical displacement imposed on the cylindrical pad,  
 $u_{x,max}$ : maximum tangential displacement applied to the cylindrical pad,  
 $f(r)$ : radial evolution of the spatial reference field,  
 $\underline{g}$ : tangential evolution of the spatial reference field,  
 $\underline{\underline{\sigma}}$ : Cauchy stress tensor,  
 $\underline{\underline{\varepsilon}}$ : small deformation strain tensor,  
 $\underline{f}_{ext}$ : external tractions applied to a body,  
 $\underline{f}_c$ : contact tractions,  
 $g_0$ : Initial normal gap between two bodies,  
 $g_N$ : normal gap function,  
 $g_T$ : tangential gap function,  
 $\epsilon_N$ : normal penalty parameter,  
 $\epsilon_T$ : tangential penalty parameter,  
 $N_i$ : finite element interpolation function,  
 $\chi$ : Lagrange multiplier interpolation function,  
 $\psi$ : enrichment function,  
 $r_e$ : enrichment radius,  
 $\beta$ : singularity order,  
 $a$ : semi-width contact zone,  
 $c$ : semi-width contact stick zone,  
 $p_0$ : contact peak pressure,  
 $\mu$ : Coulomb friction coefficient,  
 $\tilde{\mu}$ : nonlocal Coulomb friction coefficient,  
 $\underline{w}$ : displacement field on the contact surface,  
 $\underline{\lambda}$ : Lagrange multiplier field,  
 $\kappa$ : search direction parameter,

$\zeta$ : stabilization parameter,  
 $S$ : total relative slip between contacting surfaces,  
 $V$ : volume,  
 $K$ : Archard's dimensionless wear coefficient,  
 $H$ : hardness of the contacting surfaces,  
 $\alpha$ : friction wear coefficient,  
 $\kappa_w$ : Archard's local wear coefficient,  
 $h$ : local wear depth,  
 $s$ : local relative slip between contacting surfaces,  
 $E_d$ : friction energy dissipated during a fretting cycle,  
 $\sigma_a$ : stress amplitude,  
 $\sigma_m$ : mean stress,  
 $\sigma_y$ : yield stress,  
 $\sigma_{ut}$ : ultimate stress,  
 $E$ : Young modulus,  
 $\nu$ : Poisson's ratio,  
 $R_\sigma$ : stress ratio,  
 $\tau_a$ : shear stress amplitude,  
 $\sigma_{n,max}$ : maximum normal stress,  
 $\sigma'_f$ : fatigue strength coefficient,  
 $b'$ : fatigue strength exponent,  
 $\varepsilon'_f$ : fatigue ductility coefficient,  
 $d'$ : fatigue ductility exponent,  
 $I_{FP}$ : Findley multiaxial fatigue parameter,  
 $I_{SWT}$ : Smith, Watson and Topper multiaxial fatigue parameter,  
 $I_{MWCM}$ : Modified Wöhler Curve Method fatigue parameter,  
 $\rho$ : multiaxial stress ratio,  
 $\gamma$ : material parameter of Findley's multiaxial fatigue model,  
 $\kappa_\tau$ : inverse of the slope of the modified Wöhler curves,  
 $\Delta\varepsilon_n$ : normal strain range,  
 $N_f$ : number of cycles to failure,  
 $L$ : critical distance,  
 $\sigma_b$ : bulk stress,  
 $A_{th}^s$ : theoretical area of the slip zones,  
FE: Finite Element,  
FEM: Finite Element Method,  
LEFM: Linear Elastic Fracture Mechanics,  
MWCM: Modified Wöhler Curve Method,  
PGD: Proper Generalized Decomposition,  
POD: Proper Orthogonal Decomposition,  
SWT: Smith, Watson and Topper,  
X-FEM: Extended Finite Element Method.

# Chapter 1

## Introduction

This work is settled in the context of the COGNAC project (**CO**mpetition between the **G**radient effect and the scale effect in **NO**tch fatigue **AND** **C**ontact fatigue), which was proposed and conceived by Snecma, part of the SAFRAN group. This work is also supported by the Brazilian Space Agency (AEB). In this framework, the aim of the research carried out here is to improve the numerical capabilities of performing fretting simulations.

Fretting occurs when two or more mechanical components come into contact and at least one of them is subjected to vibration loads inducing micro-slip between the contact surfaces. This damage phenomenon, known as fretting, may speed up the nucleation of short cracks in the vicinity of the contact surfaces. In practical situations, if those components are also subjected to bulk fatigue loads, some of these cracks may propagate leading to failure by fretting fatigue (Hills and Nowell, 1994).

The fretting fatigue problem is of great importance, for instance, within the aerospace industry. Figure 1.1 depicts the dovetail connection between blades and discs in aircraft engines. In this case, the centrifugal load and the vibrations due to the aeroelastic interactions provide fretting fatigue conditions. A simplified spectrum of the micro-slip experienced by the dovetail connection during a flight is presented in Figure 1.2. In this case, we can observe low-cycle fatigue during take-off and landing phases as well as high-cycle fatigue during the cruise phase. Despite the complexity of the problem presented in Figure 1.1, in practice, simplified contact configurations as the cylinder-plane one (see (Munoz et al., 2006; Rossino et al., 2009; de Pannemaecker et al., 2015)) are assessed experimentally in order to obtain better understanding about the fretting-fatigue phenomenon. In the case of a cylinder-plane contact configuration, Figure 1.3, a normal load,  $P$ , is applied to the cylindrical pad while the specimen is fixed on the bottom. After that, a tangential load,  $Q(t)$ , is applied to the pad ensuring fretting conditions. In case of fretting fatigue, the specimen is also subjected to a fatigue bulk load,  $F_b(t)$ , that is not necessarily in phase with the tangential load. We can also see in Figure 1.3, the level of refinement required in such problems when numerical simulations are performed which leads to high CPU costs.

Over the years, various methodologies have been proposed in order to design safe components against fretting fatigue. Some of these methodologies are based on the evaluation of a nonlocal representative stress/strain tensor, which can be further used inside classical

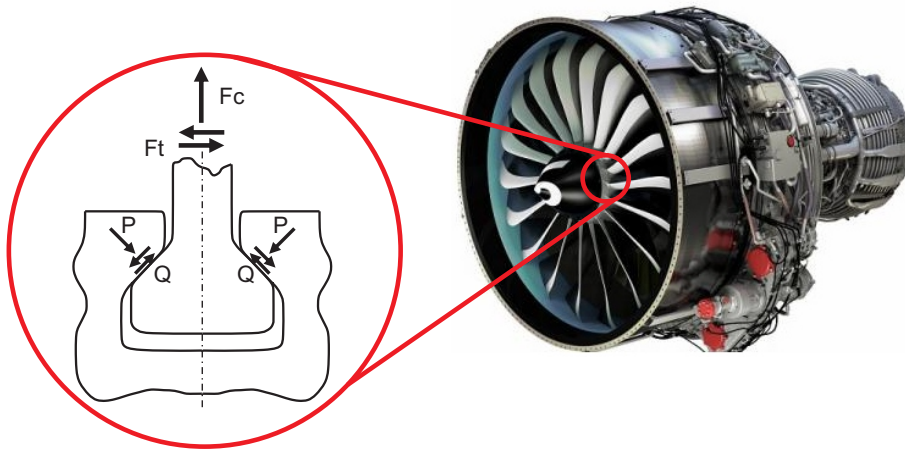


Figure 1.1: Dovetail joint in an aeronautical LEAP engine (Safran Aircraft Engines).

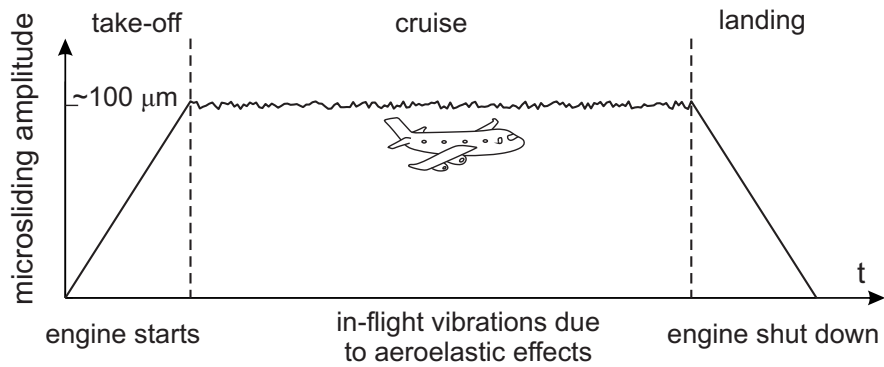


Figure 1.2: Micro-slip spectrum during a flight.

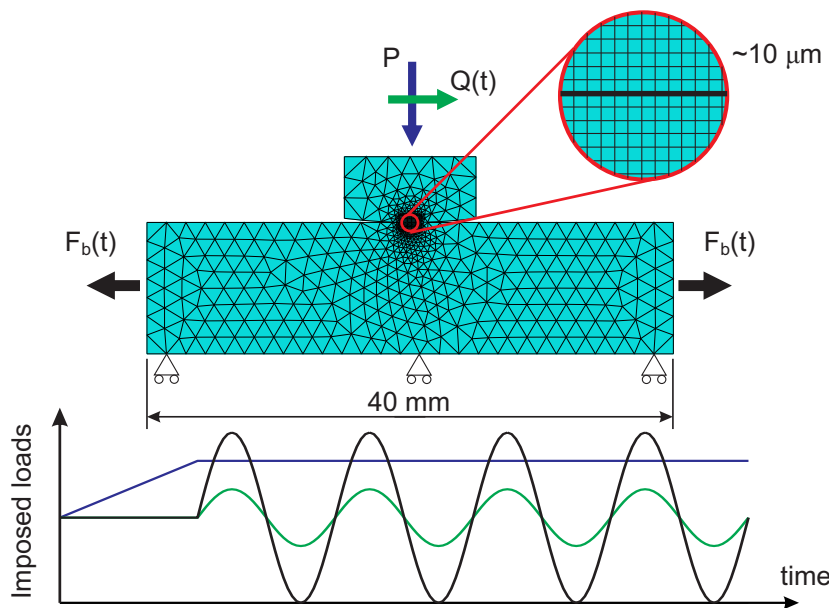


Figure 1.3: Cylinder-plane configuration often used to assess the fretting fatigue phenomenon.

---

multiaxial fatigue criteria (Araújo et al., 2007, 2008; Fouvry et al., 2014). Another common approach is to check if a short crack after being initiated will arrest or not through LEFM approaches (Araújo and Nowell, 1999; Fouvry et al., 2008; Dini et al., 2006). The main concern with the previous approaches is that all of them require simulations with fine meshes (even a few microns, Figure 1.3) in order to capture the strong stress gradient nearby the contact surfaces. The elements size in these refined meshes is often much smaller than the global characteristic dimension of the problem studied.

In an attempt to overcome this issue, recently, Montebello et al. (Montebello et al., 2016) proposed a new numerical approach capable of capturing the stress gradient effect in fretting fatigue problems through nonlocal intensity factors, which can be computed through a non-intrusive reduced order modelling technique based on LEFM insights. They could also confirm, in a generalized way, the similarity between the mechanical fields found in contact problems with the ones found close to the crack tip in LEFM problems as previously suggested by (Giannakopoulos et al., 1998, 2000).

In this setting, one of the ideas behind this work is to enrich fretting simulations performed on coarse meshes through the X-FEM method, once that, as it has been shown in (Montebello et al., 2016), the kinematic fields around the contact edges in cylindrical contact problems under fretting conditions resemble the kinematic fields around the crack tip in fracture mechanics problems. The idea of using the X-FEM technique in the context of the simulation of fretting problems has been already the subject of several works (see e.g. (Giner et al., 2008a, 2009; Pierres et al., 2011; Baietto et al., 2013)). In these works, the aim was to simulate crack growth under fretting conditions. In addition, it will not be the first time that the partition of unity framework is applied to enrich the mechanical fields arising from contact problems. The numerical modelling of complete sliding contact was carried out through the partition of unity by (Giner et al., 2008b). As in such complete contact problems there are strong singularities in the contact corners, the authors have used the X-FEM to enrich the displacement field nearby these critical zones. Besides that, a domain integral formulation was adopted to compute a generalized stress intensity factor (Fuenmayor et al., 2005).

This work also intends to verify the influence of considering wear effects when estimating fretting fatigue lives. Over the last decades, many efforts have been made in an attempt to understand better the mechanisms of failure present in fretting fatigue problems. Recently, some authors (McColl et al., 2004; Ding et al., 2004; Madge et al., 2007a,b; Cruzado et al., 2013; Garcin et al., 2015) have tried to verify the influence of the material removal due to wear when assessing fretting fatigue. The key point here is that, most of the multiaxial fatigue models commonly considered in order to evaluate fretting problems so far are stress-strain based. Consequently, the sub-surface stress modifications due to wear may lead to completely different results in terms of life estimates mainly under gross sliding conditions. Therefore, in this work, classical multiaxial fatigue criteria will be used to estimate fretting fatigue life on a Ti-6Al-4V alloy where all the experimental data assessed was conducted under partial slip conditions (Ferry, 2017). Life prediction will be carried out considering wear effects, where the contact/sub-surface stress modifications demands the use of a cumulative damage law. Results will be compared to both standard fretting fatigue simulations where wear is neglected and with experimental data. At the end, the idea is to verify whether under partial slip regime wear needs to be taken into account or not (simplifying approach adopted in most of the work in the fretting research field (Szolwinski and Farris, 1996; Araujo and Nowell, 2002; Hattori et al., 2003; Araujo

et al., 2004; Sum et al., 2005; Navarro et al., 2008; Fouvry et al., 2014; Araújo et al., 2017).).

The remaining of this manuscript is organized as follows:

- **Chapter 2:** The fretting fatigue problem is introduced. A historical review of the main research progress in the field over the last decades is presented as well. In addition, this chapter also addresses the following aspects: fretting fatigue experimental apparatus, wear, fatigue of materials and basic contact mechanics.
- **Chapter 3:** A new computational approach for the simulation of fretting problems is introduced, where it aims to reduce the computational costs involved when solving such problems. In this case, taking advantage of the crack analogue approach discussed in (Montebello et al., 2016), an enrichment technique is used in order to enhance the quality of the results in the context of FE simulations when using coarser meshes. For so, the X-FEM is used to enrich the displacement field discretization close to the contact edges in fretting problems.

This chapter ends with a comparison between standard and enriched FE simulations for both partial and gross sliding conditions. This intends to verify the improvements in the quality of the results as well as the decrease in the computational cost when using the enrichment strategy here investigated.

- **Chapter 4:** This chapter investigates the effects of considering the material removal due to wear when estimating fretting fatigue lives. The FE computational strategy used to update the contacting surfaces as wear evolves as well as the procedure used to evaluate the fatigue damage over the fretting cycles are also presented in this chapter.

In the end of the chapter, fatigue life estimates considering and neglecting wear are compared with experimental data for the Ti-6Al-4V titanium alloy. In this case, only tests under partial slip conditions are considered.

- **Chapter 5:** The main conclusions draw on this thesis are highlighted. Suggestion for future work are also addressed in this chapter.

# Chapter 2

## Literature review

### 2.1 Fretting fatigue

The phenomenon so-called fretting has been considerably studied over the last century. The first recorded reference in the literature seems to be in the paper of Eden et al. (Eden et al., 1911), published in 1911. Fretting was identified by the presence of oxide debris on the surface of the steel grips in contact with plain fatigue specimens. The first actual investigation of the fretting process was carried out by Tomlinson (Tomlinson, 1927). He associated this phenomenon to very small relative tangential displacements on the contact surface between materials. Later, more systematic investigations of fretting fatigue showed that specimens previously subjected to fretting conditions, presented fatigue strength reductions (14 – 17%) (Warlow-Davies, 1941). Further studies conducted by (McDowell, 1952), pointed out that combined effects of fretting and fatigue could reduce material fatigue strength by factors ranging from 2 to 5 or even more. However, it is worth mentioning that only after late 1960's more systematic investigations of parameters such as contact pressure, relative tangential displacement, contact size, fretting wear, environment conditions and stress concentration on fretting fatigue were conducted, where (Nishioka and Hirakawa, 1969a,b,c,d; Nishioka and Kenji, 1972) analysed independently many of these factors. One of the main conclusions was the small influence of the frequency of the cyclic loading on the fretted specimens lives. They could also observe the presence of non-propagating cracks in some of the fretting fatigue experiments, leading to conclude that although fretting may collaborate to crack initiation, other parameters may influence the crack arrest. The influence of the relative slip between the surfaces was also verified in their study, showing that in a range from  $5\mu m$  to  $50\mu m$  fatigue strength was reduced while above  $50\mu m$  of slip displacement fatigue cracks were not observed, probably because in these cases the role played by the wear was too strong and cracks were worn out as soon as they initiated. This behaviour was later evaluated by (Vingsbo and Söderberg, 1988), Figure 2.1. Besides those features, in (Nishioka and Hirakawa, 1969b) the cracks were noticed to initiate in the high stress zones close to the contact edges and propagate entering the region behind the contact zone. In (Nishioka and Hirakawa, 1969c) they observed that the mean bulk stress applied to specimens had not great effects on the fretting fatigue life.

In the 1970's, a number of different approaches aiming to design against fretting

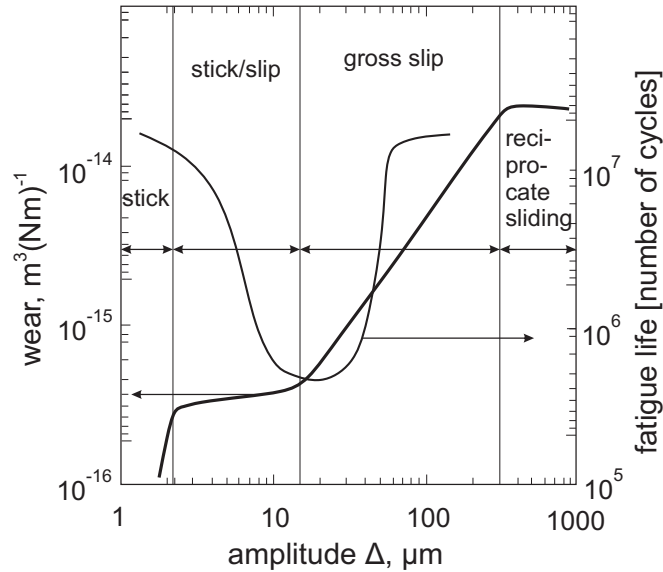


Figure 2.1: Fretting map: wear (thick line) and fatigue life as function of slip amplitude (Vingsbo and Söderberg, 1988).

fatigue were proposed. In (Gordelier and Chivers, 1979) a literature review of palliatives for fretting fatigue as surface treatments, coatings, shims and friction reduction is carried out. A few authors have also focused on stress concentration effects as in (Wright and O'Connor, 1972). In 1973, Bramhall (Bramhall, 1973) performed a study where he varied the size of the contact zone in fretting fatigue tests while keeping constant the contact peak pressure. He could observe that for a certain critical contact size, the fatigue life of the tests were significantly reduced, which he attributed to the stress gradient effect. Small contacts have steeper stress decays, whereas larger contacts have smoother ones for the same levels of surface stress. This behaviour was later confirmed by other authors as (Nowell, 1988; Araújo and Nowell, 1999). Endo and Goto (1976) performed crack growth measurements on mild steel using cylindrical pads under full slip conditions. They showed that cracks initiated on shear planes (stage I) and then quickly started propagating nearly perpendicular to the contact surface (stage II). In their work, it was possible to see that fretting does not only accelerate crack initiation but it also has a great influence on early stages of crack propagation.

Ruiz et al. (1984) proposed a particularly popular method used to predict fretting fatigue performance by the use of empirical parameters formulated purely for the fretting case. Firstly, it was based on the definition of an energy damage parameter defined as the product of the local slip amplitude with the maximum shear traction ( $\tau\delta$ ). A further improvement of this formulation was made by introducing the maximum stress component parallel to the contact surface ( $\sigma\tau\delta$ ). This was found to give better estimations of the location of fretting cracks initiation. Although the physical interpretation of this parameter is not very clear, it often provides a good correlation with experimental observations (Ciavarella et al., 2001).

With the continuous progress in the development of the contact mechanics theory over the last century (Hertz, 1882; Cattaneo, 1938; Muskhelishvili, 1953; Johnson, 1987), analytical results made it possible to obtain precise information about the mechanical fields for



simple geometries commonly utilized to evaluate the fretting fatigue phenomenon. Thanks to that, some authors have started working with different theories to predict fretting fatigue performance, among them, notch analogy (Giannakopoulos et al., 2000; Araújo et al., 2007; Dini et al., 2006), crack analogy (Giannakopoulos et al., 1998; Ciavarella, 2003) and short crack arrest (Araújo and Nowell, 1999; Dini et al., 2006; Fouvry et al., 2008). At this point, it would be nearly impossible to cover all the relevant contributions to the fretting fatigue field over the last years. Therefore, bearing in mind the numerical scope of this thesis, the next section briefly describes some of the relevant works on the simulation of fretting fatigue carried out in the last decades.

## 2.2 Numerical modelling of fretting fatigue

With the advent progress of computational mechanics, the fretting fatigue problem could be better understood through the simulation of more complex and realistic phenomena, for example, Ruiz et al. (1984) conducted an early study involving the application of a 2D finite element analysis to model fretting fatigue in a dovetail joint. Later, Papanikos et al. (1998) came with a 3D nonlinear finite element analysis of the same problem. In (Munoz et al., 2006), under plain fretting conditions, a model which combines both crack nucleation and propagation processes is used to predict the crack extension throughout the life of the component. A finite element sub-modelling method was used to estimate crack propagation life in (Fadag et al., 2008). In (Baietto et al., 2013; Giner et al., 2014) the crack propagation under fretting conditions is simulated through the X-FEM as well as the interactions between the crack faces are taken into account.

Concerning elasto-plastic analysis, Tsai and Mall (2000) investigated a pre-stressed strip with a cylindrical pad. In (Goh et al., 2006) crystallographic plasticity is represented in two-dimensional fretting analyses of Ti-6Al-4V. The relationship between the location of maximum localized plasticity and Ruiz fretting damage parameter with the crack initiation site was carried out in (Talemi and Wahab, 2012). Fretting fatigue life is predicted considering a damage-coupled elastic-plastic constitutive model and wear in (Shen et al., 2015). In (McColl et al., 2004; Ding et al., 2004; Madge et al., 2007a,b; Cruzado et al., 2013; Garcin et al., 2015) fatigue damage assessments were carried out taking into account wear effects (material removal). These works were capable of capturing the increasing effects in fatigue life for gross slip regimes. Ben Dhia and Torkhani (2008) considered a multimodel/multiscale strategy (Arlequin method) in order to model fretting wear. In (Ding et al., 2007; Basseville et al., 2011) wear modelling considering third body interactions were carried out. Yue and Wahab (2017) investigated the influence of the friction coefficient variation in the numerical assessment of fretting problems. The digital image correlation method (DIC) was used to calibrate the friction coefficient in a FE model in (Nesládek et al., 2012). In (Rodríguez-Tembleque et al., 2011) a 3D boundary element method formulation was used to simulate fretting wear under both partial and slip regimes. The boundary element method was also considered in the analysis of a Cattaneo-Mindlin problem in (Cavalcante et al., 2017). The work of Wang et al. (2012) introduced a new rolling contact solver using a semi-analytical method in order to evaluate 3D steady-state rolling contact problems, where creep effects were also included in the analysis.

The numerical modelling of complete sliding contact was carried out through the par-

tition of unity framework by (Giner et al., 2008b). These authors have enriched the displacement field close to the contact edges (XFEM) in order to capture the stress singularities in these regions. Besides, a domain integral formulation was adopted to compute a generalized stress intensity factor (Fuenmayor et al., 2005). More recently, Montebello et al. (2016) proposed a new numerical method to describe the stress gradient effect in fretting problems through an analogy to fracture mechanic problems.

## 2.3 Fretting fatigue experimental testing

Over the years, experimental investigations of fretting fatigue have occurred in many different ways. Initially, due to its simplicity, the contact set-up between a specimen and “bridge” pads was common, Figure 2.2(a), which remained popular until the 1990’s. In such configuration, a regular fatigue specimen can be used, where the fatigue loads can be applied due to cyclic bending or tension. The bridges are clamped to the specimen and the cyclic strain in the specimen provokes the relative motion between the contact parts. Despite its simplicity, this contact configuration brings some difficulties. It is not easy to characterize contact conditions at the pad feet, particularly if bending takes place in the bridge. In general, contact conditions at each foot are not the same and it is likely that one foot slips before the other. In this case, slip regime during the experiment is frequently unknown.

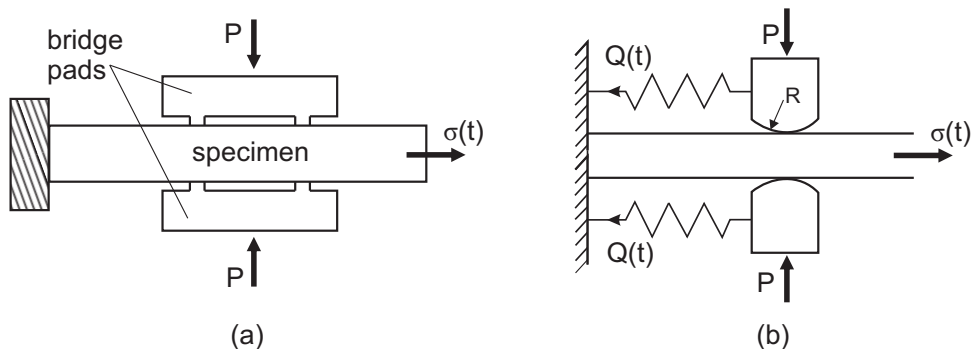


Figure 2.2: Fretting fatigue test configurations: (a) bridge pads, (b) cylindrical pads.

In their breakthrough in the experimental investigation of fretting fatigue, Nishioka and Hirakawa used a contact configuration characterized by cylindrical pads clamped against flat specimens, Figure 2.2(b). This contact geometry presents many advantages such as: pad alignment is not so critical and for some particular cases of interest (elastic regime and partial slip conditions), the analytical solution of the problem is known (Hertz, 1882; Mindlin, 1949). Besides, important parameters as the normal load, tangential and fatigue loads can be readily obtained throughout the experiment. Since then, this type of geometry has been used by many other authors (Bramhall, 1973; Hills et al., 1988; Rossino et al., 2009; Fouvry et al., 2008). In this kind of test set-up, the normal load  $P$  is usually static while the tangential load  $Q$  is cycled in phase with the bulk fatigue load applied to the specimen, Figure 2.2(b). Tests performed using spherical pads are also common, (Wittkowsky et al., 2000; Dubourg et al., 2003; Baietto et al., 2013). This

geometry favours the contact alignment, however, closed form analytical solutions are available only for axi-symmetric loads.

Other authors, on the other hand, have focused their attention on geometries closer to actual industrial components (Papanikos et al., 1998; Ruiz et al., 1984; Rajasekaran and Nowell, 2006). In (Ruiz et al., 1984), the apparatus consists of two blade specimens mounted in a central disk specimen, Figure 2.3. Tension loads are applied to the blade specimens simulating the centrifugal forces. The central disc is also subjected to tension loads simulating the disc expansion under centrifugal loading. High cycle fatigue loads are applied by shakers connected to the blades. Figure 2.4 depicts a photograph of a failed specimen from the biaxial dovetail apparatus (Rajasekaran and Nowell, 2006).

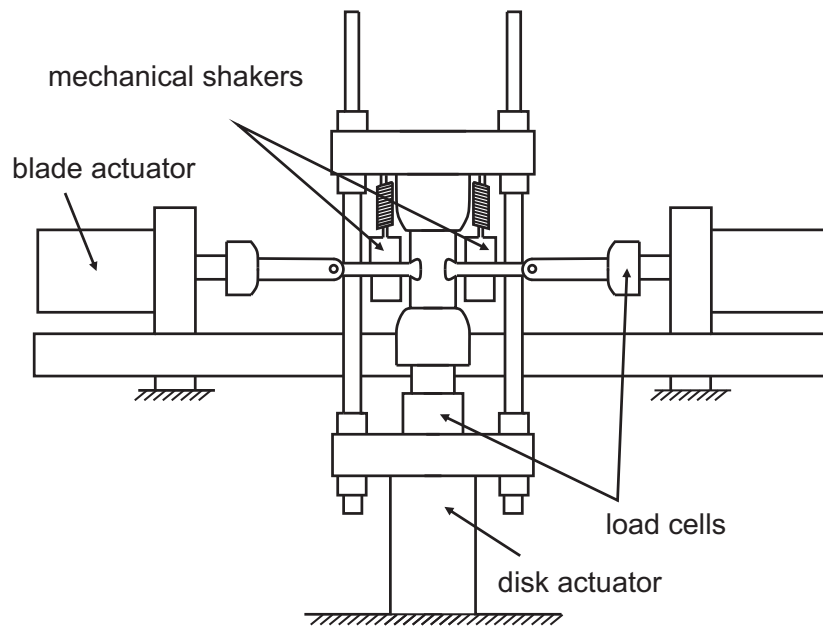


Figure 2.3: Dovetail fretting fatigue apparatus.



Figure 2.4: Failed blade specimen from the biaxial dovetail apparatus (Rajasekaran and Nowell, 2006).

At the University of Brasilia, fretting fatigue experiments are conducted in a MTS 322 Test Frame. This machine has two independent hydraulic actuators. One of them has a load capacity of 250 kN and it is responsible for applying the fatigue loads (including mean stress) while the other one, with a load capacity of 100 kN, is in charge of applying the shear fretting loads, Figure 2.5. The fretting actuator is coupled to an external device designed at the University of Brasilia where a pump is responsible for applying a compressive load  $P$  that presses the pad against the flat specimen (see the details in Figure 2.5). The maximum normal load that can be applied through this system is 22.4 kN. It is worth mentioning that, this arrangement demands a hydraulic accumulator in order to keep the normal load,  $P$ , constant during the experiments. For more details concerning pads alignment and friction coefficient determination the reader is referred to (Hills et al., 1988; Araujo and Nowell, 2002; Martins et al., 2008).

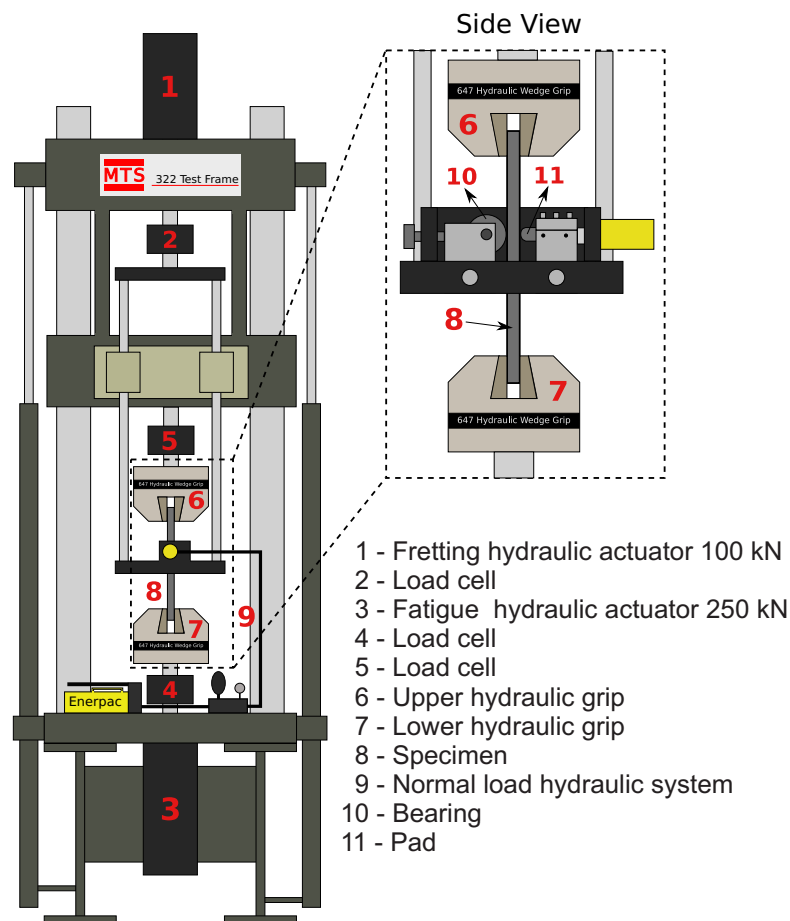


Figure 2.5: Schematic view of the fretting fatigue apparatus with two independent actuators at the University of Brasilia.

Alternatively, fretting fatigue experiments can be performed on uniaxial fatigue machines that have only one actuator, Figure 2.6. In this case, the tangential force  $Q$  is developed by restraining the pads movement by beams which act as springs. The load  $Q$  can be adjusted modifying the system stiffness by changing the relative position of the contact or varying the distance of the vertical columns, Figure 2.6.

The main advantage of the two actuator apparatus is that fretting and fatigue loads are

uncoupled, despite what happens with the one actuator set-up, providing more flexibility in the design of fretting conditions (e.g, fretting and fatigue loads out of phase).

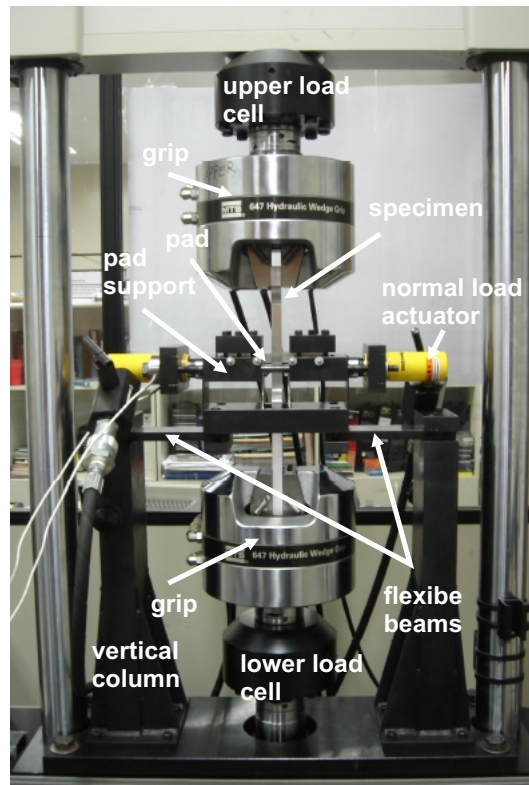


Figure 2.6: Fretting fatigue apparatus with only one actuator at the University of Brasilia.

## 2.4 Wear aspects in the context of fretting fatigue

Depending on the contact parameters, especially the slip amplitude, the fretting process can be divided into three different regimes (Hannel et al., 2001), namely partial slip regime (PSR), gross slip regime (GSR) and the so-called mixed slip regime (MSR). Regarding the PSR, the main mechanics of failure is fretting fatigue, where in this case the contact region is divided into slip and stick zones and the wear process is considerably small and confined into the slip areas. On the other hand, fretting wear is dominant in GSR, where in this case, crack growth is limited by the considerably high material removal. The MSR is observed for intermediate slip ranges and it inherits characteristics from both PSR and GSR. In (Zhou and Vincent, 1995) the MSR is reported to be the most dangerous regime for crack nucleation and propagation. The effect of slip amplitude can be qualitatively extracted through fretting maps as the one presented by (Vingsbo and Söderberg, 1988), Figure 2.1.

The damage process associated with contacts under fretting conditions is a synergistic competition involving wear, corrosion and fatigue phenomena. As a consequence, the use of pure stress-strain based multiaxial fatigue criteria may fail to interpret the effect of slip amplitude on fretting fatigue when wear effects are neglected (Jin and Mall, 2004).

During fretting, wear is inherent to the problem, influencing the nucleation and propagation of cracks. Recent studies (Madge et al., 2007a,b; Garcin et al., 2015) have taken into account this issue by developing a coupled wear and fatigue approach. The simulation of material removal is addressed by using local formulations of either the Archad's equation (McCull et al., 2004; Ding et al., 2004) or using frictional energy (Fouvry et al., 2003; Doca and Pires, 2017).

Archad's equation for sliding wear is commonly expressed as (Archard, 1953):

$$\frac{V}{S} = K \frac{P}{H} \quad (2.1)$$

where  $K$  is the dimensionless wear coefficient and  $H$  is the material hardness.  $P$ ,  $S$  and  $V$  are the normal contact load, total relative slip and volume of material removed, respectively. Considering an infinitesimal area, Eq. (2.1) can be expressed locally as:

$$dh = \kappa_w p ds \quad (2.2)$$

where  $dh$  is the material removal depth for a given incremental relative slip  $ds$ ,  $p$  is contact pressure and  $\kappa_w$  the local wear coefficient.

On the other hand, the friction energy wear law consists in relating the total wear volume to the accumulated friction energy dissipated on the contact interface.

$$V = \alpha \sum E_d \quad (2.3)$$

where  $E_d$  is the friction energy dissipated during a fretting cycle and  $\alpha$  is the energy wear coefficient. Locally, for an infinitesimal area, the wear depth can be expressed by

$$dh = \alpha q ds \quad (2.4)$$

where  $q$  is the contact shear traction.

Equations (2.2) and (2.4) implemented incrementally in a nodal basis through finite element simulations could provide a better understanding of the slip regimes influence on fretting fatigue behaviour, where in general, under gross slip conditions, wear has beneficial effects once that it removes severely damaged areas before cracks start propagating. On the contrary, under partial slip regimes, wear tends to increase the damage process and at the same shift the crack initiation sites towards the stick/slip transition regions (McCull et al., 2004; Ding et al., 2004; Madge et al., 2007a,b; Garcin et al., 2015).

## 2.5 Fatigue of materials

Fatigue of materials is characterized by the nucleation, coalescence, and stable growth of cracks leading to net section yielding or fracture (Socie and Marquis, 2000). In other words, it can be seen as the weakening of a material caused by repeatedly applied loads. It has also been reported in (Campbell, 2008) that nearly 90% of all mechanical service failures is due to fatigue.

In general, fatigue depends on many factors as frequency of the applied loads, material properties, stress raisers, load amplitude, load ratio and multiaxiality of the loads. The

fatigue phenomenon can also be divided in two different concepts, Low Cycle Fatigue (LCF) and High Cycle Fatigue (HCF). In the LCF, components are subjected to high loads which introduces appreciable levels of plasticity and short life endurance. On the other hand, in HCF, loads are sufficiently small in order to ensure primarily elastic deformation and long lives (for example, more than  $10^5$  cycles).

### 2.5.1 Crack initiation and propagation

Fatigue cracks mostly take place at free surfaces, however, in presence of internal defects such as voids and inclusions, they might initiate at sub-surfaces.

Cyclic plastic shear strain, cause the nucleation of slip bands. Grains whose crystallographic slip planes and directions are oriented in the same direction of the applied cyclic shear stress will be the first to form slip bands. At sufficiently high stresses and strains, slip bands are formed in a considerable amount of grains. In presence of repeated cyclic loading, these slip bands grow and merge into a single dominant fatigue crack. This initial stage is denominated Stage I (crack initiation), Figure 2.7. As the crack length becomes sufficiently large, the crack starts propagating perpendicularly to the principal stress, where this stage is referred as Stage II.

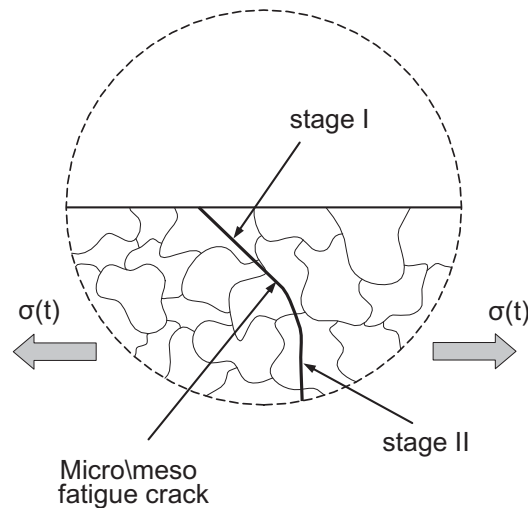


Figure 2.7: Illustration of the crack initiation/propagation process.

### 2.5.2 Wöhler diagram

Wöhler diagrams also known as S-N curves were first proposed by the German scientist Wöhler (1870) when evaluating fatigue failures in rail-road axles. In his studies, he developed an apparatus used to apply repeated loads to rail-road axles in an attempt to chart the relation between the load level and the number of cycles to failure. A few years later, (Basquin, 1910) observed a power function relationship between the nominal stress amplitude and the number of cycles to failure in HCF.

$$\sigma_a = \sigma'_f (2N_f)^{b'} \quad (2.5)$$

where  $\sigma_a$  is the stress amplitude,  $N_f$  is the number of cycles to failure,  $\sigma'_f$  is the fatigue strength coefficient and  $b'$  the fatigue strength exponent. This type of stress-life diagrams are still popular nowadays. In general, in order to obtain the parameters of Eq. (2.5) standard uniaxial laboratory tests are performed. In order to apply the cyclic loads various methods are available, e.g. rotating bend, cantilever bend, axial push-pull and torsion.

Some materials, notably low-carbon steels, exhibit a flattening off at a certain stress level, curve A in Figure 2.8, which is commonly referred as the fatigue limit. However, most materials, for instance aluminium and titanium alloys, exhibits a continually failing curve, curve B in Figure 2.8. In this case, the fatigue limit may be defined by choosing a level of stress below which failure is not expected to occur in less than a given number of cycles.

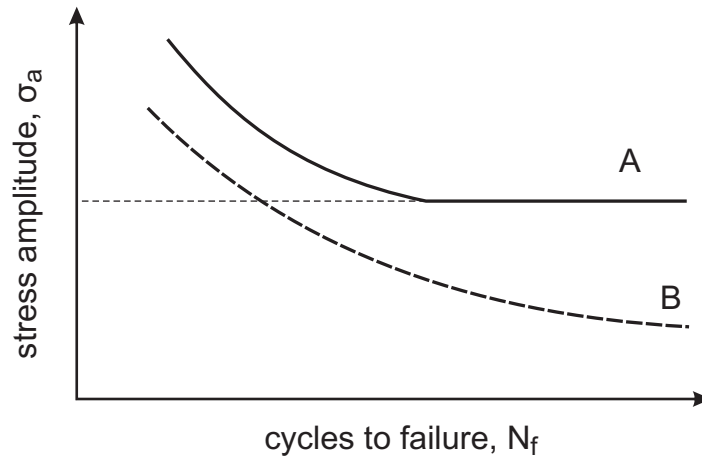


Figure 2.8: Typical S-N curves.

### 2.5.3 Uniaxial fatigue and the influence of the mean stress

Considering engineering applications, components subjected to cyclic loading conditions in the presence of mean loads are commonly observed. The well known results provided by (Goodman, 1899; Haigh, 1917) have shown that the presence of mean tensile stress tends to decrease the fatigue limit of materials while a compressive one may increase it. Physically speaking, it can be explained due to the fact that tensile loads tend to open pre-existent cracks whereas compressive loads tends to keep them closed. A common way for representing the influence of the mean stress in fatigue problems is to express the material fatigue endurance (stress amplitude) in terms of the mean stress, for example:

- Goodman equation (Goodman, 1899):

$$\sigma_a = \sigma_{-1} \left( 1 - \frac{\sigma_m}{\sigma_{ut}} \right) \quad (2.6)$$

- Soderberg equation (Soderberg, 1939):

$$\sigma_a = \sigma_{-1} \left( 1 - \frac{\sigma_m}{\sigma_y} \right) \quad (2.7)$$



- Gerber equation (Gerber, 1874):

$$\sigma_a = \sigma_{-1} \left[ 1 - \left( \frac{\sigma_m}{\sigma_{ut}} \right)^2 \right] \quad (2.8)$$

where  $\sigma_m$  is the mean stress,  $\sigma_{ut}$  the ultimate stress,  $\sigma_y$  the yield stress and  $\sigma_{-1}$  is the fatigue limit for a fully reversed axial test (load ratio  $R_\sigma = -1$ ). Figure 2.9 depicts the shape of these equations. As can be seen, Soderberg is the most conservative model while Gerber is the most optimistic one. In general, they accuracy will depend on the material analysed.

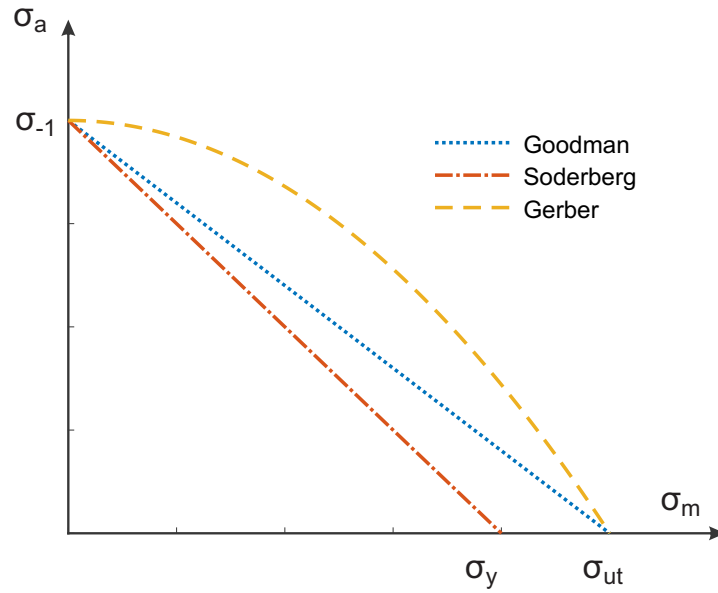


Figure 2.9: Schematic representation of Haigh diagram for a constant life.

#### 2.5.4 Miner linear cumulative damage law

Miner (1945) popularized a linear cumulative damage rule that had first been proposed independently by (Palmgren, 1924). According to this uncoupled damage rule, fatigue failure under a set of different stress levels is observed when:

$$\sum_i \frac{\Delta N_i}{N_{f,i}} = 1 \quad (2.9)$$

where  $N_{f,i}$  is the number of cycles to failure at a given stress level  $\sigma_{a,i}$  and  $\Delta N_i$  is number of cycles applied at each stress level  $\sigma_{a,i}$ , Figure 2.10.

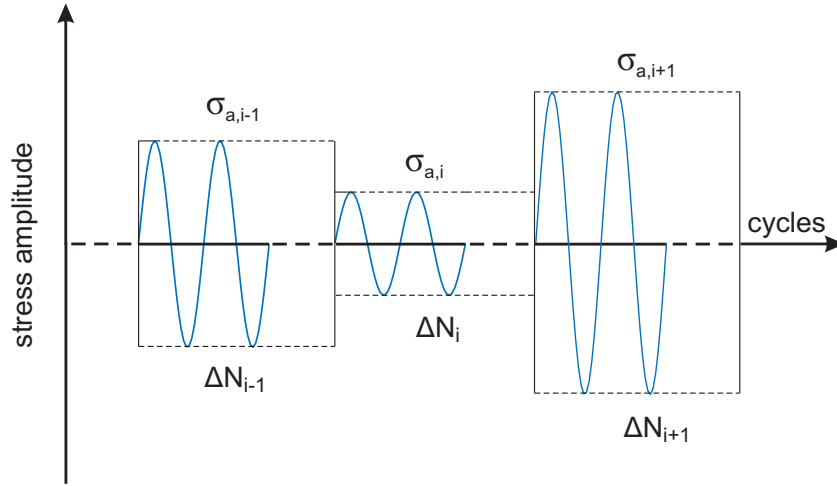


Figure 2.10: Loading history at different stress levels.

In practice, mechanical components are subjected to complex, sometimes even random, sequence of loads. However, in these cases, the complex loading history is reduced to a series of simple cyclic loadings by using techniques such as the rain-flow counting method (Matsuishi and Endo, 1968). Then, for each stress level, Miner's rule can be applied. One of the main advantages of Miner's damage rule is its simplicity, however, one of its main drawbacks relies on the fact that it is incapable of recognizing loading sequence effects.

## 2.5.5 Multiaxial fatigue

Most of the experimental data available, even today, consists of tests performed under uniaxial stress or pure torsional conditions. However, for engineering applications, multiaxial stress states are much more likely to happen. In this case, it is often unrealistic the idea of reproducing experimentally the load conditions observed in real components experiencing service conditions. The basic idea behind the multiaxial fatigue criteria is to use data provided from simple laboratory tests in order to design against multiaxial and more complex stress states.

### 2.5.5.1 Findley

After analyse an extensive amount of experiments, for instance the ones carried out by (Gough, 1949; Gough and Pollard, 1935), Findley (1958) have proposed the following multiaxial fatigue damage parameter:

$$I_{FP} = (\tau_a + \gamma\sigma_{n,max})_{max} \quad (2.10)$$

where  $\gamma$  is a material parameter.  $\tau_a$  and  $\sigma_{n,max}$  are the shear stress amplitude and the maximum normal stress, respectively, for a given material plane. The idea behind this model is that shear stresses lead to crack nucleation and early propagation whereas normal stress increases crack opening and consequently rate of growth. For ductile materials  $\gamma$  ranges between 0.2 and 0.3 and it can be obtained considering the results of fatigue tests performed on different stress states, for example see Table 2.1.

Table 2.1: Solutions for  $\gamma$  based on the ratio of fatigue strength for two stress states.

Ratio of fatigue strength	$\gamma$ expression
$\frac{\sigma_{-1}}{\tau_{-1}}$	$\frac{2}{1 + \frac{\gamma}{\sqrt{1 + \gamma^2}}}$
$\frac{\sigma_0}{\sigma_{-1}}$	$\frac{\gamma + \sqrt{1 + \gamma^2}}{2\gamma + \sqrt{1 + (2\gamma)^2}}$
$\frac{\sigma_{0.5}}{\sigma_{-1}}$	$\frac{\gamma + \sqrt{1 + \gamma^2}}{4\gamma + \sqrt{1 + (4\gamma)^2}}$

### 2.5.5.2 Smith, Watson and Topper (SWT)

An alternate model is necessary for materials that fail predominately by crack growth on planes of maximum tensile strain or stress. In these materials, despite the fact that cracks still nucleates under shear mode, crack growth takes place on planes perpendicular to maximum principal stress and strain. In their model, Smith et al. (1970) proposed a relationship that takes into account both cyclic strain range and maximum normal stress.

$$I_{SWT} = \sigma_{n,max} \frac{\Delta\varepsilon_n}{2} \quad (2.11)$$

where  $\sigma_{n,max}$  and  $\Delta\varepsilon_n$  are the maximum normal stress and normal strain range on the material plane that maximizes their product. This model can also handle non-proportional loading conditions. It also permits to estimate the component life by reference to a fully reversed uniaxial test where Basquin (stress-life) and Coffin Manson (strain-life) relations can be combined yielding:

$$\sigma_{n,max} \frac{\Delta\varepsilon_n}{2} = \frac{(\sigma'_f)^2}{E} (2N_f)^{b'} + \sigma'_f \varepsilon'_f (2N_f)^{b'+d'} \quad (2.12)$$

where  $\varepsilon'_f$  and  $d'$  are the fatigue ductility coefficient and exponent, respectively.

### 2.5.5.3 Modified Wöhler Curve Method (MWCM)

Based on the theory of cyclic deformation in single crystals, which suggests that fatigue damage in polycrystals depends on the maximum shear stress amplitude and stress component normal to the crack initiation plane, Susmel and Lazzarin (2002) proposed their model.

Considering the assumption that cracks nucleates on planes experiencing maximum shear stress amplitude, the critical plane can be defined as the material plane subjected to the maximum shear stress amplitude  $\tau_a$  over a loading cycle. Regarding this plane, it is also possible to define the following stress ratio:

$$\rho = \frac{\sigma_{n,max}}{\tau_a} \quad (2.13)$$

where  $\sigma_{n,max}$  is the maximum normal stress developed at the critical plane. Note that this term accounts the influence of mean stress on multiaxial fatigue strength. Without further ado, the idea of the MWCM consists in characterizing the conventional S-N curves however assessing  $\tau_a$  vs  $N_f$ , Susmel and Lazzarin (2002). As well as the presence of mean stress modifies S-N curves, the stress ratio  $\rho$  alters the Modified Wöhler curves, Figure 2.11, where  $\tau_{a,ref}$  is defined as the shear stress amplitude at a certain number of cycles to failure  $N_{ref}$  and  $\kappa_\tau$  is the inverse slope of the curve  $\log(N_f)$  vs.  $\log(\tau_a)$ . Therefore, for a generic stress ratio  $\rho$  and shear stress amplitude  $\tau_a$ , the fatigue life may be estimated through the following relation:

$$N_f = N_{ref} \left[ \frac{\tau_{a,ref}(\rho)}{\tau_a} \right]^{\kappa_\tau(\rho)} \quad (2.14)$$

where  $\tau_{a,ref}(\rho)$  and  $\kappa_\tau(\rho)$  can be obtained through linear interpolation considering data from two different experiment campaigns. For example, considering fully reversed uniaxial ( $\rho = 1$ ) and torsional ( $\rho = 0$ ) fatigue curves one has:

$$\tau_{a,ref}(\rho) = [\tau_{a,ref}(\rho = 1) - \tau_{a,ref}(\rho = 0)]\rho + \tau_{a,ref}(\rho = 0) \quad (2.15)$$

and

$$\kappa_\tau(\rho) = [\kappa_\tau(\rho = 1) - \kappa_\tau(\rho = 0)]\rho + \kappa_\tau(\rho = 0) \quad (2.16)$$

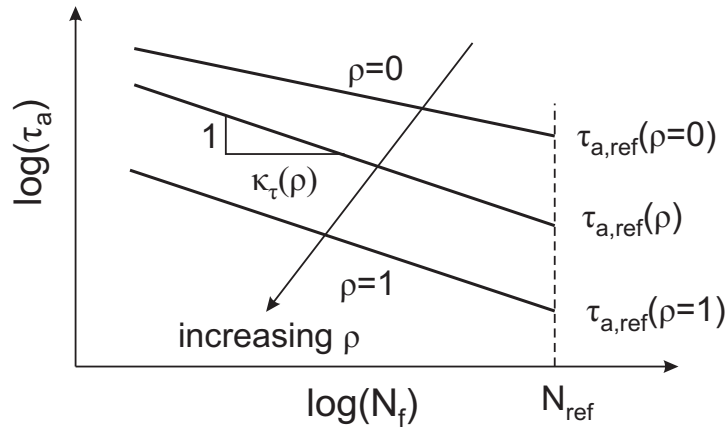


Figure 2.11: Modified Wöhler curves.

When reference shear stress values correspond to fatigue limits, Eq. (2.15) becomes:

$$\tau_a + \left( \tau_{-1} - \frac{\sigma_{-1}}{2} \right) \frac{\sigma_{n,max}}{\tau_a} \leq \tau_{-1} \quad (2.17)$$

It is worth mentioning that the use of the MWCM for large values of  $\rho$  leads to conservative results. It can be explained by the fact that, once the mean normal stress on the critical plane is larger than a certain value, micro/meso cracks are completely open and thus shear forces are completely transmitted to the crack tips instead of being partially supported by the friction interactions between cracks faces (Carpinteri et al., 2003; Susmel, 2008).

Therefore, the MWCM formulation is valid as long as  $\rho$  is lower than a threshold value  $\rho_{crit}$ , where its expression is given by (Susmel, 2009):

$$\rho_{crit} = \frac{\tau_{-1}}{2\tau_{-1} - \sigma_{-1}} \quad (2.18)$$

where whenever  $\rho \geq \rho_{crit}$  it can be set to  $\rho_{crit}$ .

#### 2.5.5.4 Definition of the multiaxial fatigue criteria stress parameters.

Consider a material plane  $\Delta$  where its normal is given by the unitary vector  $\underline{n}$ . Consider as well two other unitary vectors  $\underline{\eta}_1$  and  $\underline{\eta}_2$  which lies on the  $\Delta$  plane, Figure 2.12. These three vectors are also orthogonal with respect to each other. In this setting, for a given time instant  $t$  the stress component normal to this plane is given by

$$\sigma_n(t) = \underline{n} \cdot \underline{\underline{\sigma}}(t)\underline{n} \quad (2.19)$$

while the components of the shear stress when projected on the basis  $\underline{\eta}_1$  and  $\underline{\eta}_2$  are given respectively by

$$\tau_1(t) = \underline{\eta}_1 \cdot \underline{\underline{\sigma}}(t)\underline{n} \quad (2.20)$$

and

$$\tau_2(t) = \underline{\eta}_2 \cdot \underline{\underline{\sigma}}(t)\underline{n} \quad (2.21)$$

where  $\underline{\underline{\sigma}}$  is the Cauchy stress tensor. In this framework, the definition of  $\sigma_{n,max}$  used in the multiaxial fatigue criteria is readily obtained

$$\sigma_{n,max}(t) = \max_t[\sigma_n(t)] \quad (2.22)$$

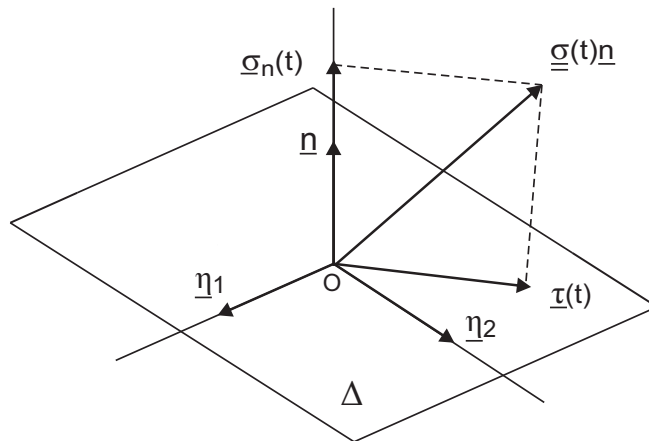


Figure 2.12: Material plane  $\Delta$  and stress vector decomposition.

On the other hand, the definition of  $\tau_a$  is more challenging once that the shear stress vector may describe a generic path  $\Theta$  as the one illustrated by the red curve in Figure 2.13.

Some definitions of  $\tau_a$  are also depicted in this figure. The Minimum Radius Circle (MRC) (Dang Van et al., 1989), Figure 2.13(a), may fail for some loading paths, e.g. rectangular ones. Mamiya and Araújo (2002) proposed the Minimum F-norm Ellipse method, Figure 2.13(b). In this case, for elliptical paths, it was shown that the shear stress amplitude could be computed from the axes of any arbitrarily oriented rectangular hull. However this method is restricted to cases where the rectangular hull circumscribing the load path  $\Theta$  approximates well an ellipsoid. Later (Mamiya et al., 2009) came up with the definition of the Maximum Rectangular Hull (MRC), Figure 2.13(c), which besides its simplicity, it can handle non-proportional paths better than the MRC, for instance. More recently, Meggiolaro and de Castro (2015) proposed the Moment of Inertia (MOI) Method, which better handles path-shape dependence issues.

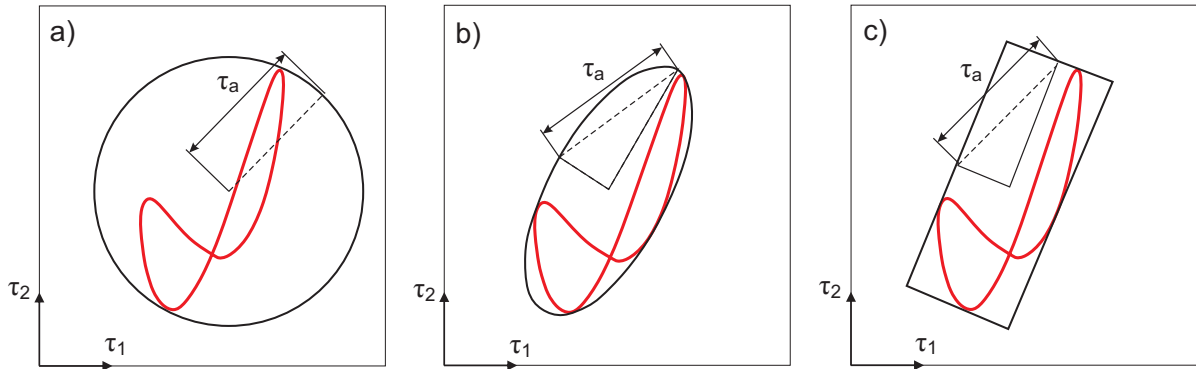


Figure 2.13: Different definitions for the shear stress amplitude, adapted from (Castro et al., 2009): (a) Minimum Radius Circle; (b) Minimum F-norm Ellipse; (c) Maximum Rectangular Hull.

## 2.6 Theory of critical distances (TCD)

It is well known that hot-spot approaches lead to very conservative results when high stress gradients are present like the ones found close to notches and the edges of contact problems. The theory of critical distances (TCD) was first proposed in order to deal with problems in presence of stress raisers such as notches and cracks (Taylor, 1999). In its most fundamental definition, the idea consists in evaluating an effective stress  $F(\underline{\sigma})$  that can appropriately characterize the fatigue damage process inside a specified volume  $V$  surrounding the stress raiser:

$$\frac{1}{V} \int_V F(\underline{\sigma}) dV \leq b \quad (2.23)$$

where  $b$  is a material property associated with its fatigue strength. The volume  $V$ , in general is associated with the material characteristic length  $L$ , a material property that can be defined as (El Haddad et al., 1979):

$$L = \frac{1}{\pi} \left( \frac{\Delta K_{th}}{\Delta \sigma_{-1}} \right)^2 \quad (2.24)$$

where  $\Delta K_{th}$  is the material threshold stress intensity factor range and  $\Delta\sigma_{-1}$  is the uniaxial fatigue limit range. For 2D analysis, the TCD can be expressed in its simplified versions (Figure 2.14) by substituting the material volume mentioned above by a point, line or area, receptively:

- Point method

$$F(\underline{\sigma}(r = L/2, \theta = 0)) \leq b \quad (2.25)$$

- Line method

$$\frac{1}{2L} \int_0^{2L} F(\underline{\sigma}(r, \theta = 0)) dr \leq b \quad (2.26)$$

- Area method

$$\frac{2}{\pi L^2} \int_{-\pi/2}^{\pi/2} \int_0^L F(\underline{\sigma}(r, \theta)) r dr d\theta \leq b \quad (2.27)$$

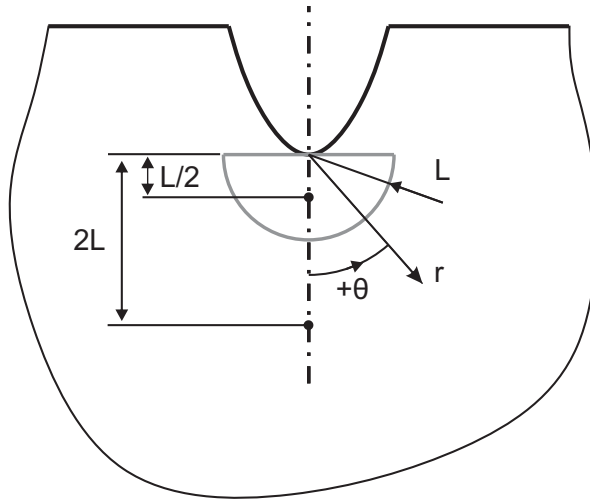


Figure 2.14: TCD averaging regions in its simplified 2D versions (point, line and area).

One of the main advantages of the TCD is that it can be used in conjunction with any multiaxial fatigue criteria (Susmel et al., 2006). However, some more recent works have claimed that the critical distance parameter (Eq. (2.24)) may vary depending on the number of cycles (Susmel and Taylor, 2007, 2008).

## 2.7 Basic contact mechanics

Typically, fretting problems involve the contact of components of great complexity. In this setting, numerical methods becomes mandatory where the finite element method is

mostly the option chosen. This section however focuses on the analytic aspects of contact problems, more specifically, the contact between a cylinder pressed onto an elastic half-plane. More details about numerical aspects are given in 3.3. This contact set-up is often assessed experimentally once that it has well-defined stresses/displacement solutions. Besides, tests are easily controlled, repeatable and insensitive to small fabrication imperfections (Hills and Nowell, 1994).

### 2.7.1 Surface tractions distributions

In this section, the analytical solutions which ensure a full determination of the contact tractions for the cylinder on plane contact configuration (Figure 2.15) is presented. In this case, the results provided by (Hertz, 1882) have shown that the pressure distribution developed between two cylindrical contact surfaces subjected to a static normal load  $P$  is given by

$$p(x) = -p_0 \sqrt{1 - \left(\frac{x}{a}\right)^2} \quad (2.28)$$

where  $p_0$  is the peak pressure

$$p_0 = \frac{2P}{\pi a} \quad (2.29)$$

$a$  is the contact semi-width

$$a = \sqrt{\frac{4PR^*}{\pi E^*}} \quad (2.30)$$

where

$$R^* = \left(\frac{1}{R_1} + \frac{1}{R_2}\right)^{-1} \quad (2.31)$$

being  $R_1$  and  $R_2$  the radius of the bodies coming into contact. For the cylinder on plane configuration,  $R^*$  is simply equal to the pad radius. The equivalent Young modulus in Eq. (2.30) is given by

$$E^* = \left(\frac{1 - \nu_1^2}{E_1} + \frac{1 - \nu_2^2}{E_2}\right)^{-1} \quad (2.32)$$

where  $E$  and  $\nu$  are, respectively, the Young modulus and the Poisson's ratio. The subscripts 1 and 2 refer to each body in contact.

In presence of a tangential load  $Q$ , shear tractions are developed along the contact surface. The solution of this problem was given by (Cattaneo, 1938) and independently by (Mindlin, 1949). Once that the elliptical distribution of the contact pressure falls to zero at the contact extremities, it is unavoidable that some slip takes place nearby the contact edges even when  $Q/P$  is less than the friction coefficient  $\mu$  (partial slip conditions). In this case, it is reasonable assuming that two symmetrical slip zones surrounding a central stick zone are formed along the contact surface. Mathematically speaking, this feature



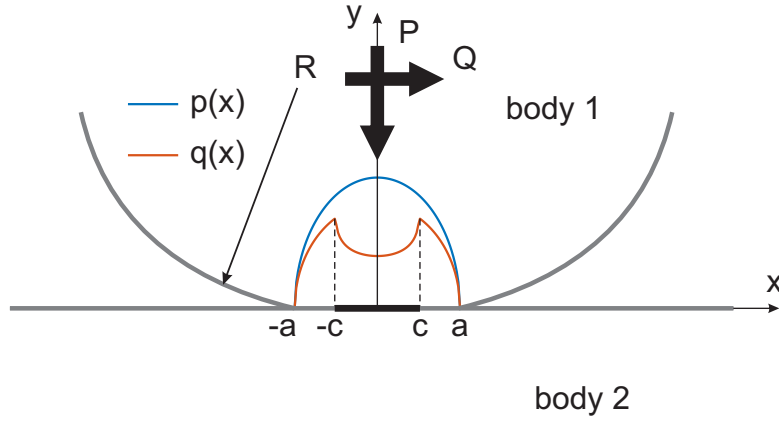


Figure 2.15: Schematic representation of the cylinder on plane contact configuration.

can be addressed to the problem facing the shear traction distribution  $q$  for partial slip conditions as a perturbation of the solution for gross sliding:

$$q(x) = \mu p_0 \sqrt{1 - \left(\frac{x}{a}\right)^2} + q'(x) \quad (2.33)$$

where

$$q'(x) = \begin{cases} 0, & \text{if } c \leq |x| \leq a \\ -\mu p_0 \frac{c}{a} \sqrt{1 - \left(\frac{x}{c}\right)^2}, & \text{if } |x| < c \end{cases} \quad (2.34)$$

where  $a$  is the semi-width of the contact zone and the semi-width of the stick zone  $c$  is obtained imposing tangential equilibrium:

$$\frac{c}{a} = \sqrt{1 - \left| \frac{Q}{fP} \right|} \quad (2.35)$$

Under fretting conditions, the tangential load  $Q$  varies over time. Figure 2.16 depicts a typical load history for the tangential load. The tangential traction  $q(x)$  presented so far is valid only when the tangential load is applied monotonically from 0 to its maximum value  $Q_{max}$ , point A (Figure 2.16). However, as soon as the tangential load is infinitesimally decreased from point A to B, the whole contact experiences stick condition. Note that the tangential traction acts oppositely to relative motion between the contact parts and at this point, this condition is violated. Further reducing the load  $Q$  to point C will lead the appearance of reversal slip once that, locally, the relative motion between the contact parts has been reversed. In the knew slip zones, shear traction will change from  $\mu p(x)$  to  $-\mu p(x)$ . In order to capture these effects, a second corrective term  $q''$  is added to the shear traction construction:

$$q''(x) = 2\mu p_0 \frac{c'}{a} \sqrt{1 - \left(\frac{x}{c'}\right)^2} \quad (2.36)$$

The following shear traction is then obtained, see Hills and Nowell (1994) for more details:

$$\frac{q(x)}{\mu p_0} = \begin{cases} -\sqrt{1 - \left(\frac{x}{a}\right)^2}, & \text{if } c' < |x| \leq a \\ -\sqrt{1 - \left(\frac{x}{a}\right)^2} + 2\frac{c'}{a}\sqrt{1 - \left(\frac{x}{c'}\right)^2} & \text{if } c < |x| \leq c' \\ -\sqrt{1 - \left(\frac{x}{a}\right)^2} + 2\frac{c'}{a}\sqrt{1 - \left(\frac{x}{c'}\right)^2} - \frac{c}{a}\sqrt{1 - \left(\frac{x}{c}\right)^2}, & \text{if } |x| \leq c \end{cases} \quad (2.37)$$

where again, from the equilibrium of forces in the tangential direction:

$$\frac{c'}{a} = \sqrt{1 - \left(\frac{Q_{max} - sQ(t)}{2\mu P}\right)} \quad (2.38)$$

where one assumes  $s = 1$  when one moves from  $Q_{max}$  towards  $Q_{min}$  and  $s = -1$  during the reloading phase, i.e. from  $Q_{min}$  to  $Q_{max}$  in the tangential loading cycle, Figure 2.16.

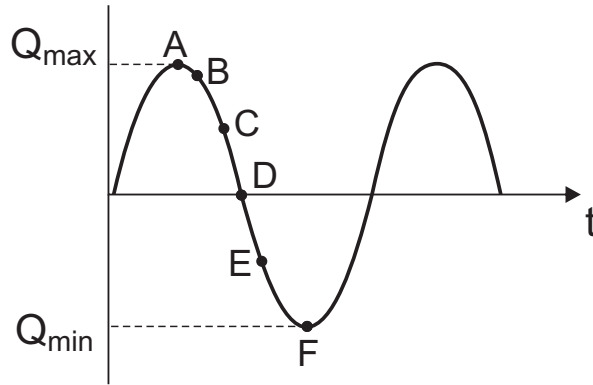


Figure 2.16: Variation of the tangential load  $Q$  over time.

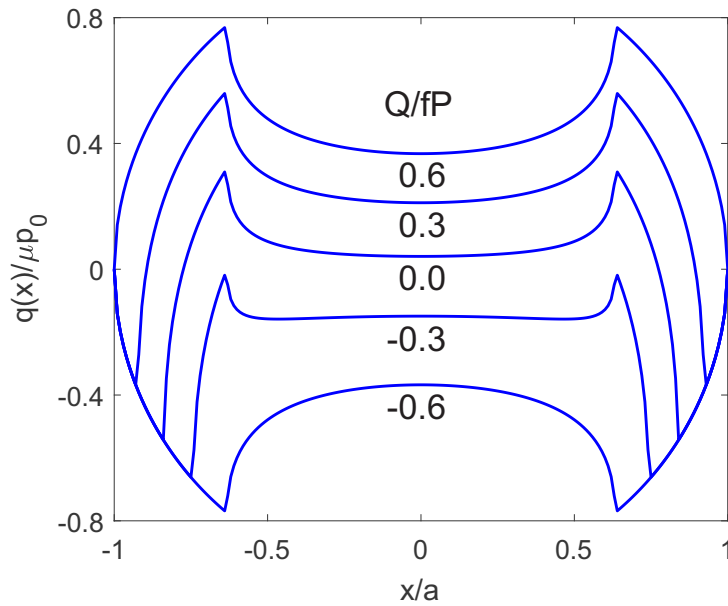


Figure 2.17: Shear traction distributions during a tangential cycle,  $Q_{max}/\mu P = 0.6$ .

Figure 2.17 depicts the shear tractions distribution during a tangential cycle when moving from point A to F in Figure 2.16. Note that when the tangential load  $Q$  is null the shear traction distribution along the contact surface does not vanish, which exemplifies the loading history dependency in contact problems. It also worth mentioning that the contact solutions presented in this section are valid for elastically similar bodies, which implies that  $p(x)$  and  $q(x)$  are uncoupled. In other words, tangential loads do not modify the contact pressure distribution and normal loads do not generate shear tractions.

### 2.7.2 Bulk load effect on the shear traction distribution

Fretting fatigue in general takes place in the presence of bulk stresses acting in one or both of the contacting bodies. Let one considers here that only the flat specimen, body 2 in Figure 2.15 is subjected to a bulk load acting in phase with the tangential load  $Q$ . This bulk load generates a bulk stress  $\sigma_b(t)$  on the specimen which will cause a mismatch in strain between the contacting parts. This mismatch will modify the Mindlin-type analyses presented in the previous section. Now the perturbation solutions  $q'$  and  $q''$  in Eq. (2.37) need to be rewritten as follows:

$$q' = -\mu p_0 \frac{c}{a} \sqrt{1 - \left(\frac{x-e}{c}\right)^2} \quad (2.39)$$

and

$$q'' = 2\mu p_0 \frac{c'}{a} \sqrt{1 - \left(\frac{x-e'}{c'}\right)^2} \quad (2.40)$$

where the normalized offset terms  $e/a$  and  $e'/a$  are given respectively by:

$$\frac{e}{a} = \frac{\sigma_{b,max}}{4\mu p_0} \quad (2.41)$$

being  $\sigma_{b,max}$  the maximum value reached by the bulk stress over a cycle and

$$\frac{e'}{a} = \frac{\sigma_{b,max} - s\sigma_b(t)}{8\mu p_0} \quad (2.42)$$

It is worth pointing out that, these equations are valid only for small values of bulk fatigue load where the following relations must be respected:  $e + c < a$  and  $e' + c' < a$ . Figure 2.18 depicts the shear traction distributions for different time instants (Figure 2.16) when the specimen is subjected to a sinusoidal bulk stress  $\sigma_b$  in phase with the tangential load  $Q$ .

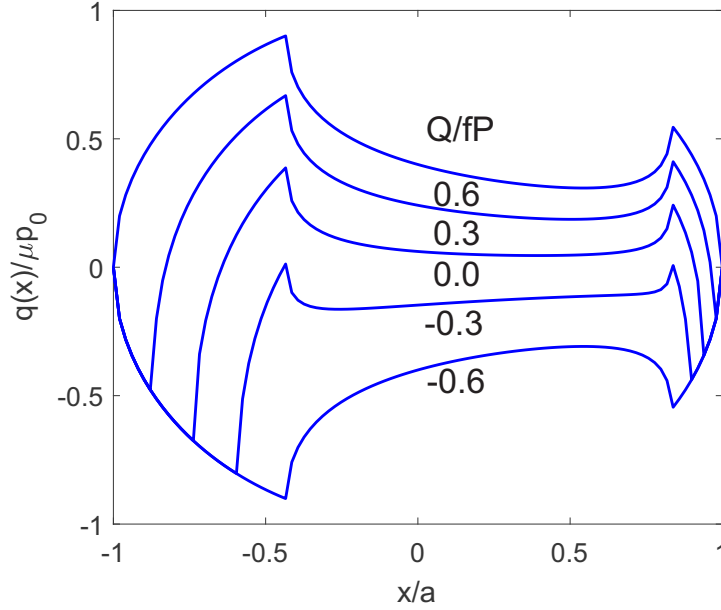


Figure 2.18: Shear traction distributions during a fretting cycle,  $Q_{max}/\mu P = 0.6$  and  $\sigma_{b,max}/\mu p_0 = 0.8$ .

### 2.7.3 Sub-surface stress distributions

For plane problems, the most popular way to compute the internal stress distribution is via Muskhelishvili potential (Muskhelishvili, 1953). This potential,  $\phi$ , is a function of position,  $z$ , which is a complex coordinate, i.e.  $z = x + yi$ . The potential itself can be obtained performing a contour integral along the contact line:

$$\phi(z) = \frac{1}{2\pi i} \int_{\text{contact}} \frac{p(\varsigma) - iq(\varsigma)}{\varsigma - z} d\varsigma \quad (2.43)$$

Once the potential  $\phi$  is found, stress components can be defined by

$$\sigma_{xx} + \sigma_{yy} = 2[\phi(z) + \bar{\phi}(\bar{z})] \quad (2.44)$$

$$\sigma_{yy} - \sigma_{xx} + 2i\sigma_{xy} = 2[(\bar{z} - z)\phi'(z) - \bar{\phi}(z) - \phi(z)] \quad (2.45)$$

where  $\phi'(z)$  implies differentiation with respect to  $z$  and  $\bar{\bullet}$  implies taking the conjugate. For the cylinder on plane contact configuration here assessed, pressure distribution has an elliptical profile. In addition, the shear traction distribution is a superposition of elliptical traction distributions. In this setting, two different potential expressions can be defined:

$$\phi^n(z) = \frac{1}{2\pi i} \int_{\text{contact}} \frac{p(\varsigma)}{\varsigma - z} d\varsigma \quad (2.46)$$

$$\phi^t(z) = \frac{1 - i\mu}{2\pi i} \int_{\text{contact}} \frac{p(\varsigma)}{\varsigma - z} d\varsigma \quad (2.47)$$

where  $\phi^n$  is obtained considering only the normal load,  $P$ , while  $\phi^t$  is obtained considering gross sliding conditions. Therefore, solving the linear system described by Eqs. (2.44) and (2.45), the following expressions for the  $\sigma_{xx}$  stress component can be obtained for instance:

- At maximum and minimum loads:

$$\frac{\sigma_{xx}(x, y)}{p_0} = \left( \frac{\sigma_{xx}^n \left( \frac{x}{a}, \frac{y}{a} \right)}{p_0} \right) \pm \mu \left( \frac{\sigma_{xx}^t \left( \frac{x}{a}, \frac{y}{a} \right)}{\mu p_0} \right) \mp \mu \frac{c}{a} \left( \frac{\sigma_{xx}^t \left( \frac{x-e}{c}, \frac{y}{c} \right)}{\mu p_0} \right) + \frac{\sigma_b}{p_0} \quad (2.48)$$

where the signal combination + and - holds for the maximum load.

- During unloading and reloading phases:

$$\begin{aligned} \frac{\sigma_{xx}(x, y)}{p_0} &= \left( \frac{\sigma_{xx}^n \left( \frac{x}{a}, \frac{y}{a} \right)}{p_0} \right) \mp \mu \left( \frac{\sigma_{xx}^t \left( \frac{x}{a}, \frac{y}{a} \right)}{\mu p_0} \right) \pm 2\mu \frac{c'}{a} \left( \frac{\sigma_{xx}^t \left( \frac{x-e'}{c'}, \frac{y}{c'} \right)}{\mu p_0} \right) \\ &\mp \mu \frac{c}{a} \left( \frac{\sigma_{xx}^t \left( \frac{x-e}{c}, \frac{y}{c} \right)}{\mu p_0} \right) + \frac{\sigma_b}{p_0} \end{aligned} \quad (2.49)$$

where the signal combination -, + and - holds for the unloading phase.

Similarly, the other stress components can be obtained.

# Chapter 3

## A new multiscale approach for the simulation of fretting problems

In this chapter, the first part of the research conducted in this thesis is addressed, where a new methodology for the simulation of fretting problems in the context of the FE framework is presented. In this setting, the idea is to reduce the computational cost when performing fretting simulations and at the same time keep the accuracy of stress/strain solutions close to the contact zones. More specifically, at the contact edges, regions where the stress state is in general the most severe. For so, an enrichment-based approach is used in order to enrich the displacement field close to the contact edges. This chapter is organized as follows: in the first two sections, the spatial modes utilized in order to enrich the fretting simulations as well as the enrichment technique here considered are presented. In the next section, concepts concerning the numerical implementation of contact problems are discussed. After that, simulations considering the enrichment technique proposed are compared with standard FE simulations in order to verify its applicability and benefits when considering both partial and gross slip conditions.

### 3.1 Reduced basis (spatial modes) and crack analogy

In this section, the non-intrusive methodology proposed by (Montebello et al., 2016) used to extract the spatial modes that will be further used to enrich the fretting simulations will be briefly presented. For further details, the reader is referred to (Montebello, 2015; Montebello et al., 2016).

One of the main features of fretting-fatigue problems is the considerably high and localized stress gradient generated by the contact loads, which nearby the contact edges is comparable to what happens close to the crack tip (complete contacts) or in the vicinity of notches (incomplete contacts) (Giannakopoulos et al., 1998, 2000). For instance, in the crack analogue applied to complete contact configurations proposed by (Giannakopoulos et al., 1998), the normal load  $P$ , generates a symmetric field which is analogue to what is observed in a crack loaded under mode I, whereas, the antisymmetric effect of the tangential load  $Q$  is comparable to a mode II loading, Fig. 3.1. In this setting, expression for stress intensity factors can be readily obtained using fracture mechanics insights. In spite of these really interesting features, this type of approach is restricted to some simple

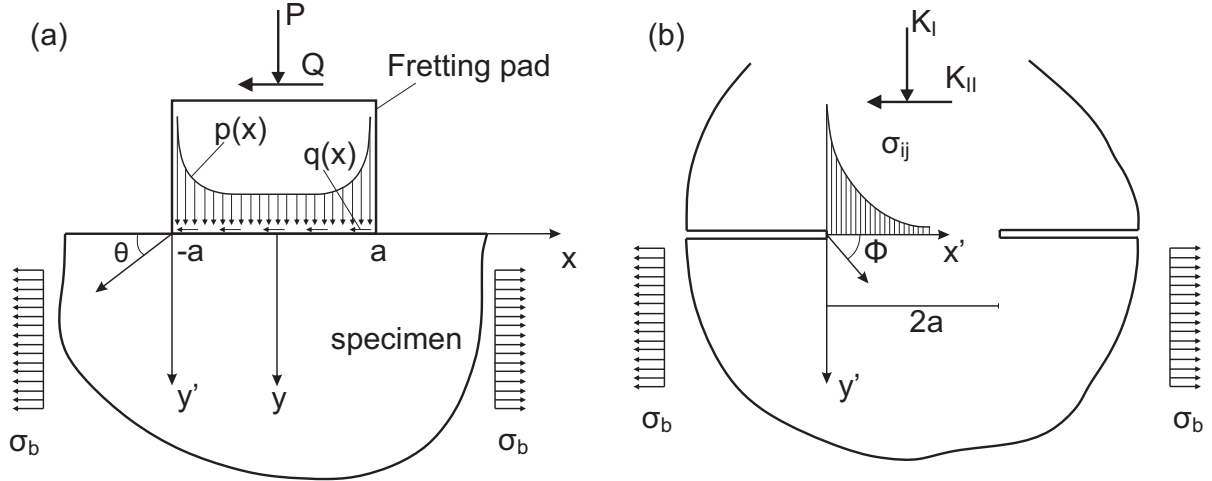


Figure 3.1: Analogy between complete contact under fretting condition (a) and double-edge cracked plate (b).

contact geometries like the one presented Fig. 3.1 when predominantly stick condition is held.

Considering the crack tip in fracture mechanics problems, an original approach was proposed by (Pommier et al., 2009) in order to describe mixed-mode cyclic elastic-plastic behaviour at the global scale. The goal was to establish a model reasonably precise but condensed into a set of partial derivative equations avoiding huge plastic FE computations. In this context, the kinematics of the crack tip region was characterized by a set of condensed variables (model order reduction). The non-intrusive methodology proposed by (Montebello et al., 2016) is highly inspired in the aforementioned works, where the aim was to describe the stress field under fretting conditions arising close to the contact edges via nonlocal stress intensity factors, transposing what have been done by (Pommier et al., 2009) to fretting fatigue problems, which was justified by the analogies between these two problems of different nature (Giannakopoulos et al., 1998, 2000).

The idea, basically, relies on the fact that in presence of strong gradients, the local geometry dictates the mechanical fields distribution while its intensity is governed by macroscopic loads. It suggests that the solution of the problem can be described through a “fracture mechanics approach”, where the velocity field, for instance, can be computed as a product between intensity factors and spatial reference fields:

$$\underline{v}(\underline{x}, t) \simeq \underbrace{\dot{I}^s(t)\underline{d}^s(\underline{x}) + \dot{I}^a(t)\underline{d}^a(\underline{x})}_{\underline{v}^e} + \underbrace{\dot{I}^c(t)\underline{d}^c(\underline{x})}_{\underline{v}^c} \quad (3.1)$$

where  $\underline{v}(\underline{x}, t)$  is expressed with respect to a reference system attached to the contact edge, Figure 3.2, while  $\underline{x}$  and  $t$  are position and time, respectively (see Appendix A). Velocity is chosen rather than displacement or stress once that the velocity field characterizes better the nonlinear behaviour due to friction (load history dependency). As can be seen in Eq. (3.1), the velocity field is partitioned into two parts,  $\underline{v}^e$  which is related to the linear response of the problem and  $\underline{v}^c$  which represents the nonlinear response due to friction inside the slip zones. In addition, the linear part can be divided into a symmetric and an antisymmetric part as presented in Eq. (3.1). The idea is that each one of these terms can

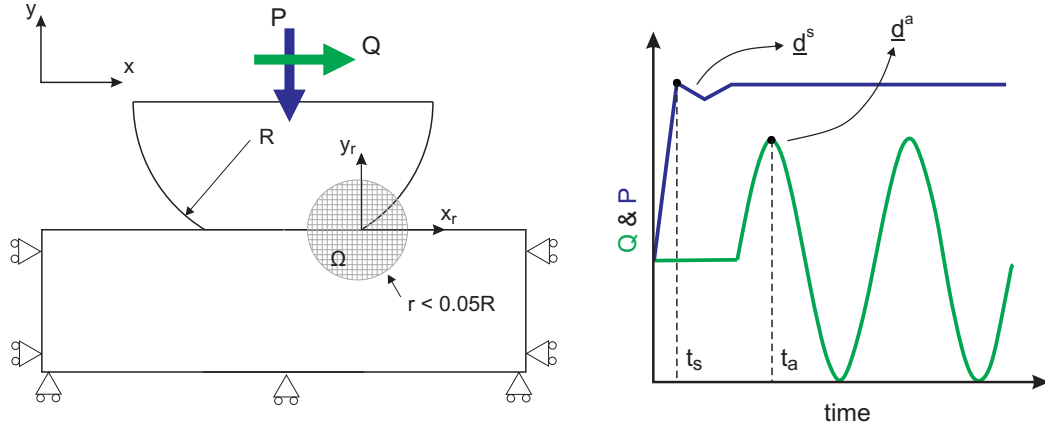


Figure 3.2: FE model used to extract the spatial modes and the nonlocal intensity factors.

be described as product of nonlocal intensity factors ( $\dot{I}^s$ ,  $\dot{I}^a$ ,  $\dot{I}^c$ ), capable of capturing the effects of the macroscopic loads, and spatial modes, that describe the local geometrical effects ( $\underline{d}^s$ ,  $\underline{d}^a$ ,  $\underline{d}^c$ ).

When it comes to the linear part of the velocity field, the spatial modes  $\underline{d}^s$  and  $\underline{d}^a$  can be computed extracting the velocity field in some strategic time steps of the load history (snapshots) presented in Figure 3.2. The point is to catch separately the effects of the normal and tangential loads. When these spatial modes are computed, both bodies behave like one, once they are calculated in time steps where the whole contact zone is in stick condition. This is the reason why  $\underline{v}^e$  is referred as linear, once that the nonlinear effects due to friction inside the slip zones are not taken into account in this term.

Once  $\underline{d}^s$  and  $\underline{d}^a$  are computed, the nonlocal intensity factors can be obtained through these decompositions:

$$\dot{I}^s(t) = \frac{\int_{\Omega} \underline{v} \cdot \underline{d}^s d\Omega}{\int_{\Omega} \underline{d}^s \cdot \underline{d}^s d\Omega} \quad (3.2)$$

$$\dot{I}^a(t) = \frac{\int_{\Omega} \underline{v} \cdot \underline{d}^a d\Omega}{\int_{\Omega} \underline{d}^a \cdot \underline{d}^a d\Omega} \quad (3.3)$$

where the domain of integration  $\Omega$  is depicted in Figure 3.2. The complementary part of the velocity field can be determined evaluating the residue of the velocity field approximation when only the linear part of the velocity field is considered.

$$\underline{v}^c(\underline{x}, t) = \underline{v}(\underline{x}, t) - \underline{v}^e(\underline{x}, t) \quad (3.4)$$

Once that  $\underline{v}^c$  is defined differently,  $\dot{I}^c(t)$  and  $\underline{d}^c(\underline{x})$  can be computed applying a Proper Orthogonal Decomposition (POD) to  $\underline{v}^c(\underline{x}, t)$ .

$$\underline{v}^c(\underline{x}, t) \underbrace{\simeq}_{\text{POD}} \dot{I}^c(t) \underline{d}^c(\underline{x}) \quad (3.5)$$



Note that, in this case, only the first mode of the decomposition is considered. For more details concerning the POD technique see Appendix B.

As well as the complementary part of velocity field, through a second POD, the spatial modes can be expressed in polar coordinates using a reference frame attached to the contact edge assuming that the geometry under analysis can be approximated as self-similar (scale invariant):

$$\underline{d}^s(\underline{x}) \rightarrow \underline{d}^s(r, \theta) \simeq f^s(r)\underline{g}^s(\theta) \quad (3.6)$$

$$\underline{d}^a(\underline{x}) \rightarrow \underline{d}^a(r, \theta) \simeq f^a(r)\underline{g}^a(\theta) \quad (3.7)$$

$$\underline{d}^c(\underline{x}) \rightarrow \underline{d}^c(r, \theta) \simeq f^c(r)\underline{g}^c(\theta) \quad (3.8)$$

where the radial and angular components of  $\underline{d}^s$  and  $\underline{d}^a$  are depicted in Figures 3.3 and 3.4, respectively.

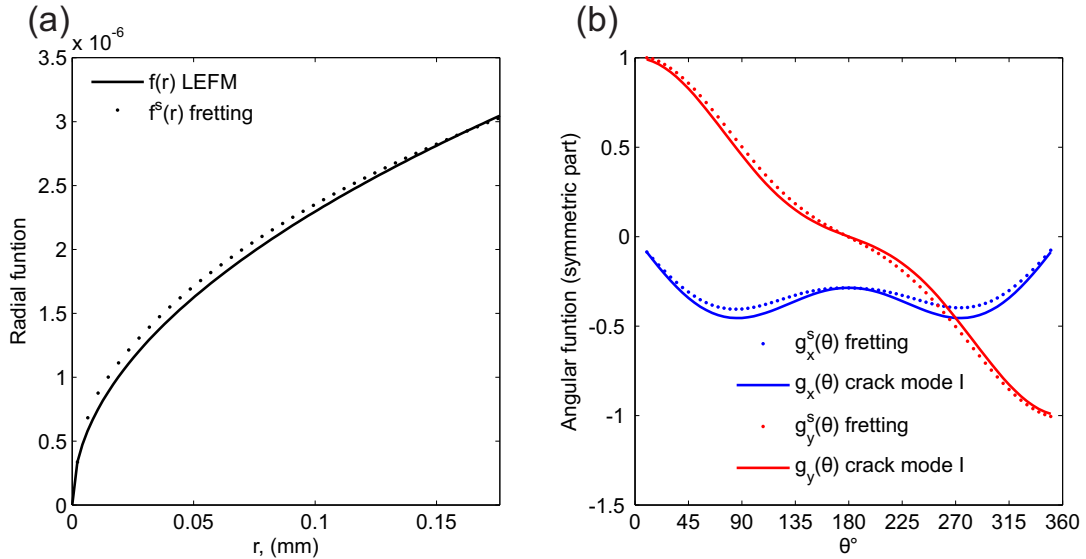


Figure 3.3: (a) Comparison between the radial evolution of  $\underline{d}^s$  and the radial evolution of the displacement field nearby a crack tip (mode I), (b) Comparison between the angular evolution of  $\underline{d}^s$  and the angular evolution of the displacement field nearby a crack tip (mode I).

A generic contact configuration may not respect the self-similar hypothesis, however the polar decomposition is applied within a circular region close enough to the contact edges such as self-similarity can be approximated. Note that the fretting spatial modes (points) are similar to the ones used to describe the mechanical fields close to crack tip in LEFM problems (solid lines), which confirms the crack analogy proposed by (Montebello et al., 2016). For the sake of brevity, the results concerning the complementary field will not be shown here, however, as presented in (Montebello et al., 2016), the radial component of  $\underline{d}^c$  decreases quickly when one moves away from the contact edge confirming the very localized effects of friction inside the slip zones. Knowing that, and pointing out

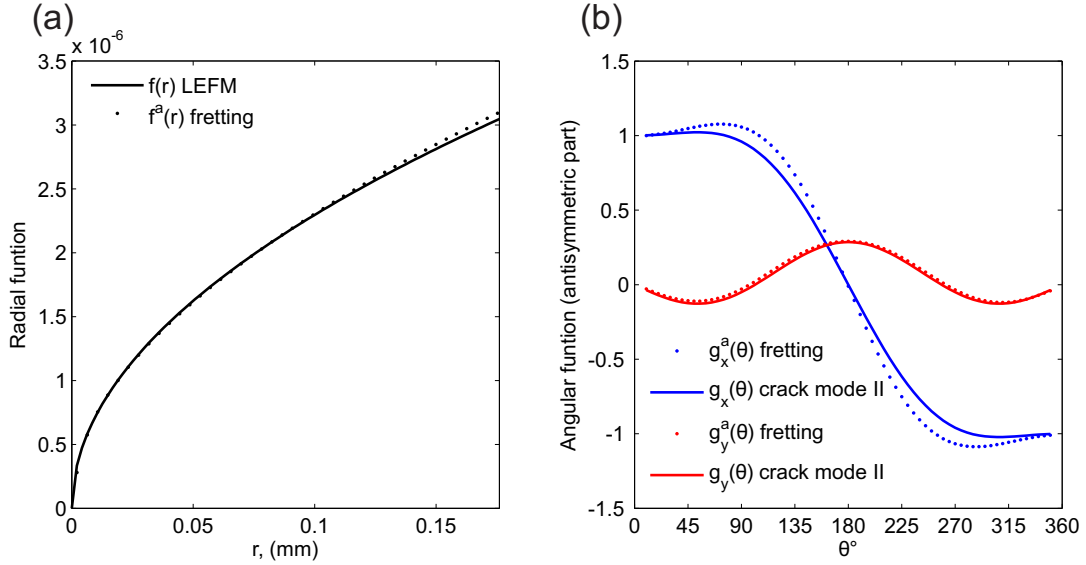


Figure 3.4: (a) Comparison between the radial evolution of  $\underline{d}^a$  and the radial evolution of the displacement field nearby a crack tip (mode II), (b) Comparison between the angular evolution of  $\underline{d}^a$  and the angular evolution of the displacement field nearby a crack tip (mode II).

that the angular functions coming from the complementary part are not so smooth as the ones coming from  $\underline{d}^s$  and  $\underline{d}^a$ , only these spatial modes will be used to enrich the fretting simulations.

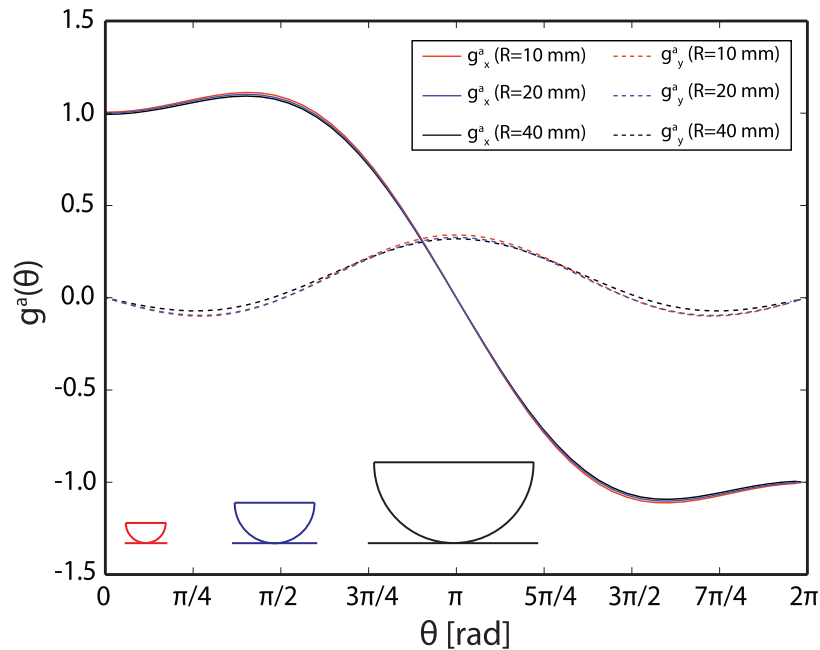


Figure 3.5: Comparison of  $g^a(\theta)$  for different geometries obtained varying the pad radius.

In addition, it has been shown in (Montebello, 2015) that, for different cylindrical

contact configurations, the reference functions which describe the spatial modes  $\underline{d}^s$ ,  $\underline{d}^a$  and  $\underline{d}^c$  can be regarded as the same. For instance, in Fig. 3.5, the angular functions coming from  $\underline{d}^a$  are plotted for different pad radii. This is an important result once that, for industrial applications, the contact geometries are not necessarily the cylindrical one. For example, the contact configuration present in the dovetail root of a fan blade root is better described by the rounded punch-on-flat contact set-up. Nevertheless, locally, close to the contact tip where the partition is applied, the contact geometry can be approximated as self-similar resulting in unchanged reference functions.

## 3.2 Enrichment technique

One of the main ideas of this work is to enrich fretting simulations using the spatial modes presented in the previous section. To accomplish that, the standard FE approximation will be enriched using the partition of unity framework as previously applied to LEFM problems in (Moës et al., 1999; Sukumar et al., 2000; Moës et al., 2002) and in particular to fretting problems in (Giner et al., 2008a, 2009; Pierres et al., 2011; Baietto et al., 2013; Giner et al., 2014), where the authors simulated the crack propagation under fretting conditions. However, note that, in the present work, cracks are not considered once the goal here is only to improve the accuracy of the stress computation close to the contact surfaces when fretting takes place as it has been done by (Giner et al., 2008b) for complete sliding contacts. In the standard FEM, the displacement field can be approximated and expressed as:

$$\underline{u} = \sum_{i \in I} N_i(\underline{x}) \underline{u}_i \quad (3.9)$$

where  $I$  is the set of all nodes discretizing the domain,  $\underline{u}_i$  is the displacement field at the node  $i$  and  $N_i$  is the corresponding basis function of this node. It is well known that the FE basis functions represents the partition of unity. The basic idea behind the X-FEM (see (Moës et al., 1999; Sukumar et al., 2001; Khoei, 2014)) is the multiplication of the nodal basis functions  $N_i(\underline{x})$  with some enrichment function  $\psi(\underline{x})$ , where this function, in general, is capable of capturing some previous known behaviour of the problem studied. Defining  $J$  as the subset of enriched nodes,  $J \subset I$ , the enriched approximation of the displacement field using the partition of unity can be expressed as:

$$\underline{u}(\underline{x}) = \sum_{i \in I} N_i(\underline{x}) \underline{u}_i + \sum_{j \in J} N_j(\underline{x}) \sum_{\alpha} \psi_{\alpha}(\underline{x}) \underline{b}_{j,\alpha} \quad (3.10)$$

where  $\psi_{\alpha}$  are the set of enriched functions at each enriched node  $j \in J$  multiplying the new degrees of freedom  $\underline{b}_{j,\alpha}$ . This approach permits us to inherit some properties of the FE basis functions, such as their compact support, and hence preserving the advantages of the standard FEM, such as the symmetry and sparsity of the stiffness matrix.

As it has been shown in Section 3.1, the mechanical fields around the contact edges in fretting problems are similar to the ones found close to the crack tip in fracture mechanics problems. Therefore, it seems a reasonable idea to use the same analytical functions used to enrich the displacement field close to the crack tip in LEFM problems to enrich fretting simulations, where in this case, one has:

$$\psi_{\alpha} = \left\{ \sqrt{r} \sin \frac{\theta}{2}, \sqrt{r} \cos \frac{\theta}{2}, \sqrt{r} \sin \frac{\theta}{2} \sin \theta, \sqrt{r} \cos \frac{\theta}{2} \sin \theta \right\} \quad (3.11)$$

A linear combination of these enrichment functions can recover with high accuracy the distribution of the fretting spatial modes presented in Figs. 3.3 and 3.4 (Section 3.1). The actual spatial modes from the velocity field decomposition could also have been used in this setting, however, it would introduce less flexibility when composing the enrichment functions.

It is worth mentioning that, despite the self-similar behaviour found nearby the contact edges in the non-complete contact configuration here assessed, it is true that at the contact tip, there is no stress singularity like the ones in LEFM or complete contact problems. The mechanical fields at the contact tip in this type of smooth contact are more likely to behave like the ones found in the vicinity of blunt cracks Giannakopoulos et al. (2000). In this case, the asymptotic stress solution contains the regular sharp crack solution and an additional non-singular term Creager and Paris (1967). The enrichment functions (Eq. (3.11)) contain only the singular term, the non-singular term of the partition proposed in Eq. (3.1) is embodied in the complementary field  $\underline{d}^c$ , which is not used here due to its complexity and localized effects. However as will be seen in Section 3.4, it does not seem to introduce any anomalous behaviour to the fretting fields solution in the proximity of the contact edges. In addition, Giner et al. (2008b) verified that the order of the singularity ( $r^\beta$ ) in complete contacts was associated to parameters like the contact geometry, the friction coefficient and the stick/slip condition. Here the order of the singularity extracted directly from FE computations appeared to be 1/2 when considering only the linear response of the problem. An exponential term seems to govern the evolution of the complementary part that takes into account the nonlinearities inside the slip zones. In his work, Montebello et al. (2016) verified that considering only the linear description of the velocity field could lead to errors around 20% when trying to recover the actual velocity field extracted from FE computations. The magnitude of this error was related to the size of the slip zones which in his study represented up to around 40% of the contact total width. The use of the complementary part of the velocity field could make this error falls below 5%. Having said that, differently from what have been done in Giner et al. (2008b), an approximation have been done in order to choose the enrichment functions where these ones describes better the problem the smaller the slip zones are.

Figure 3.6 illustrates how the enrichment technique is applied in order to solve fretting problems, for more details concerning the X-FEM implementation see Appendix C. As can be seen, two different areas surrounding the contact edges are enriched. In these two regions the stress concentrations are the highest. The amount of elements enriched is controlled by the enrichment radius  $r_e$ . It is also possible to see three different types of elements. The fully enriched elements are the ones where all its nodes are enriched whereas the standard elements are enrichment free. The blended elements are composed of both enriched and standard nodes. It is worth mentioning that, in this kind of problem, where one has smooth non-complete contact configurations, which means that the width of the contact zone depends on the external applied loads, the position of the contact edges need to be known a priori in order to apply the enrichment technique.

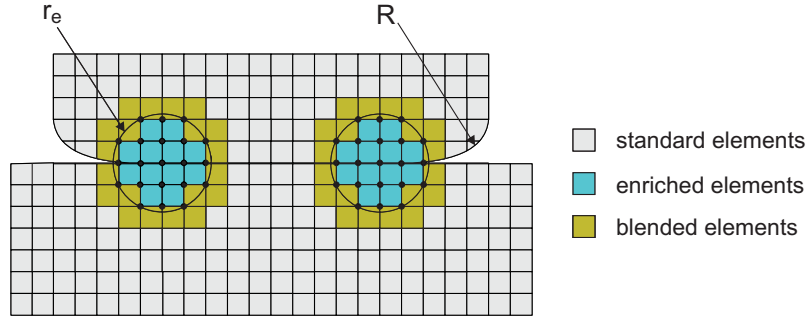


Figure 3.6: Enrichment scheme.

### 3.3 Contact aspects

In this work, the enrichment technique has been implemented inside an in-house FE element code, which consequently, made things easier to be implemented and tested. Nevertheless, the ideas and techniques used here can be readily reproduced using some of the commercial FE software available nowadays.

Regardless the enrichment procedure presented in the last section, the contact problem is solved in a standard way considering two deformable bodies coming into contact, Figure 3.7. In this case,  $\Omega^{(1)}$  and  $\Omega^{(2)}$  are the domains occupied by the bodies 1 and 2, respectively, with open boundaries that can be distinguished in three sets at a certain time  $t \in [0, T] \subset \mathbb{R}$ :

- $\Gamma_d^{(i)}$ : part of the boundary where displacements are prescribed.
- $\Gamma_\sigma^{(i)}$ : part of the boundary where external loads are prescribed.
- $\Gamma_c^{(i)}$ : part of the boundary where contact is likely to occur.

where the subscript “ $i$ ” denotes the bodies 1 and 2. We first define the notion of solution spaces  $\mathcal{U}_t^{(i)}$  and a weighting spaces  $\mathcal{V}_0^{(i)}$  as

$$\mathcal{U}_t^{(i)} = \left\{ \underline{u}_t^{(i)} : \Omega^{(i)} \rightarrow \mathbb{R}^2 \mid \underline{u}_t^{(i)} \in H^1(\Omega^{(i)}), \underline{u}_t^{(i)} = \underline{u}_d^{(i)} \text{ in } \Gamma_d^{(i)} \right\} \quad (3.12)$$

$$\mathcal{V}_0^{(i)} = \left\{ \underline{u}^{*(i)} : \Omega^{(i)} \rightarrow \mathbb{R}^2 \mid \underline{u}^{*(i)} \in H^1(\Omega^{(i)}), \underline{u}^{*(i)} = \underline{0} \text{ in } \Gamma_d^{(i)} \right\} \quad (3.13)$$

where  $\underline{u}_t^{(i)}$  is the displacement field at a given time  $t$  and  $\underline{u}^{*(i)}$  is the weight function. Assuming linear quasi-static conditions, the equilibrium equation of this problem can be expressed in terms of its weak formulation by:

$$\sum_{i=1}^2 \left( \int_{\Omega^{(i)}} \underline{\underline{\sigma}}^{(i)} : \underline{\underline{\varepsilon}}(\underline{u}^{*(i)}) d\Omega - \int_{\Gamma_\sigma^{(i)}} \underline{f}^{(i)} \cdot \underline{u}^{*(i)} d\Gamma - \int_{\Gamma_c^{(i)}} \underline{f}_c^{(i)} \cdot \underline{u}^{*(i)} d\Gamma \right) = 0, \quad (3.14)$$

$$\forall \underline{u}^{*(i)} \in \mathcal{V}_0^{(i)}$$

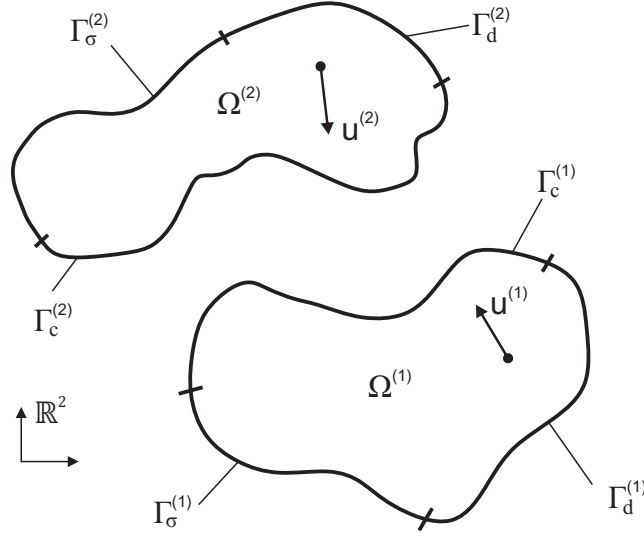


Figure 3.7: Contact problem two deformable bodies.

where  $\underline{\sigma}$  is the Cauchy stress tensor,  $\underline{\varepsilon}$  is the linear strain tensor,  $\underline{f}_{-ext}^{(i)}$  and  $\underline{f}_{-c}^{(i)}$  are the external and contact loads in each body, respectively.

Regarding the contact aspects, the first thing to be considered is the non-penetration condition, where the following relation must be respected:

$$(\underline{u}^{(2)} - \underline{u}^{(1)}) \cdot \underline{n} + g_0 \geq 0 \quad (3.15)$$

where  $\underline{n}$  is defined as the outward normal on the contact surface of the body 1, Figure 3.8. The normal initial gap between the two bodies is defined as  $g_0$ . When Eq. (3.15) is equal to zero, contact happens and the following relation is observed:

$$(\underline{f}_{-c}^{(1)} + \underline{f}_{-c}^{(2)}) \cdot \underline{n} = 0. \quad (3.16)$$

In this case, Coulomb's friction law with no regularization is used, where, if one has stick condition:

$$|\underline{f}_{-c}^{(1)} \cdot \underline{n}_t| < \mu |\underline{f}_{-c}^{(1)} \cdot \underline{n}| \quad (3.17)$$

and

$$(\underline{\dot{u}}^{(2)} - \underline{\dot{u}}^{(1)}) \cdot \underline{n}_t = 0 \quad (3.18)$$

where  $\mu$  is the friction coefficient,  $\underline{\dot{u}}^{(i)}$  is the velocity field on the contact zones and  $\underline{n}_t$  is defined as the tangential unitary vector to the contact surface in the body 1, Figure 3.8. On the other hand, if one has slip conditions:

$$|\underline{f}_{-c}^{(1)} \cdot \underline{n}_t| = \mu |\underline{f}_{-c}^{(1)} \cdot \underline{n}| \quad (3.19)$$

and  $\exists \dot{\gamma} > 0$  such that:

$$(\underline{\dot{u}}^{(2)} - \underline{\dot{u}}^{(1)}) \cdot \underline{n}_t = \dot{\gamma} \frac{\underline{f}_{-c}^{(1)} \cdot \underline{n}_t}{|\underline{f}_{-c}^{(1)} \cdot \underline{n}_t|} \quad (3.20)$$

and according to Newton's third law:

$$(\underline{f}_c^{(1)} + \underline{f}_c^{(2)}) \cdot \underline{n}_t = 0. \quad (3.21)$$

Considering Eq. (3.14) and the inequality constraints coming from the local contact problem formulation, Eqs. (3.15)-(3.21), it is clear that even under linear elastic conditions contacts problems are nonlinear and a wide range of optimization techniques can be used to solve these problems, being the most commonly used the penalty and Lagrange multiplier methods (Wriggers, 1995; Laursen, 2013; Yastrebov, 2013). Here a brief presentation of these two methods are presented.

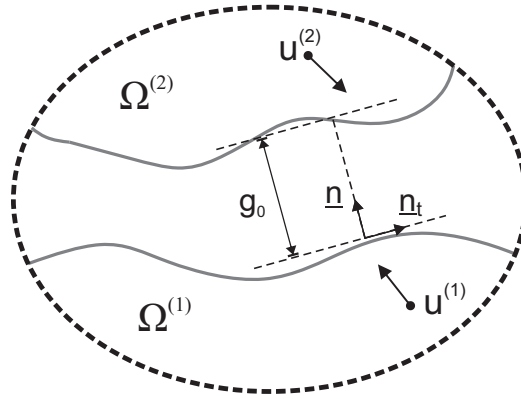


Figure 3.8: Local contact formulation.

### 3.3.1 Penalty method

The penalty method has the advantage of removing explicitly the contact constraints from the variational formulation which enables us to solve the problem as a simple unconstrained optimization problem. In this setting, the following potential penalty energy terms are added to the sum of the potential energy of each body:

$$\Pi^c := \frac{1}{2} \int_{\Gamma_c^{(1)}} \epsilon_N \langle g_N \rangle^2 d\Gamma + \frac{1}{2} \int_{\Gamma_c^{(1)}} \epsilon_T g_T^2 d\Gamma \quad (3.22)$$

where  $\epsilon_N$  and  $\epsilon_T$ , both positive, are the penalty parameters. The notation  $\langle * \rangle$  denotes the Macauley bracket operator. The normal and tangential gap function  $g_N$  and  $g_T$  are defined respectively as:

$$g_N = (\underline{u}^{(1)} - \underline{u}^{(2)}) \cdot \underline{n} - g_0 \leq 0 \quad (3.23)$$

$$g_T = (\underline{u}^{(2)} - \underline{u}^{(1)}) \cdot \underline{n}_t \quad (3.24)$$

The penalized energy functional can be expressed as:

$$\Pi^{pen}(\underline{u}^{(i)}) = \sum_{i=1}^2 \Pi^{(i)}(\underline{u}^{(i)}) + \Pi^c \quad (3.25)$$

where

$$\Pi^{(i)} = \frac{1}{2} \int_{\Omega^{(i)}} \underline{\underline{\sigma}}^{(i)} : \underline{\underline{\varepsilon}}^{(i)} d\Omega - \int_{\Gamma_{\sigma}^{(i)}} \underline{f}_{ext}^{(i)} \cdot \underline{u}^{(i)} d\Gamma \quad (3.26)$$

The weak form of the problem can then be established minimizing the penalized energy functional resulting in

$$\begin{aligned} & \sum_{i=1}^2 \left( \int_{\Omega^{(i)}} \underline{\underline{\sigma}}^{(i)} : \underline{\underline{\varepsilon}}(\underline{u}^{*(i)}) d\Omega - \int_{\Gamma_{\sigma}^{(i)}} \underline{f}_{ext}^{(i)} \cdot \underline{u}^{*(i)} d\Gamma \right) \\ & + \int_{\Gamma_c^{(1)}} \epsilon_N \langle g_N \rangle \delta g_N d\Gamma + \int_{\Gamma_c^{(1)}} \epsilon_T g_T \delta g_T d\Gamma = 0, \forall \underline{u}^{*(i)} \in \mathcal{V}_0^{(i)} \end{aligned} \quad (3.27)$$

that can be solved using Newton Raphson methods for instance. Expanding Eq. (3.27) it can be shown that contact tractions in the penalty formulation can be regarded as:

$$\begin{aligned} \underline{f}_c^{(1)} \cdot \underline{n} &= -\epsilon_N g_N \\ \underline{f}_c^{(1)} \cdot \underline{n}_t &= \epsilon_T g_T \end{aligned} \quad (3.28)$$

where the magnitude of  $\underline{f}_c^{(1)} \cdot \underline{n}_t$  is limited by Coulomb's friction law. Despite its simplicity, the penalty method presents some shortcomings. Impenetrability and Coulomb's friction law are only perfectly observed for  $\epsilon_N, \epsilon_T \rightarrow \infty$  which from a numerical point of view is not possible (ill-conditioning). Thus, the penalty method is not able to fulfil contacts constraints arbitrarily close, which depending on the problem assessed it may be an issue.

### 3.3.2 Lagrange multipliers method

Another method that can be used in order to enforce contact constraints is the Lagrange multipliers method. In this case, the following potential energy terms are added to the sum of the potential energy of each body:

$$\Pi^c := \int_{\Gamma_c^{(1)}} \lambda_N g_N d\Gamma + \int_{\Gamma_c^{(1)}} \lambda_T g_T d\Gamma \quad (3.29)$$

where  $\lambda_N$  and  $\lambda_T$  are the normal and tangential components of the Lagrange multipliers, respectively, and  $g_N$  and  $g_T$  are defined by Eqs. (3.23) and (3.24). Therefore, the solution of the contact problem can be obtained by finding the stationary point of the following functional:

$$\Pi^{lag}(\underline{u}^{(i)}) = \sum_{i=1}^2 \Pi^{(i)}(\underline{u}^{(i)}) + \int_{\Gamma_c^{(1)}} \lambda_N g_N d\Gamma + \int_{\Gamma_c^{(1)}} \lambda_T g_T d\Gamma \quad (3.30)$$

which results in

$$\begin{aligned} & \sum_{i=1}^2 \left( \int_{\Omega^{(i)}} \underline{\underline{\sigma}}^{(i)} : \underline{\underline{\varepsilon}}(\underline{u}^{*(i)}) d\Omega - \int_{\Gamma_{\sigma}^{(i)}} \underline{f}_{ext}^{(i)} \cdot \underline{u}^{*(i)} d\Gamma \right) + \int_{\Gamma_c^{(1)}} \lambda_N \delta g_N d\Gamma + \int_{\Gamma_c^{(1)}} \lambda_T \delta g_T d\Gamma \\ & + \int_{\Gamma_c^{(1)}} \lambda_N^* g_N d\Gamma + \int_{\Gamma_c^{(1)}} \lambda_T^* g_T d\Gamma = 0, \forall \underline{u}^{*(i)} \in \mathcal{V}_0^{(i)} \text{ and } \lambda_N \geq 0 \end{aligned} \quad (3.31)$$



This non-linear equation can be solved using Newton-like methods and also note that, as the constraint  $\lambda_N \geq 0$  needs to be fulfilled, the Lagrange multiplier method does not convert a minimization problem with inequalities constraint to a complete unconstrained one. It can also be seen that the Lagrange multipliers have physical meaning being  $\lambda_N$  and  $\lambda_T$ , respectively:

$$\begin{aligned} \underline{f}_c^{(1)} \cdot \underline{n} &= -\lambda_N \\ \underline{f}_c^{(1)} \cdot \underline{n}_t &= \lambda_T \end{aligned} \quad (3.32)$$

During the solution of this minimization problem,  $\lambda_T$  is bounded by Coulomb's friction law and in this case, Eq. (3.31) should be modified yielding

$$\begin{aligned} \sum_{i=1}^2 \left( \int_{\Omega^{(i)}} \underline{\underline{\sigma}}^{(i)} : \underline{\underline{\varepsilon}}(\underline{u}^{*(i)}) d\Omega - \int_{\Gamma_\sigma^{(i)}} \underline{f}_{ext}^{(i)} \cdot \underline{u}^{*(i)} d\Gamma \right) + \int_{\Gamma_c^{(1)}} \lambda_N \delta g_N d\Gamma + \int_{\Gamma_c^{(1)}} (\underline{f}_c^{(1)} \cdot \underline{n}_t) \delta g_T d\Gamma \\ + \int_{\Gamma_c^{(1)}} \lambda_N^* g_N d\Gamma = 0, \forall \underline{u}^{*(i)} \in \mathcal{V}_0^{(i)} \text{ and } \lambda_N \geq 0 \end{aligned} \quad (3.33)$$

One of the main advantages of the Lagrange multiplier method is that it fulfils exactly the local contact conditions, however it makes the problem to be solved larger, and sometimes convergence might become a hard task. Another important difficulty associated with the Lagrange multipliers approach is the determination of the active constraints which is surely a nontrivial exercise. For a more rigorous formulation of the Lagrange multipliers in the context of contact problems the reader is referred to (Kikuchi and Oden, 1988).

### 3.3.3 Contact formulation adopted in this chapter

In this chapter, a search direction iterative method was used to find the set of solutions verifying the admissible displacement field satisfying Eq. (3.14) and the set of contact admissibility equations (Eqs. (3.15) to (3.21)). Integrations over time were performed using backward Euler. In case of gross slip, the connectivity between contact surfaces was updated at each time step, once that, in this case, appreciable amounts of relative slip between the contacting surfaces are observed. Although in this work gross slip under large tangential displacement has been assessed, linear hypothesis were always assumed (elastic response and small deformations), once that, large rotations and plasticity were not experienced in the simulations. Note that Coulomb's friction law always limits the shear stress developed close to the contact surfaces.

In this case, let one considers two contact bodies  $\Omega^{(1)}$  and  $\Omega^{(2)}$  where contact and friction may occur along their contact interfaces  $\Gamma_c^{(1)}$  and  $\Gamma_c^{(2)}$ , Figure 3.7. This contact problem can be divided in a global problem, written at the  $\Omega^{(i)}$  scale, and a local problem, written at the  $\Gamma_c^{(i)}$  scale. The global problem is defined with its own variables, the displacement field  $\underline{u}^{(i)}$  and the Cauchy stress tensor  $\underline{\underline{\sigma}}^{(i)}$ . Similarly, the local contact problem can be defined by its own variables  $\underline{w}^{(i)}$  and  $\underline{f}_c^{(i)}$ , the displacement field at the contact interfaces and the contact tractions respectively. The coupling between the global and the local problems can be ensured through:

$$\underline{u}^{(i)} = \underline{w}^{(i)} \text{ on } \Gamma_c^{(i)} \quad (3.34)$$

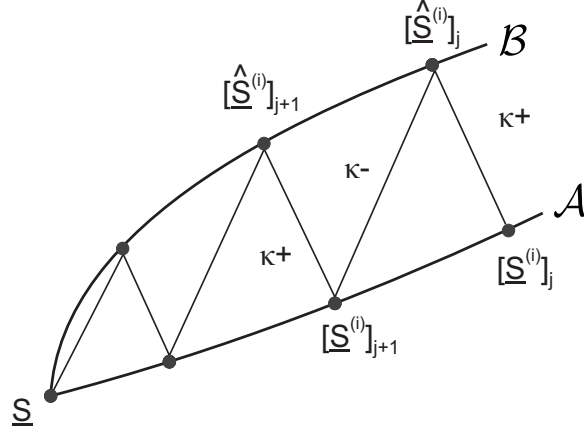


Figure 3.9: LATIN scheme.

Under small displacement and deformation assumptions, as already shown in (Pierres et al., 2010; Gravouil et al., 2011), the weak formulation of the contact problem at a given time  $t \in [0; T]$  can be expressed as (absence of body forces):

$$\begin{aligned} \sum_{i=1}^2 \left( \int_{\Omega^{(i)}} \underline{\underline{\sigma}}^{(i)} : \underline{\underline{\varepsilon}}(\underline{u}^{*(i)}) d\Omega - \int_{\Gamma_{\sigma}^{(i)}} \underline{f}^{(i)} \cdot \underline{u}^{*(i)} d\Gamma - \int_{\Gamma_c^{(i)}} \underline{f}_c^{(i)} \cdot \underline{w}^{*(i)} d\Gamma \right. \\ \left. - \int_{\Gamma_c^{(i)}} \underline{\lambda}^{*(i)} \cdot (\underline{u}^{(i)} - \underline{w}^{(i)}) d\Gamma - \int_{\Gamma_c^{(i)}} \underline{\lambda}^{(i)} \cdot (\underline{u}^{*(i)} - \underline{w}^{*(i)}) d\Gamma \right) = 0 \end{aligned} \quad (3.35)$$

where in a 2D framework

$$\underline{u}^{(i)} \in \mathcal{U}^{(i)} = \left\{ \underline{u}^{(i)} : \Omega^{(i)} \rightarrow \mathbb{R}^2 \mid \underline{u}^{(i)} \in H^1(\Omega^{(i)}), \underline{u}^{(i)} = \underline{u}_d^{(i)} \text{ in } \Gamma_d^{(i)} \right\} \quad (3.36)$$

$$\underline{u}^{*(i)} \in \mathcal{V}_0^{(i)} = \left\{ \underline{u}^{*(i)} : \Omega^{(i)} \rightarrow \mathbb{R}^2 \mid \underline{u}^{*(i)} \in H^1(\Omega^{(i)}), \underline{u}^{*(i)} = \underline{0} \text{ in } \Gamma_d^{(i)} \right\} \quad (3.37)$$

$$\underline{w}^{(i)} \in \mathcal{W}^{(i)}, \underline{w}^{*(i)} \in \mathcal{W}^{(i)} = \{ \underline{w}^{(i)} \in H^1(\Gamma_c^{(i)}) \} \quad (3.38)$$

$$\underline{\lambda}^{(i)} \in \Lambda^{(i)}, \underline{\lambda}^{*(i)} \in \Lambda^{(i)} = \{ \underline{\lambda}^{(i)} \in L^2(\Gamma_c^{(i)}) \} \quad (3.39)$$

where  $\underline{\lambda}$  is a Lagrange multiplier field. The quantities  $\underline{w}^{(i)}$  and  $\underline{f}_c^{(i)}$  should obey the relations described in Eqs. (3.15)-(3.21), where Eq. (3.34) retains its validity.

In order to solve Eq. (3.35), firstly, one assumes that the following variables are known at time  $t_{k-1}$ :  $\underline{u}_{k-1}^{(i)}$ ,  $\underline{\sigma}_{k-1}^{(i)}$ ,  $\underline{w}_{k-1}^{(i)}$ ,  $\underline{f}_{c,k-1}^{(i)}$ . Within a quasi-static incremental framework, the the solution of the problem at  $t_k$  can be computed through a search direction approach likewise the LATIN method (Ladevèze et al., 2010; Ladevèze, 2012; Giacomini et al., 2014), Figure 3.9. Briefly, this method consists in a separation of the linear and nonlinear equations of the problem studied. In this setting,  $\mathcal{A}$  denotes the set of solutions  $\underline{S}_k^{(i)} = (\underline{w}_k^{(i)}, \underline{f}_{c,k}^{(i)})$  satisfying the linear constitutive law, kinematic and static admissibility,

whereas  $\mathcal{B}$ , is the set of solutions  $\hat{\underline{S}}_k^{(i)} = (\hat{\underline{w}}_k^{(i)}, \hat{\underline{f}}_{c,k}^{(i)})$  verifying the local contact admissibility equations. A two-staged iterative algorithm can then be settled, where at the  $j^{th}$  iteration, the global stage consists in finding  $[\underline{S}_k^{(i)}]_{j+1} \in \mathcal{A}$ , with a search direction:

$$[\underline{f}_{c,k}^{(i)}]_{j+1} - [\hat{\underline{f}}_{c,k}^{(i)}]_j = -\kappa([\underline{w}_k^{(i)}]_{j+1} - [\hat{\underline{w}}_k^{(i)}]_j) \quad (3.40)$$

then the local stage consists in finding  $[\hat{\underline{S}}_k^{(i)}]_{j+1} \in \mathcal{B}$ :

$$[\hat{\underline{f}}_{c,k}^{(i)}]_{j+1} - [\underline{f}_{c,k}^{(i)}]_{j+1} = \kappa([\hat{\underline{w}}_k^{(i)}]_{j+1} - [\underline{w}_k^{(i)}]_{j+1}) \quad (3.41)$$

where  $\kappa$  is the search direction parameter which has only influence in the rate of convergence of the method.

Replacing Eq. (3.40) into Eq. (3.35):

$$\begin{aligned} \sum_{i=1}^2 \left( \int_{\Omega^{(i)}} [\underline{\sigma}_k^{(i)}]_{j+1} : \underline{\underline{\varepsilon}}(\underline{u}^{*(i)}) d\Omega - \int_{\Gamma_\sigma^{(i)}} \underline{f}_{ext}^{(i)} \cdot \underline{u}^{*(i)} d\Gamma - \int_{\Gamma_c^{(i)}} \left( [\hat{\underline{f}}_{c,k}^{(i)}]_j + \kappa[\hat{\underline{w}}_k^{(i)}]_j \right) \cdot \underline{w}^{*(i)} d\Gamma \right. \\ \left. + \int_{\Gamma_c^{(i)}} \kappa[\hat{\underline{w}}_k]_{j+1} \cdot \underline{w}^{*(i)} d\Gamma - \int_{\Gamma_c^{(i)}} \underline{\lambda}^{*(i)} \cdot ([\underline{u}_k^{(i)}]_{j+1} - [\underline{w}_k^{(i)}]_{j+1}) d\Gamma \right. \\ \left. - \int_{\Gamma_c^{(i)}} [\underline{\lambda}_k^{(i)}]_{j+1} \cdot (\underline{u}^{*(i)} - \underline{w}^{*(i)}) d\Gamma \right) = 0 \end{aligned} \quad (3.42)$$

Introducing the FEM discretization to Eq. (3.42) the following linear system is yielded (global stage).

$$\begin{bmatrix} \mathbf{K} & \mathbf{0} & -\mathbf{K}_{u\lambda} \\ \mathbf{0} & \mathbf{K}_{ww} & \mathbf{K}_{w\lambda} \\ -\mathbf{K}_{u\lambda}^T & \mathbf{K}_{w\lambda}^T & \mathbf{0} \end{bmatrix} \begin{bmatrix} \mathbf{U}_{j+1} \\ \mathbf{W}_{j+1} \\ \mathbf{\Lambda}_{j+1} \end{bmatrix} = \begin{bmatrix} \mathbf{F}_{ext} \\ \mathbf{F}_c \\ \mathbf{0} \end{bmatrix} \quad (3.43)$$

The following relative error indicator may be used (Ribeaucourt et al., 2007) as a stop criterion for a given time instant  $t_k$ :

$$\eta = \sqrt{\frac{\|\underline{S}_k^{(i+1)} - \hat{\underline{S}}_k^{(i)}\|}{\|\underline{S}_k^{(i+1)}\| + \|\hat{\underline{S}}_k^{(i)}\|}} < tol \quad (3.44)$$

According to (Trollé et al., 2012) a stabilization operator can be introduced to Eq. (3.43) reducing spurious oscillations on the dual fields. Eq. (3.43) then becomes:

$$\begin{bmatrix} \mathbf{K} & \mathbf{0} & -\mathbf{K}_{u\lambda} \\ \mathbf{0} & \mathbf{K}_{ww} & \mathbf{K}_{w\lambda} \\ -\mathbf{K}_{u\lambda}^T & \mathbf{K}_{w\lambda}^T & \mathbf{K}_{\lambda\lambda} \end{bmatrix} \begin{bmatrix} \mathbf{U}_{j+1} \\ \mathbf{W}_{j+1} \\ \mathbf{\Lambda}_{j+1} \end{bmatrix} = \begin{bmatrix} \mathbf{F}_{ext} \\ \mathbf{F}_c \\ \mathbf{K}_{\lambda\lambda} \mathbf{\Lambda}_j \end{bmatrix} \quad (3.45)$$

where

$$\mathbf{K}_{\lambda\lambda} = -\zeta \int_{\Gamma_c} \chi_i \chi_j d\Gamma \quad (3.46)$$

and  $\zeta$  is the stabilization parameter and  $\chi$  the shape function associated to the Lagrange multipliers. Note that at convergence,  $\mathbf{K}_{\lambda\lambda}\mathbf{\Lambda}_{j+1} - \mathbf{K}_{\lambda\lambda}\mathbf{\Lambda}_j$  approaches  $\mathbf{0}$ .

It is worth mentioning that, despite the similarity with the conventional LATIN formulation, the problem here studied is solved incrementally for each time step, where the admissible solutions are obtained time step by time step.

Given the solution of the global stage  $[\underline{S}_k^{(i)}]_{j+1}$ , which satisfy kinematic and static admissibility conditions, the local stage can be faced as an updating stage taking place along the contact surfaces. Therefore, at each contact node, frictional contact conditions must be verified making use of the search direction relation expressed by Eq. (3.41). In order to solve the local stage explicitly, let one first defines the following contact indicators for the normal interactions:

$$C_n = \frac{1}{2} \left( [\underline{f}_{c,k}^{(1)}]_{j+1} - [\underline{f}_{c,k}^{(2)}]_{j+1} \right) \cdot \underline{n} + \frac{\kappa}{2} \left[ \left( [\underline{\hat{w}}_k^{(2)}]_{j+1} - [\underline{\hat{w}}_k^{(1)}]_{j+1} \right) \cdot \underline{n} + g_0 \right] \quad (3.47)$$

Using the search direction relation expressed in Eq. (3.41),  $C_n$  can be rearranged as:

$$C_n = \frac{1}{2} \left( [f_{c,k}^{(1)}]_{j+1} - [f_{c,k}^{(2)}]_{j+1} \right) \cdot \underline{n} + \frac{\kappa}{2} \left[ \left( [w_k^{(2)}]_{j+1} - [w_k^{(1)}]_{j+1} \right) \cdot \underline{n} + g_0 \right] \quad (3.48)$$

Notice that in this relation, only informations provided by the linear stage are needed. Similarly, a tangential contact indicator can be defined as:

$$\begin{aligned} C_t = \frac{1}{2} \left( [\underline{f}_{c,k}^{(1)}]_{j+1} - [\underline{f}_{c,k}^{(2)}]_{j+1} \right) \cdot \underline{n}_t + \frac{\kappa}{2} \left[ \left( [\underline{\hat{w}}_k^{(2)}]_{j+1} - \underline{\hat{w}}_{k-1}^{(2)} \right) - \left( [\underline{\hat{w}}_k^{(1)}]_{j+1} - \underline{\hat{w}}_{k-1}^{(1)} \right) \right] \cdot \underline{n}_t = \\ \frac{1}{2} \left( [f_{c,k}^{(1)}]_{j+1} - [f_{c,k}^{(2)}]_{j+1} \right) \cdot \underline{n}_t + \frac{\kappa}{2} \left[ \left( [w_k^{(2)}]_{j+1} - \underline{\hat{w}}_{k-1}^{(2)} \right) - \left( [w_k^{(1)}]_{j+1} - \underline{\hat{w}}_{k-1}^{(1)} \right) \right] \cdot \underline{n}_t \end{aligned} \quad (3.49)$$

Note that, the choice of  $C_n$  and  $C_t$  were made judiciously, such that, if there is contact

$$C_n = [\underline{f}_{c,k}^{(1)}]_{j+1} \cdot \underline{n} \leq 0 \quad (3.50)$$

otherwise, there is no contact and  $C_n > 0$ . For the tangential indicator, if  $|C_t| \leq \mu|C_n|$  stick condition is observed and

$$C_t = [\underline{f}_{c,k}^{(1)}]_{j+1} \cdot \underline{n}_t \quad (3.51)$$

otherwise, slip occurs and the tangential load is limited by Coulomb's friction law. Table 3.1 summarizes the explicit solutions of the local stage, where the subscripts  $k$  and  $j+1$  were dropped for the sake of brevity.

It is worth mentioning that the convergence of the iterative method here presented strongly depends on the parameters  $\kappa$  and  $\zeta$ . In previous uses of the LATIN method to solve contact problems (Champaney et al., 1999; Cognard et al., 1996), the search direction parameter was defined through the following relation:

$$\kappa = E/L_0 \quad (3.52)$$

where  $E$  is the Young's modulus and  $L_0$  is a characteristic length of the structure. In their structure assembly analysis (Champaney et al., 1999; Cognard et al., 1996), near

Table 3.1: Solution of the local stage.

if $C_n > 0$ (no contact)	
$\hat{f}_c^{(1)} = \hat{f}_c^{(2)} = 0$	
$\hat{w}^{(1)} = \underline{w}^{(1)} - \underline{f}_c^{(1)}/\kappa$	
$\hat{w}^{(2)} = \underline{w}^{(2)} - \underline{f}_c^{(2)}/\kappa$	
if $C_n \leq 0$ (contact)	
$\hat{f}_c^{(1)} \cdot \underline{n} = -\hat{f}_c^{(2)} \cdot \underline{n} = C_n$	
$\hat{w}^{(1)} \cdot \underline{n} = \underline{w}^{(1)} \cdot \underline{n} + (\hat{f}_c^{(1)} - \underline{f}_c^{(1)}) \cdot \underline{n}/\kappa$	
$\hat{w}^{(2)} \cdot \underline{n} = \underline{w}^{(2)} \cdot \underline{n} + (\hat{f}_c^{(2)} - \underline{f}_c^{(2)}) \cdot \underline{n}/\kappa$	
if $ C_t  < \mu C_n $ (stick condition)	if $ C_t  \geq \mu C_n $ (slip condition)
$\hat{f}_c^{(1)} \cdot \underline{n}_t = -\hat{f}_c^{(2)} \cdot \underline{n}_t = C_t$	$\hat{f}_c^{(1)} \cdot \underline{n}_t = -\hat{f}_c^{(2)} \cdot \underline{n}_t = \mu C_n C_t/ C_t $
$\hat{w}^{(1)} \cdot \underline{n}_t = \underline{w}^{(1)} \cdot \underline{n}_t + (\hat{f}_c^{(1)} - \underline{f}_c^{(1)}) \cdot \underline{n}_t/\kappa$	$\hat{w}^{(1)} \cdot \underline{n}_t = \underline{w}^{(1)} \cdot \underline{n}_t + (\hat{f}_c^{(1)} - \underline{f}_c^{(1)}) \cdot \underline{n}_t/\kappa$
$\hat{w}^{(2)} \cdot \underline{n}_t = \underline{w}^{(2)} \cdot \underline{n}_t + (\hat{f}_c^{(2)} - \underline{f}_c^{(2)}) \cdot \underline{n}_t/\kappa$	$\hat{w}^{(2)} \cdot \underline{n}_t = \underline{w}^{(2)} \cdot \underline{n}_t + (\hat{f}_c^{(2)} - \underline{f}_c^{(2)}) \cdot \underline{n}_t/\kappa$

optimum values for  $\kappa$  were obtained setting  $L_0$  as the structure maximum length. In the case of frictional cracks,  $L_0$  was set as the crack length (Ribeaucourt, 2006). In this work, however, optimum values for  $\kappa$  were obtained defining  $L_0$  as the contact semi-width, whereas,  $\zeta$  was chosen according to (Trollé et al., 2012):

$$\zeta = \frac{1}{\kappa} \quad (3.53)$$

## 3.4 Results and discussions

### 3.4.1 Fretting under partial slip conditions

In order to check the improvements in the fretting simulations when making use of the crack analogy presented in Section 3.1, the problem depicted in Figure 3.10 will be assessed. In this case, a vertical monotonic displacement,  $u_y$ , presses the cylindrical pad, of radius  $R = 40$  mm, against the specimen that is fixed on the bottom and on both lateral sides. After that, a tangential sinusoidal displacement is imposed on the pad ensuring fretting conditions. The total normal load,  $P$ , and the total tangential load,  $Q$ , developed at the contact interfaces always obey the relation  $Q/P < \mu$ , where  $\mu$  is the friction coefficient between the contact surfaces. However, locally, slip zones may be observed. All the simulations considered in this work will be confined to the linear quasi-static case, where the material Young's modulus,  $E$ , is 200 GPa and the Poisson's ratio,  $\nu$ , is 0.3. The procedure used to enrich the simulations is presented in Section 3.2. The contact problem, implemented via MATLAB, is solved according to the formulation presented in Subsection 3.3.3. The friction problem is formulated using the Coulomb's friction law with a friction coefficient  $\mu = 0.9$ . As can be seen in Figure 3.10, the finite element discretization far from the contact surfaces consists of linear triangular elements, whereas linear quadrangular elements are used to discretize the neighbourhood of the contact surfaces.

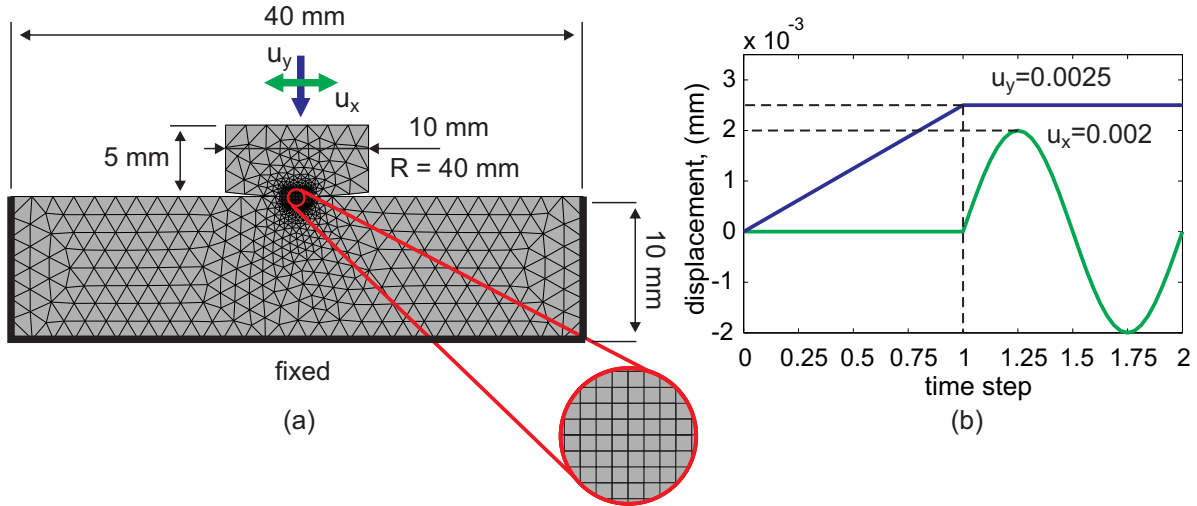


Figure 3.10: (a) Fretting model under partial slip, (b) fretting under partial slip load history.

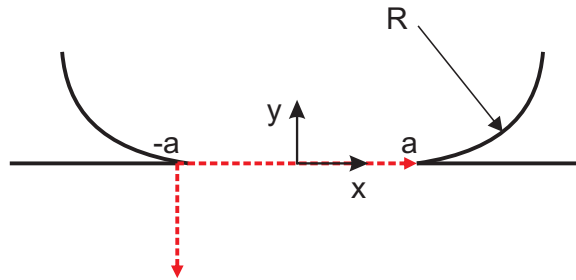


Figure 3.11: Directions of stress evaluation.

Three different simulations were confronted in order to check the improvements obtained through the enrichment technique. The first one, the reference solution, was performed considering the standard FEM. In this case, a fine mesh was used (0.0025 mm), around 180 elements discretizing the contact zone. The second one was also conducted considering the standard FE framework. However, in this case, a relatively coarse mesh was considered (0.025 mm), around 18 contact elements discretizing the contact zones, which in this case, is compatible with engineering facilities when performing simulation on real components as the dovetail connection between blades and discs in aeronautical compressors (SAFRAN). Finally, a third simulation was carried out, but now the enrichment technique was applied. In this case, the mesh discretization used is the same one used in the coarse standard FE simulation (0.025 mm). It is worth mentioning that, this simplified study case admits analytical solution, see Section 2.7, and that, the size of the mesh refinement in the reference solution is the one needed to recover with a good accuracy the analytical solution of this problem, Figure 3.12. In order to compare these three simulations, the stress distributions were assessed in two different directions, firstly along the contact surfaces ( $y = 0$ ) and secondly inward the contact in the vertical direction at the left contact edge ( $x = -a$  and  $y \leq 0$ ), Figure 3.11. Note that “ $a$ ” is the semi-width of the contact zone. The stress distributions were assessed at the time step where  $u_x = u_{x,max}$ , where in this case,  $u_{x,max}$  is the maximum value achieved by the prescribed

tangential displacement.

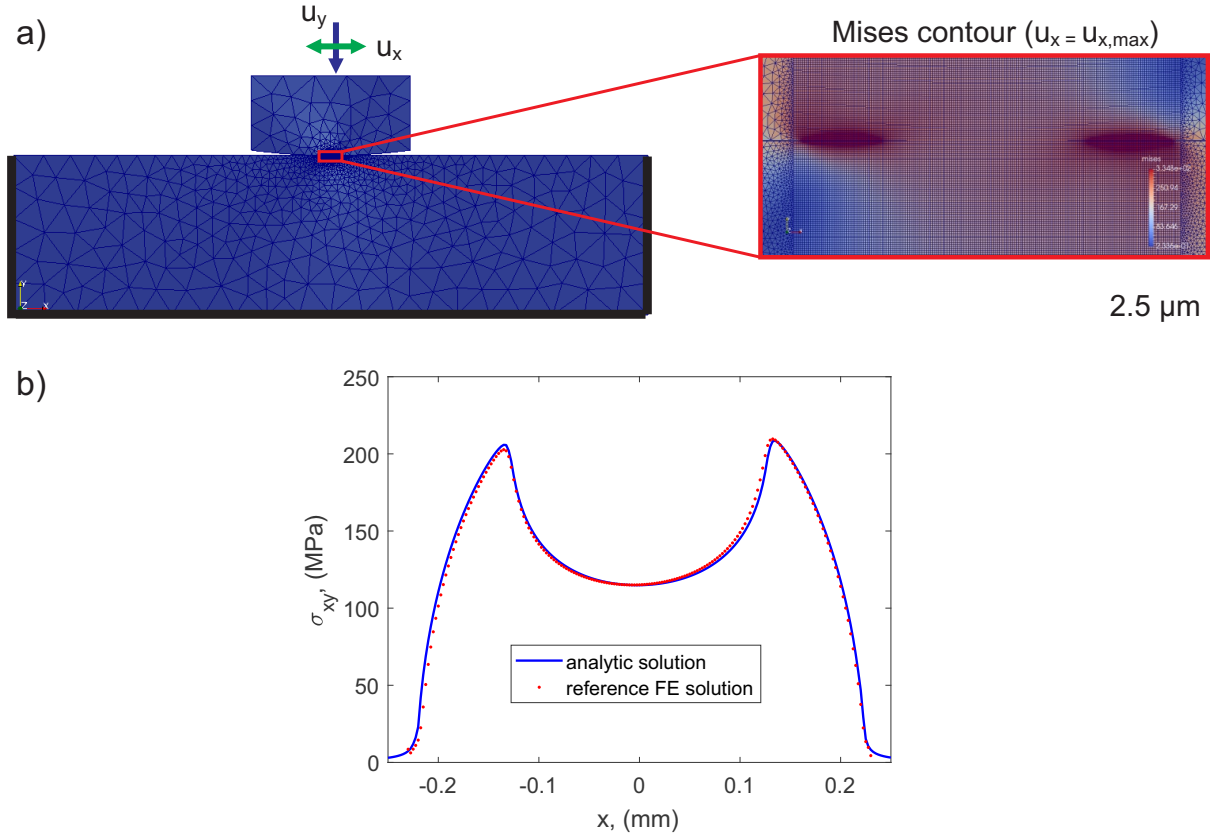


Figure 3.12: Reference solution of the fretting problem: (a) FE model and von Mises contour at  $u_x = u_{x,max}$ , (b) comparison between analytical and reference solution of the problem investigated for the  $\sigma_{xy}$  stress component along the contact surface ( $u_x = u_{x,max}$ ).

In order to improve the accuracy of the FE computations within the enriched elements, these ones were subdivided in  $n \times n$  sub-domains, where in each sub-domain, four Gauss points were considered in order to integrate the FE stiffness matrix, Figure 3.13. In this study, convergence was achieved when  $8 \times 8$  sub-domains were considered in each enriched element.

In Figures 3.14 and 3.15 the  $\sigma_{xx}$  and  $\sigma_{xy}$  stress components of the three simulations are compared. The reference solution is depicted by the black lines, the coarse standard simulation by the blue ones, while the enriched one is depicted by the red lines. In Figure 3.14, the stress distribution is assessed along the contact surface while Figure 3.15 depicts the results for the stress distribution inwards the contact. As can be seen, the enrichment technique can improve considerably the quality of the results, mainly when one analyses the  $\sigma_{xy}$  stress component along the contact surface. Note that, using the enrichment technique, it was possible to work with a mesh 10 times coarser than the one for the reference solution without losing quality. The enrichment radius considered in these simulations was  $0.6a$ . This value will be discussed in the next subsection.

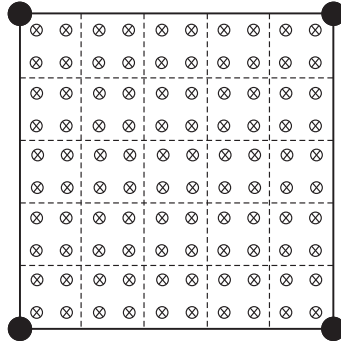


Figure 3.13: Gauss points integration scheme.

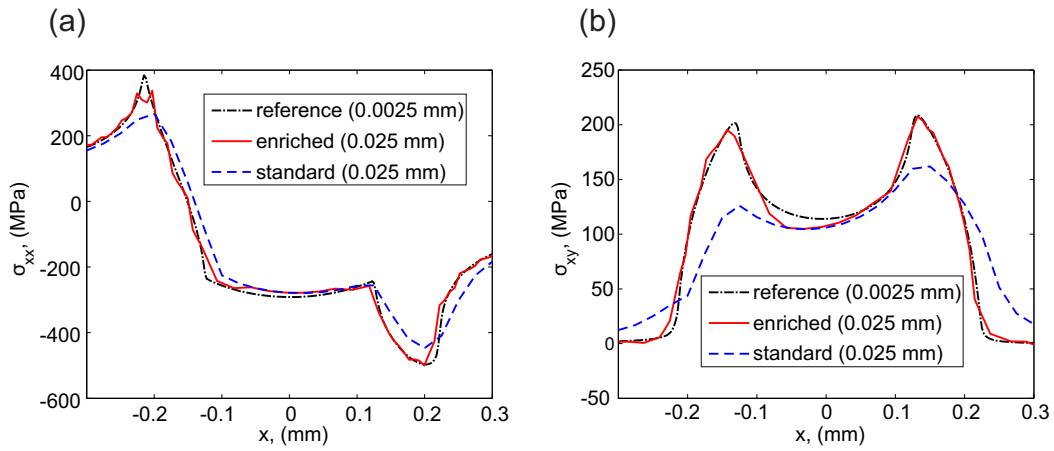


Figure 3.14: (a)  $\sigma_{xx}$  stress component ( $y = 0, u_x = u_{x,max}$ ), (b)  $\sigma_{xy}$  stress component ( $y = 0, u_x = u_{x,max}$ ).

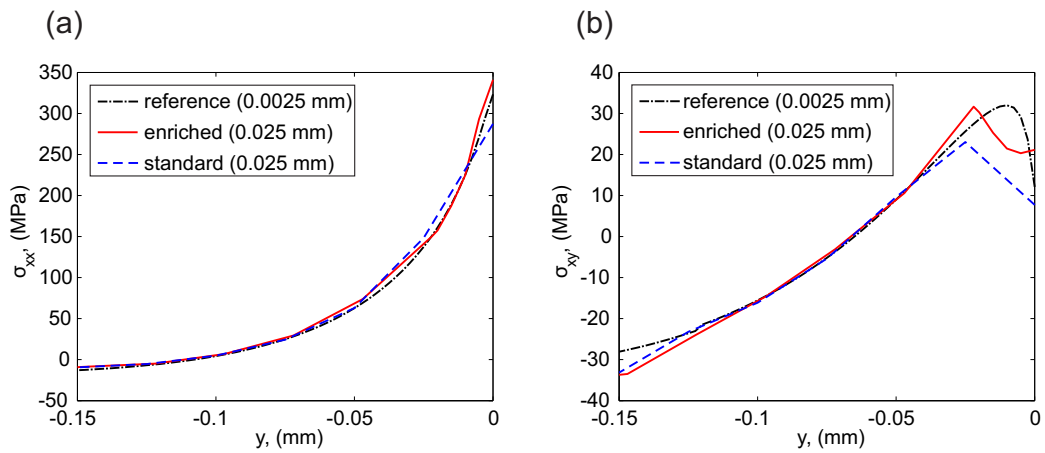


Figure 3.15: (a)  $\sigma_{xx}$  stress component ( $x = -a, y < 0, u_x = u_{x,max}$ ), (b)  $\sigma_{xy}$  stress component ( $x = -a, y < 0, u_x = u_{x,max}$ ).

To quantify the improvements obtained when using the enrichment technique, different



simulations considering different mesh sizes were performed. Some of these simulations were also performed making use of the enrichment fields. To measure these gains, a numerical error was defined, where the  $\sigma_{xy}$  stress component along the contact surface obtained numerically in each simulation was compared with the one obtained analytically. The  $\sigma_{xy}$  stress component was evaluated at the time instant where  $u_x = u_{x,max}$ .

$$\xi = \frac{\sqrt{\sum_{k \in K} (\sigma_{xy}^n(\underline{x}_k) - \sigma_{xy}^a(\underline{x}_k))^2}}{\sqrt{\sum_{k \in K} \sigma_{xy}^a(\underline{x}_k)^2}} \quad (3.54)$$

where  $K$  denotes the set of contact nodes on the specimen. Figure 3.16(a) depicts the numerical error expressed by Eq. (3.54) for different mesh sizes. It is possible to see that the enrichment technique considerably improves the quality of the results when the same mesh size is considered (for example, from nearly 35% to less than 10% for the mesh of 0.025 mm). The improvement is higher the coarser the meshes are. In Figure 3.16(b), the numerical error is also assessed, but this time, it was compared with the elapsed time in each simulation. Again, it is possible to see a noticeable time-saving when the enrichment technique is applied (for example, for an error of around 10%, the enriched simulation was 16 times faster).

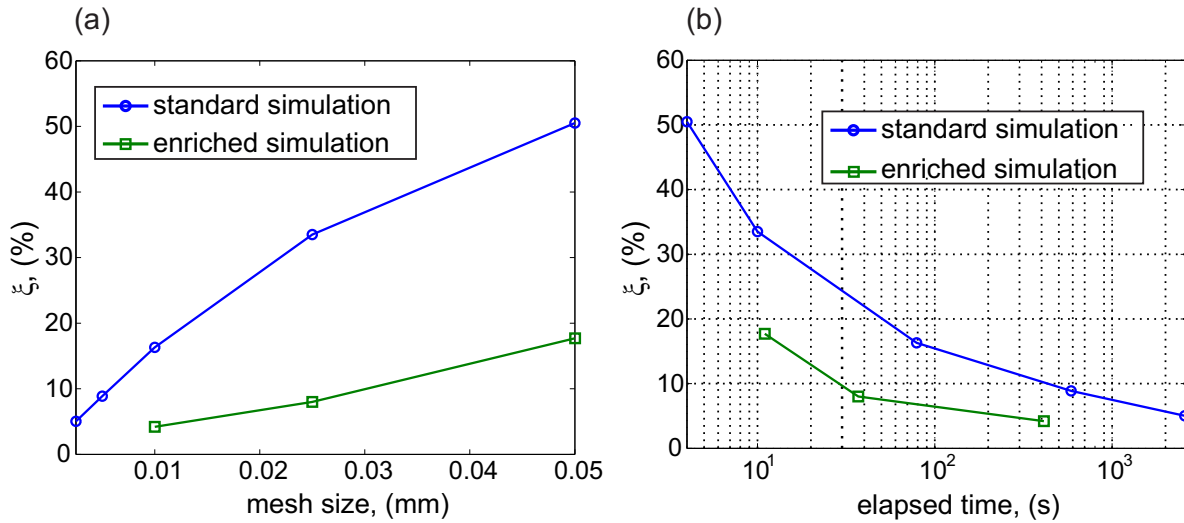


Figure 3.16: (a) numerical error expressed by means of the size of mesh, (b) numerical error expressed by means of the elapsed time in each simulation.

This work was more focused on a proof of concept of the enrichment technique presented in Section 3.2. Therefore, convergence rate analysis of the method are not rigorously conducted here. However, from Figure 3.16, it is possible to see that, standard and enriched simulations provided similar rates of convergence. Note as well that, the enrichment technique in this work is employed in a whole fixed area surrounding the contact edges, strategy similar to that applied to cracked problem in (Laborde et al., 2005) in an attempt to find optimal rate of convergence with the X-FEM (even though the X-FEM improves accuracy of solutions, blending elements are responsible for lack of optimal convergence rate).

### 3.4.2 Enrichment radius sensitivity

A question that may raise in this approach is how many elements surrounding the contact edges should be enriched. A study was conducted where different simulations were carried out. In these simulations, the only parameter changed was the enrichment radius. The results are presented in Figure 3.17, where the  $\sigma_{xx}$  stress component when  $u_x = u_{x,max}$  is plotted against the distance from the surface at  $x = -a$ .

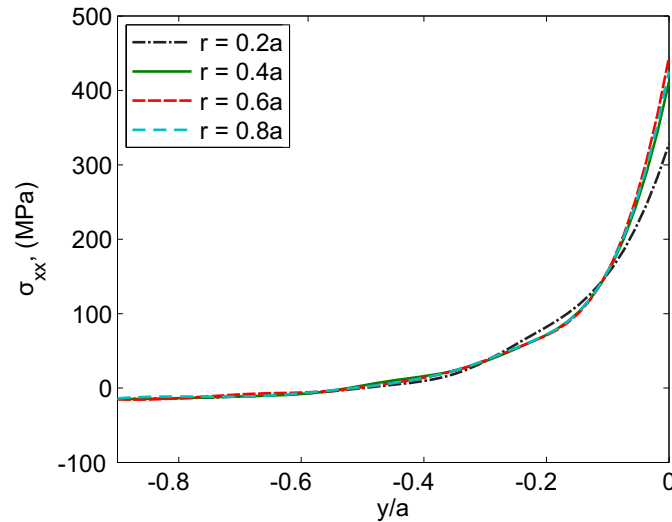


Figure 3.17: Variation of  $\sigma_{xx}$  when  $u_x = u_{x,max}$  against distance from the surface ( $x/a = -1$ ) for different enrichment radii.

The external loads considered here are the same as the ones presented in Figure 3.10. The mesh considered was again the same as the previous coarse enriched simulation (0.025 mm). As can be seen in Figure 3.17, for enrichment radii higher than  $0.4a$ , the results remain nearly the same, which means that, in order to apply the enrichment technique to capture the strong stress gradient, usually present in fretting problems, there is no need to enrich large regions.

### 3.4.3 Fretting under gross slip conditions

In the previous subsections, all the simulations were confined under partial slip conditions, which means that during the entire time domain evaluated, the position of the contact edges remained the same during the simulations. In this subsection, the issue is to check if the enrichment technique used up to this point works well when gross slip is present. In this case, one needs to track the position of the contact edges in order to enrich locally the model. For this purpose, a problem very similar to the one depicted in the Figure 3.10(a) will be assessed, however, now, gross slip needs to be taken into account. The displacement history depicted in Figure 3.18(a) will be considered, where, in this case, after the static vertical displacement,  $u_y$ , a large monotonic tangential displacement,  $u_x$ , is applied to the pad ensuring gross slip conditions. Further, the tangential displacement,  $u_x$ , starts varying sinusoidally ensuring partial slip conditions. Even-though large tangential displacements

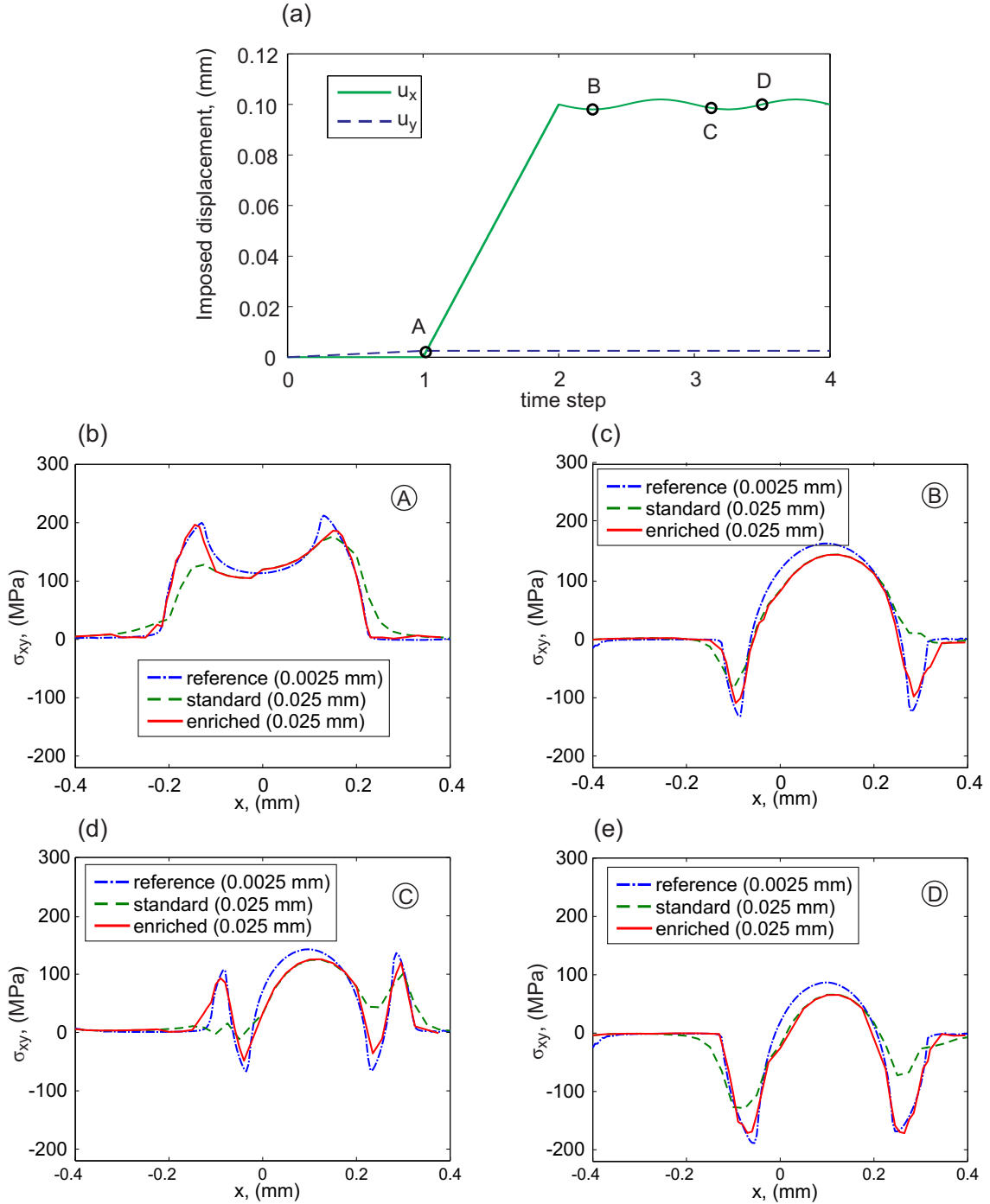


Figure 3.18: (a) Prescribed displacement history in gross slip,  $\sigma_{xy}$  stress component at time steps (b) A, (c) B, (d) C and (e) D.

were here considered, linear elastic simulations under small deformations were always assumed. It was possible once that, contact tractions are limited by Coulomb's friction law, where for the study case evaluated in this work, contact stresses remains inside the elastic domain.

Again, a reference solution performed on a fine mesh (0.0025 mm) through the standard FEM was compared with two other coarse simulations (0.025 mm), one of them

considering the enrichment technique and the other one without any enrichment. The results are depicted in Figure 3.18, where the  $\sigma_{xy}$  stress component is evaluated at the contact surface for different time steps. At this point, the position of the contact edges were assumed to be known in order to apply the enrichment multiscale approach. This information could be obtained from the reference solution of the problem.

Figure 3.18(a) depicts the displacement history considered in this analysis. At the time step A (Figure 3.18(b)), the tangential displacement is not high enough to cause gross slip. In this case we have two slip zones in the extremities of the contact surface and a central stick zone. At the time steps B (Figure 3.18(c)), C (Figure 3.18(d)) and D (Figure 3.18(e)), partial slip is also observed, but in these cases one can see that the contact surface was shifted to the right, once that, during the monotonic increase of the external tangential displacement gross slip was observed. Regarding these results, one can see that, whenever the enrichment technique is considered, a good improvement in the results is observed. The enriched simulations could recover with a good accuracy the results obtained through the reference solution, where the mesh used was 10 times finer. Regarding the results obtained by the standard coarse FE simulation, the response was not very accurate.

### 3.4.4 Contact status identification through nonlocal intensity factors

As presented in Section 3.1, the nonlocal intensity factors  $I^s$  and  $I^a$  are related to compressive and tangential loads, respectively. The idea is that these nonlocal parameters are capable of providing some information concerning the contact status. In order to check what happens with  $I^a$  and  $I^s$  when gross slip is present, a model very similar to the one presented in the last subsection (Fretting under gross slip conditions) will be assessed, however, in this case, the amplitude of the tangential displacement during the sinusoidal phase is greater (0.02 mm), Figure 3.19(a). It will ensure gross slip conditions most of the loading cycle.

Results were then obtained performing a standard FE simulation. The mesh discretization used here is very similar to the ones used so far, Figure 3.10, where, in this case, the size of the refined mesh surrounding the contact surface is 0.0025 mm. The results coming from this simulation will be also used as our reference solution hereinafter. Figure 3.19(b) depicts the slip zone semi-width over time. Note that “ $c$ ” is the semi-width of the stick zone and that when  $(a - c)/a$  is equal to 1, gross slip occurs. In Figure 3.19(c), one can observe that the nonlocal intensity factor,  $I^a$ , the one related with tangential effects, is always upper and lower bounded, which means that whenever gross slip is present, its value is limited. This behaviour can be described using a generalization of Coulomb’s friction law (Montebello et al., 2016):

$$|I^a| \leq \tilde{\mu}|I^s| \quad (3.55)$$

where,  $\tilde{\mu}$ , can be regarded as a nonlocal “friction coefficient”. Figure 3.19(d) confirms that when gross slip is present  $|I^a| = \tilde{\mu}|I^s|$ , on the other hand, under partial slip conditions  $|I^a| < \tilde{\mu}|I^s|$ . This behaviour suggests that, it is possible to link these nonlocal quantities,  $I^s$  and  $I^a$ , with the contact status of the problem which can speed up the simulations and permit a better application of the enrichment fields when gross slip is present. In order to

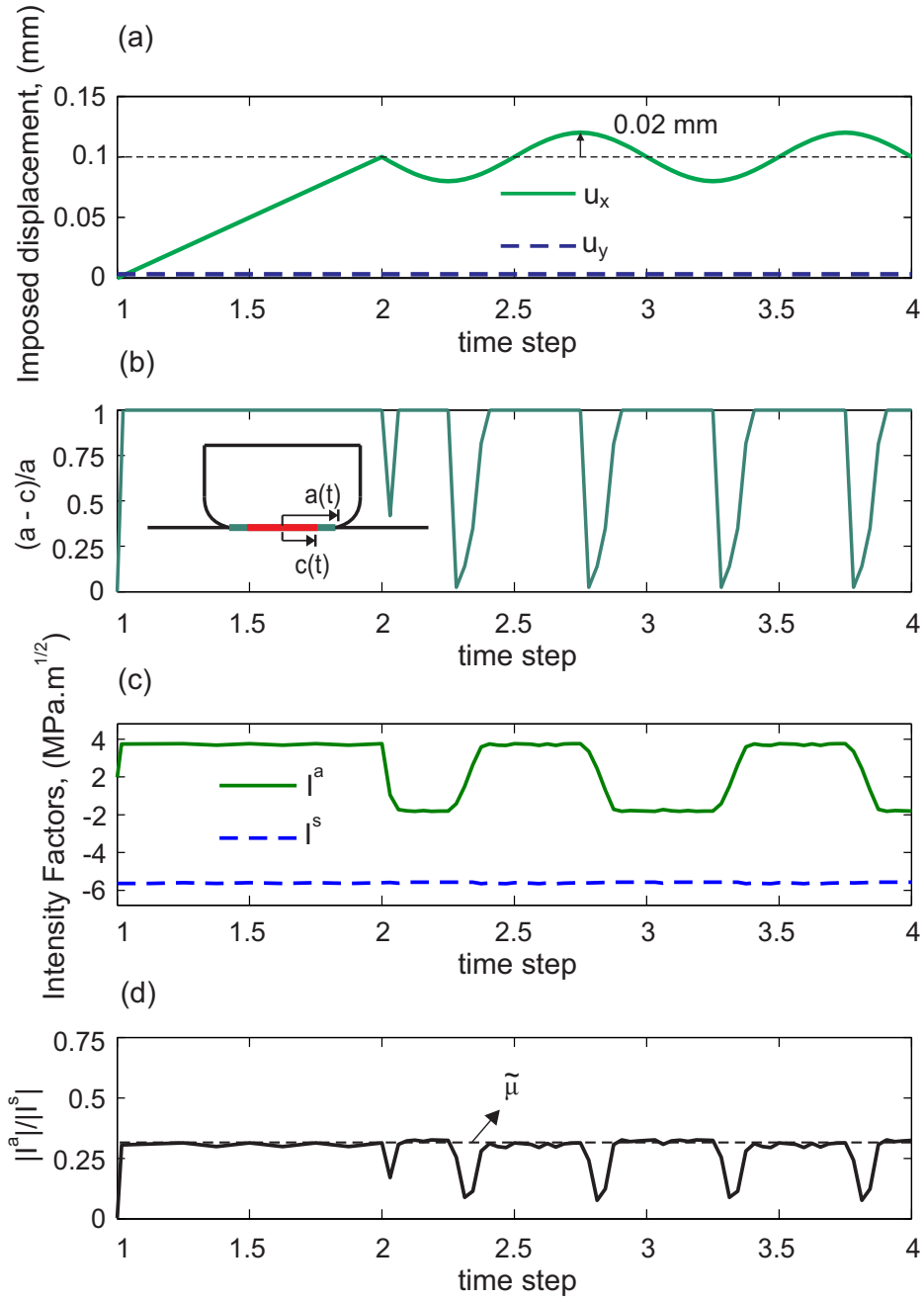


Figure 3.19: (a) Prescribed displacement history used to check the nonlocal intensity factors behaviour under gross slip conditions, (b) contact slip zone semi-width over time, (c) nonlocal intensity factors evolution over time, (d)  $|I^a|/|I^s|$  over time.

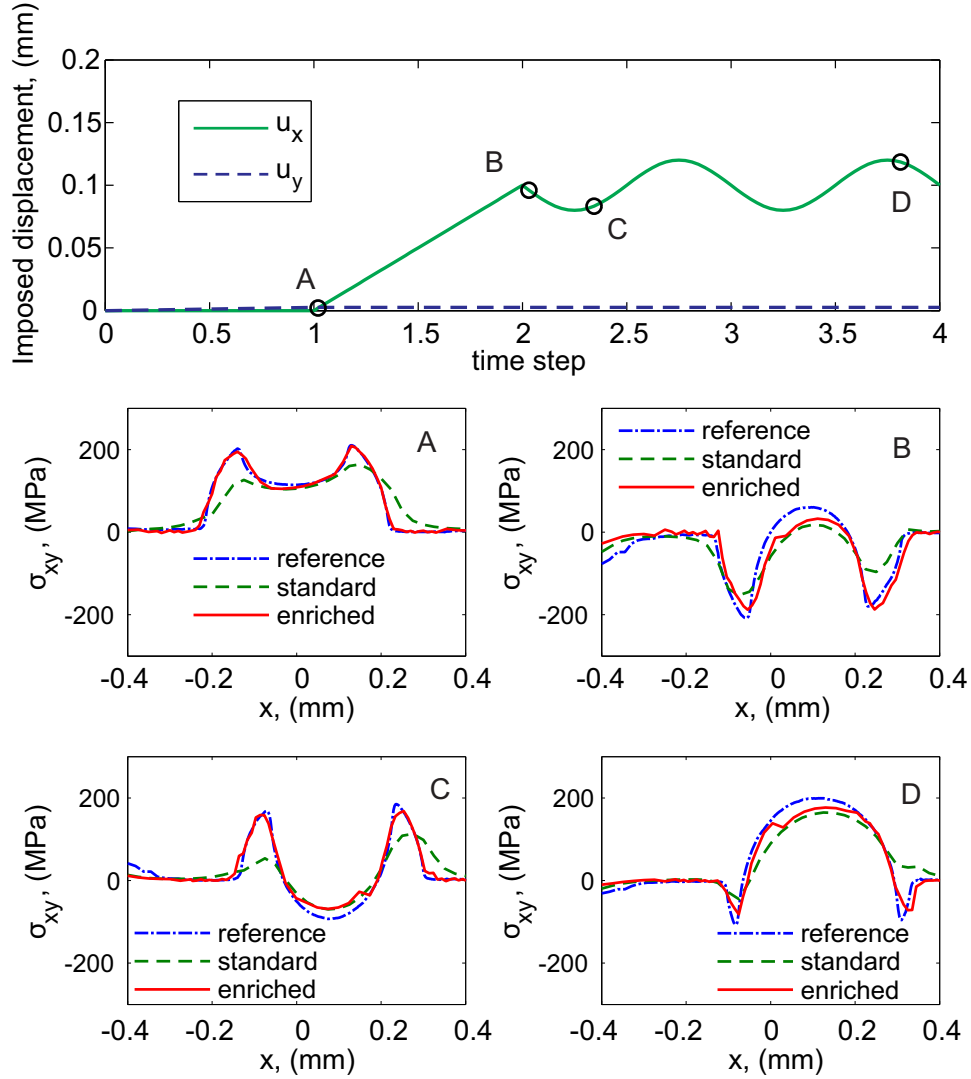


Figure 3.20:  $\sigma_{xy}$  stress component along the contact surface for different time steps when gross slip is predominantly observed.

verify that, the same problem presented in Figure 3.19(a) was solved again. However, now, two coarse simulations (0.025 mm) were performed. One of them considering the standard FE method and the other one making use of the enrichment technique. In the enriched case, during the solution of the contact problem, in the end of each time step iteration, the nonlocal intensity factors were computed and the relation expressed by Eq. (3.55) was checked. In case of  $|I^a| < \tilde{\mu}|I^s|$  the local contact problem in the next time step was solved normally as presented in Subsection 3.3.3. However if  $|I^a| = \tilde{\mu}|I^s|$ , gross slip was assumed, and the contact front was shifted by the same amount of the imposed external displacement increment at that time step preserving all other contact parameters. Note that this assumption is possible due to fact that the problem studied here considers two elastic bodies under small deformations. In Figure 3.20, the  $\sigma_{xy}$  stress component on the contact surface is depicted for different time steps for the three different simulations. The reference solution is depicted by the blue lines, the coarse standard one by the green lines and the enriched one by the red ones. As can be seen, a good improvement is observed in the results when the enrichment technique is used in association with the nonlocal IF that

were used to track the position of the contact edges. In this case, the major advantages are that during the gross slip phases, the problem does not need to be iteratively solved which save a significant amount of time, and at the same time, when the enrichment technique is being used, the position of the contact edge can be readily obtained ensuring that the enrichments field are being used in the right place. Note that in this case, just the initial information about the precise position of the contact edges needs to be known.

Further studies are still in progress in an attempt to link the nonlocal intensity factors  $I^s$ ,  $I^a$  and  $I^c$  with some local quantities as the size of the stick/slip zones as well as the position of the contact edges. With those informations the enrichment technique will become more independent of prior informations about the contact front. Note that it would not be a problem if we were dealing with complete contact problems, those ones where the position of the contact edges do not depend on the applied external loads.

### 3.4.5 PGD strategy to enhance performance

For the enrichment technique proposed in this work, under gross sliding conditions, the position of the contact edges are constantly changing. Since the enrichment functions are computed with respect to a reference frame attached to the contact edges, every time that the contact edges experience appreciable displacements, the enriched part of the FE element stiffness matrix needs to be recomputed. Even tough it was not deeply verified in this work, an attempt to describe the stiffness matrix of enriched elements by using the proper generalized decomposition (PGD) (Néron and Ladevèze, 2010; Ladevèze et al., 2010; Chinesta et al., 2011) was briefly tested in this work. The idea then is to use the PGD to build a library during a learning stage, which will allow the fast recovering of the enriched part of the stiffness matrix for a given element during actual simulations.

Therefore, consider a simple quadrangular element of sizes  $L$  with its center expressed in polar coordinates as depicted in Figure 3.21. In this case, denoting the enriched part of the stiffness matrix of this element by  $\mathbf{K}^{enr}(r, \theta, L, M)$ , where  $M$  refers to material properties, the PGD yields an approximate solution of the form:

$$\mathbf{K}^{enr}(r, \theta, L, M) \approx \sum_{i=1}^n f_i(r) \mathbf{g}_i(\theta) h_i(L) m_i(M) \quad (3.56)$$

In order to verify the applicability of this approach, the simplest case was investigated, where the size of the elements nearby the contact edges and the material properties were assumed constant, i.e.

$$\mathbf{K}^{enr}(r, \theta) \approx \sum_{i=1}^n f_i(r) \mathbf{g}_i(\theta) \quad (3.57)$$

In this setting, only the functions  $f_i(r)$  and  $\mathbf{g}_i(\theta)$  need to be determined. Then, the form of these functions can be obtained by the following relations:

$$f_i(r) = \int_{\theta} \left( \mathbf{K}^{enr}(r, \theta) - \sum_{k=1}^{i-1} f_k(r) \mathbf{g}_k(\theta) \right) : \mathbf{g}_i(\theta) d\theta / \int_{\theta} \mathbf{g}_i(\theta) : \mathbf{g}_i(\theta) d\theta \quad (3.58)$$

$$\mathbf{g}_i(\theta) = \int_r \left( \mathbf{K}^{enr}(r, \theta) - \sum_{k=1}^{i-1} f_k(r) \mathbf{g}_k(\theta) \right) f_i(r) dr / \int_r f_i(r)^2 dr \quad (3.59)$$

where these equations can be solved throughout a fixed point iteration scheme.

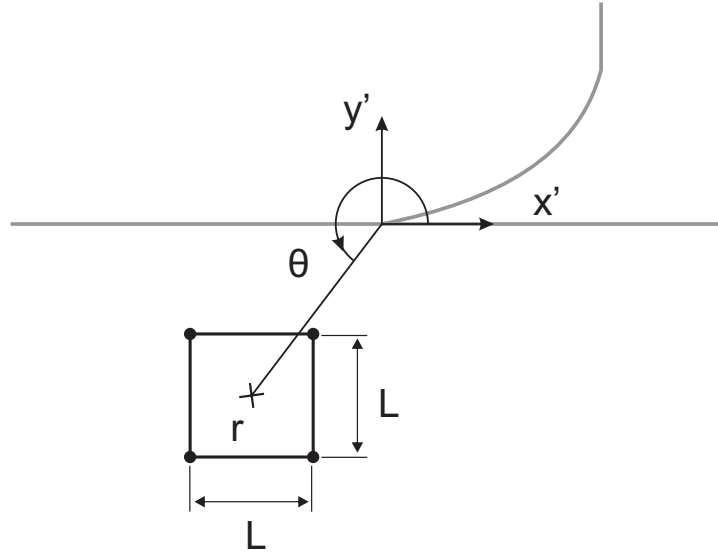


Figure 3.21: Reference frame PGD description.

For the FE model considered in the previous subsections and for an element of size equal to 0.025 mm, the error of the approximation expressed by Eq. (3.57) in terms of the number of functional products is depicted in Figure 3.22. As can be seen, only a few terms (around 5) are already enough to build our library. It is worth noting that, the introduction of more variables will increase the number of terms needed, however, it will probably be advantageous yet.

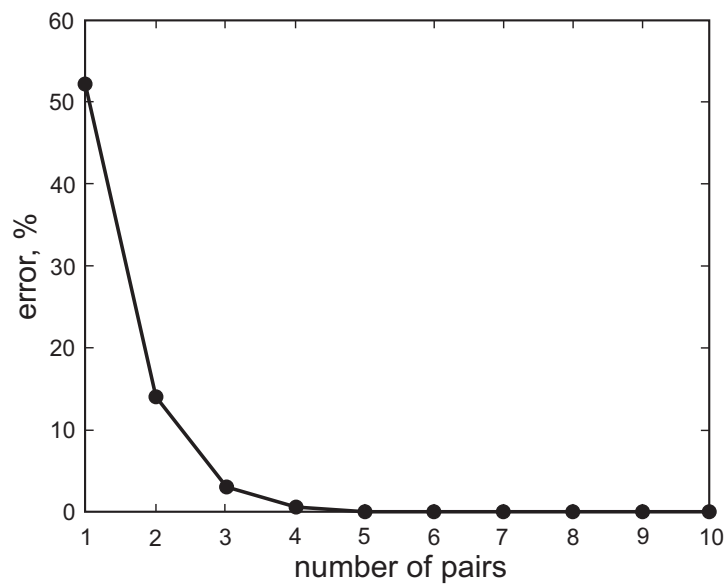


Figure 3.22: PGD error in terms of the number of functional pairs.



## 3.5 Chapter highlights

In this chapter, an enrichment-based approach for the simulation of fretting problems was proposed and tested. The enrichment functions here used were obtained through the crack analogue approach presented in (Montebello, 2015; Montebello et al., 2016) where it can be observed that the mechanical fields close to the contact edges in fretting problems are close to the ones near the crack tip in LEFM problems. Taking advantage of this similarity, closed form enrichment functions were used in order to enrich fretting simulations by using the X-FEM allowing us to capture the strong stress gradient nearby the contact edges. Both partial and gross slip regimes were assessed. Results have shown that, without appreciable loss of accuracy, the enrichment technique can considerably improve the quality of the results allowing the use of meshes up to 10 times coarser than those utilized when performing standard FE simulations, which consequently reduces computational costs.

The nonlocal intensity factors  $I^a$  and  $I^s$  coming from the crack analogue approach presented in Section 3.1 have also shown to be good indicators of the problem contact status. In this setting, those were used in order to track the position of the contact edges when gross slip takes place, which permits to apply the enrichment technique in the right place.

# Chapter 4

## Wear effects on fretting fatigue life estimate

In this chapter, the influence of the material removal due to wear when estimating fretting fatigue life under partial slip condition is addressed. Details concerning the numerical model and the contacting surfaces update are provided. Multiaxial fatigue life assessments and experimental data are compared.

### 4.1 Contextualization

Fretting fatigue life prediction approaches generally neglect wear effects when partial slip conditions are predominant (Araujo and Nowell, 2002; Hattori et al., 2003; Araujo et al., 2004; Navarro et al., 2008; Araújo et al., 2017). However, the contact surface evolution due to wear, over the fretting cycles, may lead to appreciable changes in the stress field distributions caused by the contact loads (McColl et al., 2004; Ding et al., 2004). As most of the works done so far concerning life prediction for fretting problems rely on stress based models, considering wear effects may change life predictions. Madge et al. (2007a,b) took into account wear effects in order to estimate fatigue life for a titanium alloy and could capture efficiently the detrimental wear effect under partial slip conditions and a beneficial one when gross sliding was observed. Under gross sliding conditions, cracks are worn out before they even start growing. This chapter will focus on the analysis of fretting fatigue data undertaken at the University of Brasilia by (Ferry, 2017; Ferry et al., 2017) for the titanium alloy Ti-6Al-4V. The main idea here is to compare life predictions regarding wear effects with the ones obtained when wear is neglected. All the analysis are carried out under the partial slip regime (PSR).

### 4.2 Wear numerical modelling and damage accumulation

As presented in Section 2.4, wear can be computed locally by using the Archard's law, Eq. (2.2) or the friction energy local law, Eq. (2.4). Those equations can be readily

implemented in the context of a FE code. Thus, the total required number of wear cycles (loading cycles),  $N_t$ , can be split in  $n_w$  wear blocks, where each block corresponds to  $\Delta N$  wear cycles, i.e.  $n_w = N_t/\Delta N$ . From a practical point of view, it would not be feasible in many situations to simulate each wear cycle. In this case, a strategy commonly adopted is to compute the wear during a fretting cycle and then multiply it by the jumping factor  $\Delta N$  assuming that the wear is nearly constant for  $\Delta N$  wear cycles. Doing so, the contact surface of the problem can be updated on a nodal basis after the application of the  $i^{th}$  wear block  $\Delta N$  as follows:

- Archard's law:

$$\Delta h_{i,j} = \sum_{k=1}^{n_{inc}} \kappa_w p(x_j, t_k) \Delta s(x_j, t_k) \Delta N \quad (4.1)$$

- Frictional dissipated energy:

$$\Delta h_{i,j} = \sum_{k=1}^{n_{inc}} \alpha q(x_j, t_k) \Delta s(x_j, t_k) \Delta N \quad (4.2)$$

where  $\Delta h_{i,j}$  is the wear depth increment of the node  $j$  located at the contact surface,  $\kappa_w$  is the local wear coefficient,  $\alpha$  is the energy wear coefficient and  $n_{inc}$  is the total number of load increments over a fretting cycle. The contact variables  $p(x_j, t_k)$ ,  $q(x_j, t_k)$  and  $\Delta s(x_j, t_k)$  denote, respectively, the pressure distribution, the shear traction and the contact relative slip increment for the node  $j$  at the time increment  $t_k$ . Therefore, the total wear depth at  $N_t$  cycles for the node  $j$  is given by:

$$h_j = \sum_{i=1}^{n_w} \Delta h_{i,j} \quad (4.3)$$

Besides the update of the contact surface, which is addressed in the next section, changes in stress and strain are recorded for each wear step so that the Miner's linear cumulative damage rule (Palmgren, 1924; Miner, 1945) can be used to predict material failure. In this case, for a material sub-surface point  $\underline{x}$ , the total cumulative damage associated with the  $n^{th}$  wear step is given by:

$$D_{f,n}(\underline{x}) = \sum_{i=1}^n \frac{\Delta N}{N_{f,i}(\underline{x})} \quad (4.4)$$

where  $N_{f,i}$  is the fatigue life expected for a given stress state, i.e. after determining the stress state  $\underline{\sigma}(\underline{x}, t)$  for given material point  $\underline{x}$  and time instant  $t$  over the  $i^{th}$  fretting cycle, it can be introduced in multiaxial fatigue criteria in order to predict the fatigue life  $N_{f,i}(\underline{x})$  (see Subsection 2.5.5).

In this work, the centroid of elements were chosen in order to compute the damage parameter defined by Eq. (4.4). However, it is worth noting that, due to the material removal along the contact surfaces, the contact geometries are constantly modified which as consequence changes the position of the element centroids describing such geometries (mainly under gross sliding conditions). In order to account for that, the following numerical scheme was adopted: after each  $i^{th}$  fretting cycle simulation, the damage value on

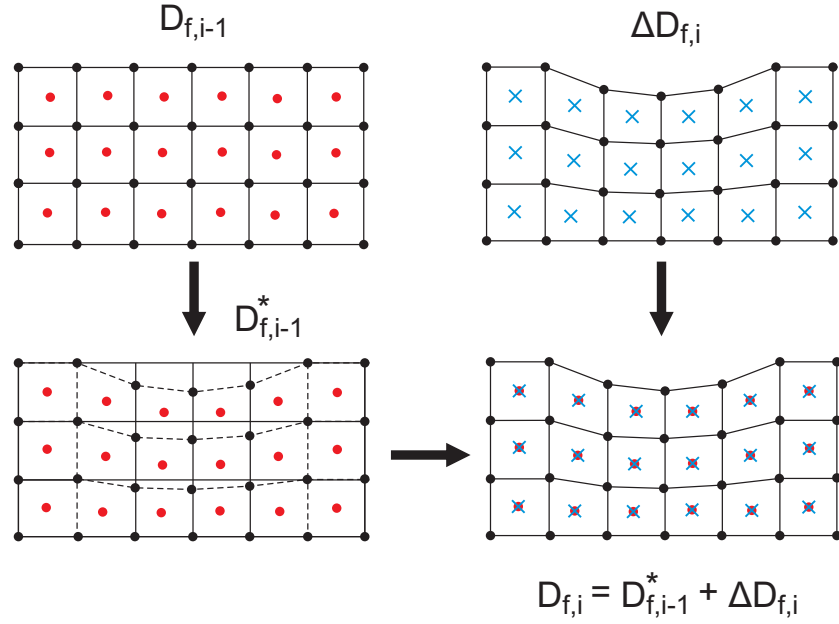


Figure 4.1: Illustration of the methodology used in order to transfer the cumulative damage from a previous fretting cycle simulation to the next.

the  $(i-1)^{th}$  fretting cycle was interpolated from the previous  $(i-1)^{th}$  element centroids to the new  $i^{th}$  element centroids location. Therefore, the actual damage field distribution at the  $i^{th}$  damage increment can be expressed as:

$$D_{f,i} = D_{f,i-1}^* + \Delta D_{f,i} \quad (4.5)$$

where  $D_{f,i-1}^*$  is the damage field from the previous fretting cycle simulation  $(i-1)^{th}$  interpolated to the position of the element centroid points at the  $i^{th}$  fretting cycle, Figure 4.1. As can be seen, this strategy ensures that damage is not accumulated at material points removed due to wear. Damage interpolation from a previous mesh configuration ( $D_{f,i-1}$ ) to the new one ( $D_{f,i-1}^*$ ) were performed by firstly applying a Delaunay triangulation to points at the  $(i-1)^{th}$  centroids location followed by a linear interpolation of  $D_{f,i-1}$  to the new element centroid positions.

### 4.3 Contact surface update

In order to update the contact surfaces as the fretting cycles goes on, two different strategies are commonly applied. One of them is the remeshing technique (McColl et al., 2004; Ding et al., 2004; Garcin et al., 2015), in this case, after the simulation of a fretting cycle, the coordinates of the contact nodes are vertically displaced by the amount defined in Eqs. (4.1)-(4.2) and another mesh is generated in order to avoid element distortion. Another way to tackle the problem is by using adaptive meshes (Madge et al., 2007a; Madge, 2009; Cruzado et al., 2013; Silva, 2016), where the position of the contact nodes are also displaced over the fretting cycles, however, this technique dispenses the remeshing procedure once that the mesh topology is held the same while nodal positions are shifted

in order to avoid distortion. However, an advection process needs to be carried out, which consists in remapping solution variables from an old mesh to the new one.

These two techniques were tested in this work. Figure 4.2 displays a flowchart illustrating the FE-based wear model coupled with the remeshing technique. Herein, a main Python script manages all the process which consists in the simulation of each fretting cycle  $i$  followed by the contact surfaces updating, where contact nodes are vertically moved according to Eq. (4.1) or (4.2) depending on the wear model used.

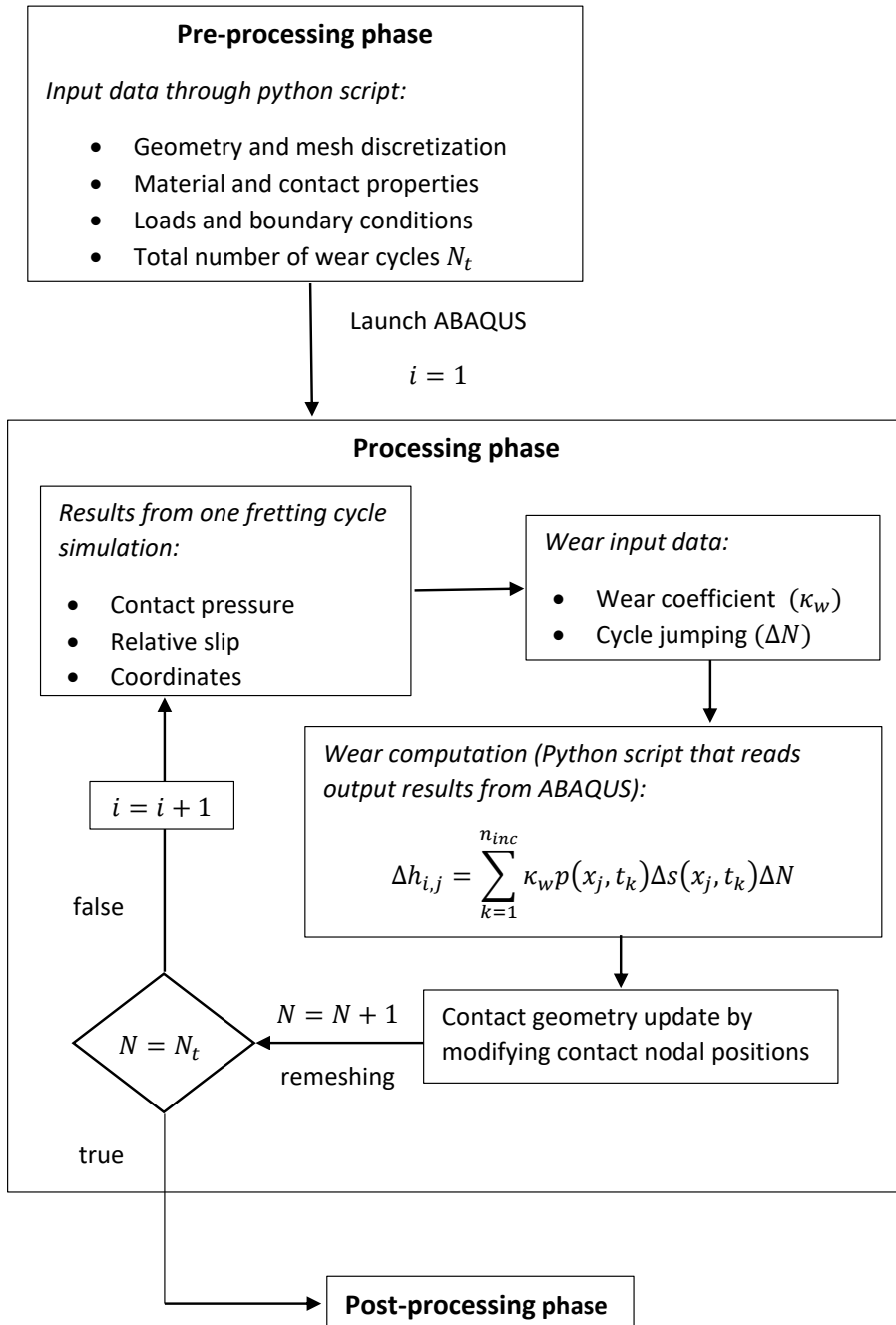


Figure 4.2: FE-based model for wear analysis using the remeshing technique.

Figure 4.3, on the other hand, depicts the incremental wear simulation methodology when using the adaptive meshing (ALE adaptive meshing (Abaqus, 2013)). In this case, the main difference is that instead of computing the material removal and updating the contact surface at the end of a complete fretting cycle, wear calculation and contact nodes motion are carried out within a fretting cycle for each load increment. This procedure is implemented by a user subroutine (UMESHMOTION, (Abaqus, 2013)).

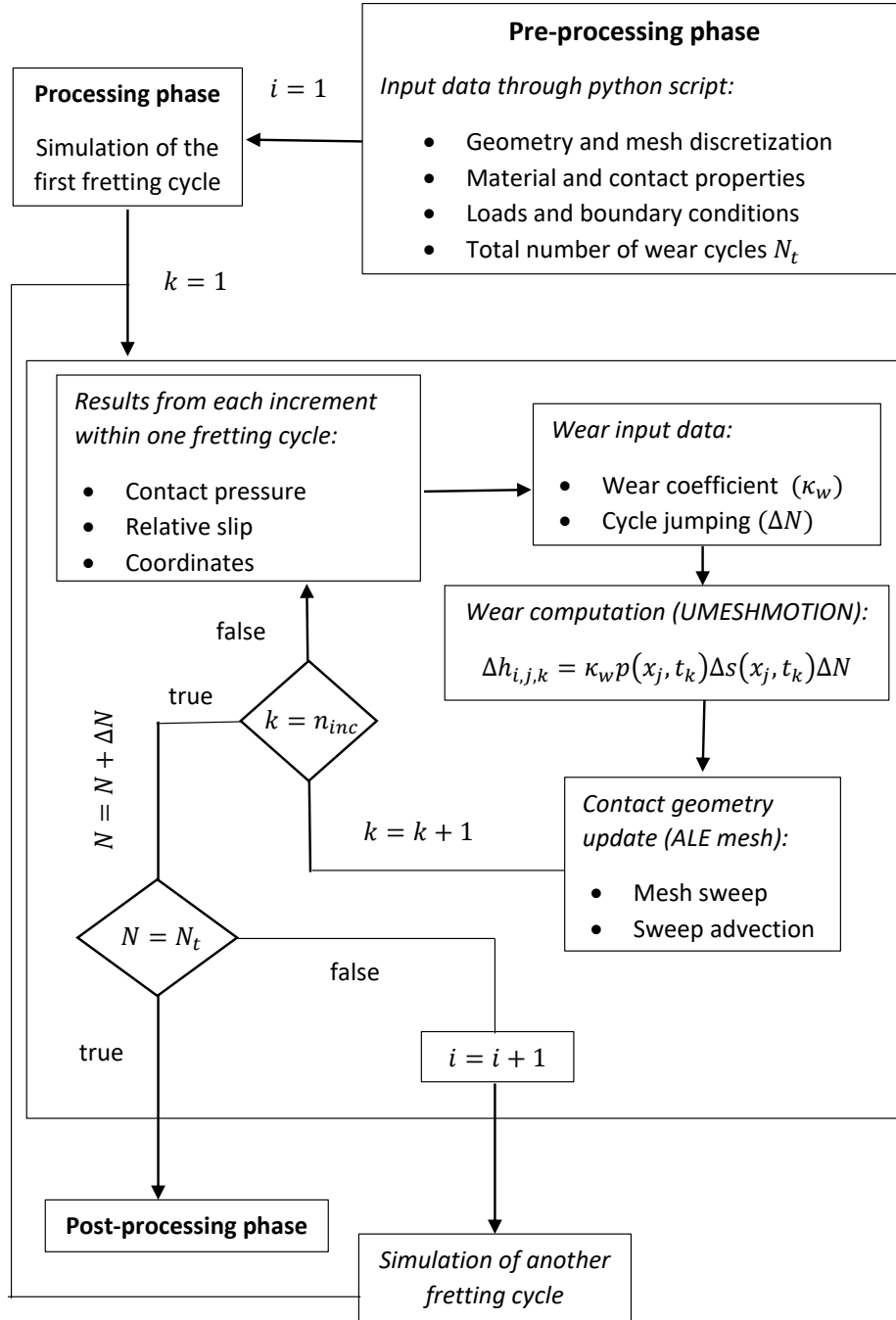


Figure 4.3: FE-based model for wear analysis using the ALE adaptive technique.

In order to evaluate these two methods, results from (Ding et al., 2004) were here reproduced and used as reference for validation. These authors have investigated the

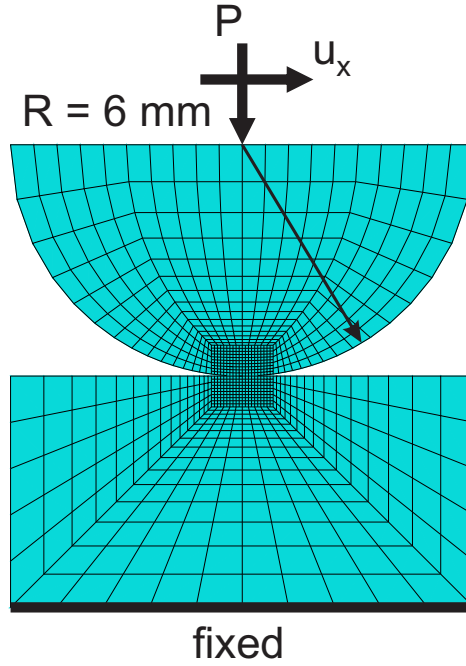


Figure 4.4: FE model used to validate wear implementations.

wear effects on the stress distribution under both partial and gross sliding conditions. Figure 4.4 depicts the geometry and load conditions considered, where first a normal load  $P = 120 \text{ N/mm}$  is applied to the cylindrical pad pressing it onto the flat specimen which is fixed on the bottom surface. Then, while this normal load  $P$  is held constant, a tangential oscillatory displacement  $u_x$  is applied to the pad. The upper surface of the pad is also subjected to a multi-point constraint which prevents pad's rotation. Two different amplitudes of  $u_x$  were investigated, a smaller one of  $2.5 \mu\text{m}$  establishing partial slip conditions and larger one of  $10 \mu\text{m}$  ensuring gross sliding regime.

The material considered was a high strength steel with Young modulus  $E = 200 \text{ MPa}$ , Poisson's ratio  $\nu = 0.3$  and a local wear coefficient  $k_w = 1.0 \times 10^{-7} \text{ MPa}^{-1}$  (Ding et al., 2004). The friction coefficient assumed in the simulations was  $\mu = 0.6$ .

Figure 4.5 shows the contact pressure distribution for different number of fretting cycles under partial slip conditions considering both contact surface update procedures (remeshing and adaptive meshing). In this case, the size of the mesh near the contacting surfaces was set equal to  $5 \mu\text{m}$ . As can be seen, as the wear evolves, slip zones are worn out while the stick zone tends to support all external contact loads. For a high enough number of cycles (18000 cycles, Figure 4.5(a)), it is possible to observe that the pressure distributions along the initial slip zones are nearly null, which happens because these zones were completely removed at this point. In this case, a full stick condition is observed at the initial stick zone region where the pressure distribution is close to the one found in complete contact problems (flat-on-flat). Similar conclusions were obtained previously by (Ciavarella and Hills, 1999) when evaluating wear effects under partial slip conditions analytically. This shifting of the hot spot zones from the contact edges towards the stick zones may explain why many times cracks are observed at the slip zones close the initial stick/slip zone region.

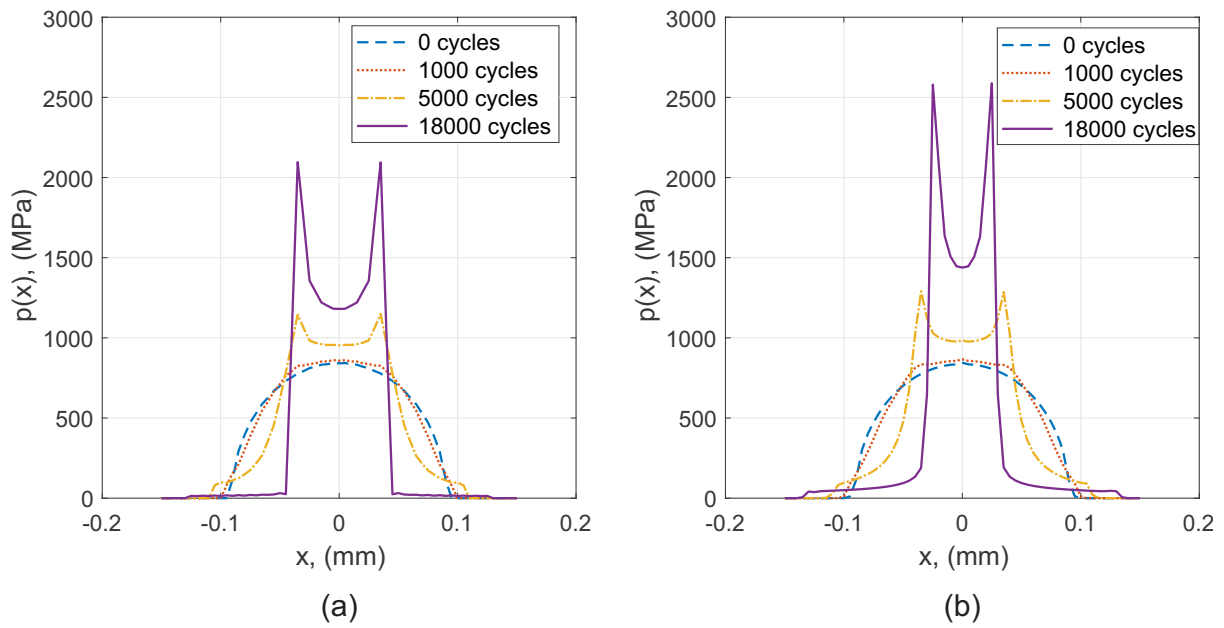


Figure 4.5: Contact pressure distributions under partial slip conditions ( $P = 120 \text{ N/mm}$ ,  $u_x = 2.5 \text{ }\mu\text{m}$ ,  $R = 6 \text{ mm}$ ) for different number of fretting cycles: (a) considering the remeshing technique and (b) the adaptive mesh.

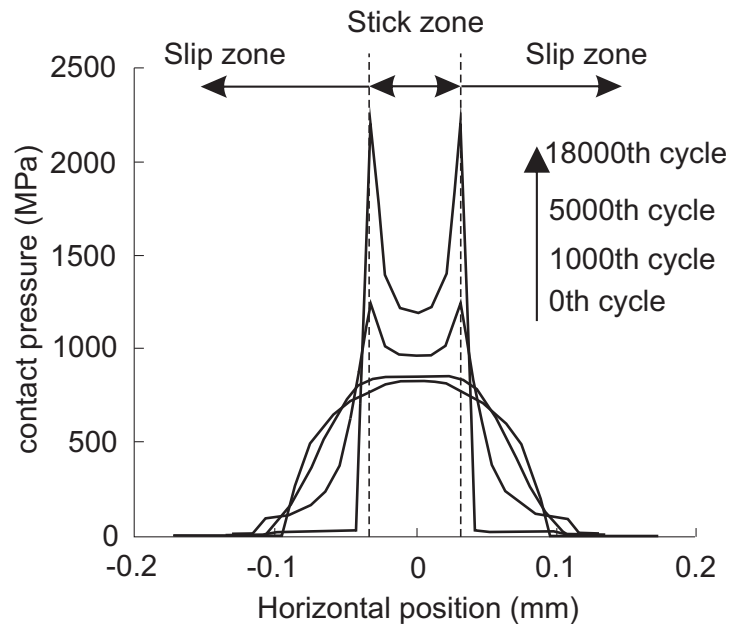


Figure 4.6: Contact pressure distributions under partial slip conditions for different number of fretting cycles (Ding et al., 2004).



Results from Figure 4.5(a) were obtained by using the remeshing technique and are in close agreement with the data provided by (Ding et al., 2004) (Figure 4.6), which used a similar contact surface updating procedure. On the other hand, the adaptive mesh strategy lead to overestimate wear effects. As can be seen in Figure 4.5(b), the size of the stick zone is always decreasing which consequently makes the peak pressure achieve very high values. Note as well that the pressure distribution at the initial slip zones falls to zero slower when compared to the remeshing technique. It may be due to the smoothing procedures performed on the ALE adaptive meshing algorithm (Abaqus, 2013). However, this phenomenon only took place when partial slip conditions were evaluated, i.e.  $u_x = 2.5 \mu\text{m}$ .

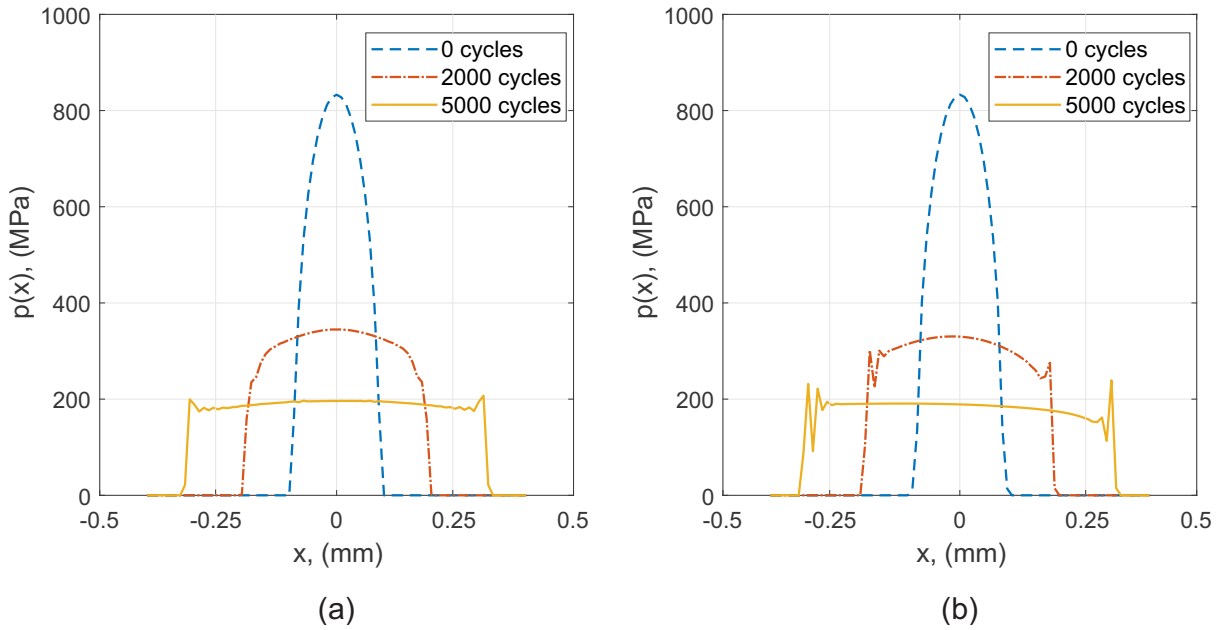


Figure 4.7: Contact pressure distributions under gross sliding conditions ( $P = 120 \text{ N/mm}$ ,  $u_x = 10 \mu\text{m}$ ,  $R = 6 \text{ mm}$ ) for different number of fretting cycles: (a) considering the remeshing technique and (b) the adaptive mesh.

When gross sliding conditions were assessed, both contact surface update procedures provided nearly the same results as depicted in Figure 4.7. In this case, the size of the mesh in the refined region surrounding the contact surfaces was defined equal to  $10 \mu\text{m}$ . For the gross sliding regime, it is possible to see that, as the fretting cycles evolve, the contact region becomes larger and the pressure distribution tends to a flat distribution. Note that the initial peak pressure is around 4 times higher than that at 5000 fretting cycles. In addition, the large amount of material loss is constantly removing severely damaged areas, which hinders the propagation of cracks. Results depicted in Figure 4.7 are in very good accordance with the ones presented by (Ding et al., 2004) (Figure 4.8). Results from Figures 4.5 and 4.7 were obtained before start applying the tangential displacement to the pad ( $u_x = 0$ ).

For the partial slip conditions, a jumping cycle ( $\Delta N$ ) of 2000 was used when using the adaptive meshing procedure. For the remeshing technique, the jumping cycle was set to 500. Fretting cycles were equally divided into 16 steps when using the remeshing

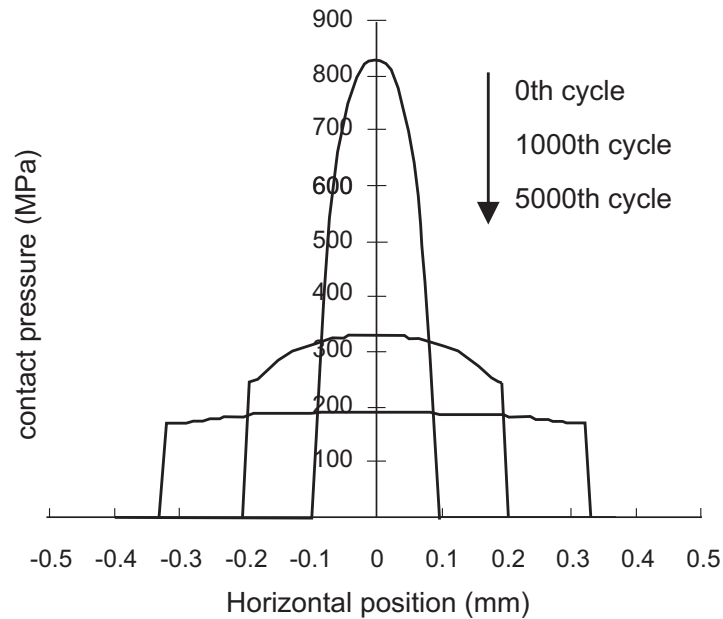


Figure 4.8: Contact pressure distributions under gross conditions sliding for different number of fretting cycles (Ding et al., 2004).

technique and 50 steps when using the adaptive meshing for the partial slip regime. For gross sliding conditions, the jumping cycle was set to 25 and 100, respectively, when using the remeshing and adaptive meshing procedures. In this case, for the fretting cycle increments, 16 time steps were used for the remeshing approach while 100 time steps for the adaptive meshing one.

Generally speaking, the ALE adaptive meshing is computationally more efficient and allows the use of higher cycle jumps. This procedure permits the modification of the contact surface incrementally throughout a tangential cycle. In addition, the unloading and loading phases of the normal load does not need to be carried out as it is done in the remeshing technique. However, this strategy is more memory demanding once that, all the fretting cycles incrementation data need to be stored in memory while the FE analysis is running, which can be a huge drawback when considering large problems. Besides, the apparently no stabilization of the worn profile under partial slip conditions is a considerable shortcoming in the scope of this work, once that, high cycle fretting fatigue cases will be evaluated. Therefore, the remeshing technique was chosen in order to update contact surfaces when performing fretting simulations in this work. Figures 4.9 and 4.10 show the worn profile of the flat specimen and the cylindrical pad by using the remeshing technique for both slip regimes.

It is worth noting that, in spite of the slip regime, Madge et al. (2007a) obtained good results by estimating the effect of slip amplitude on fretting fatigue life by using the adaptive meshing technique. In this case, good results under partial slip conditions may be explained due to the fact that, for the data by them assessed, contact loads and wear coefficient were smaller, which consequently decreases wear rates. And as can be seen in Figure 4.9, for the first 5000 cycles, results obtained by using the remeshing or the adaptive meshing technique do not diverge too much. In other words, for a certain level of wear, under partial partial slip conditions, both procedures provide similar results.

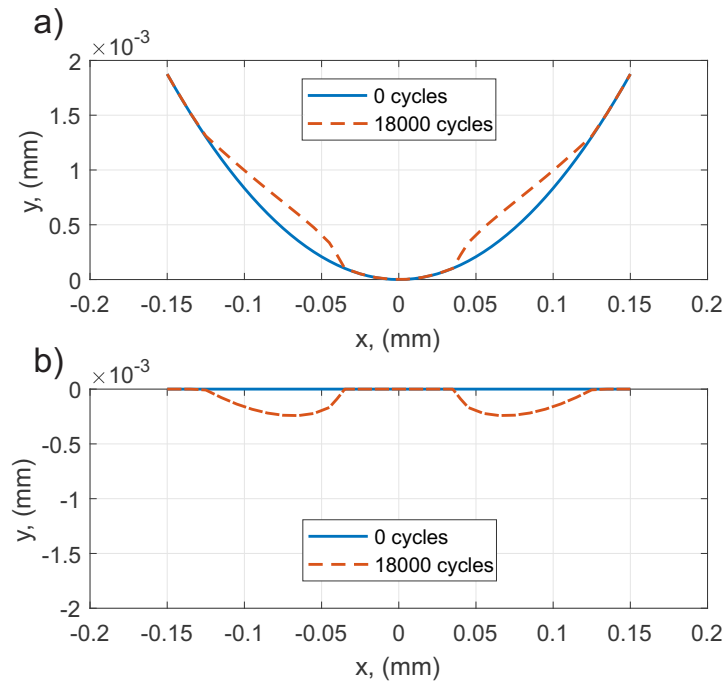


Figure 4.9: Worn profile under partial slip conditions ( $P = 120$  N/mm,  $u_x = 2.5$   $\mu$ m,  $R = 6$  mm): (a) pad, (b) specimen.

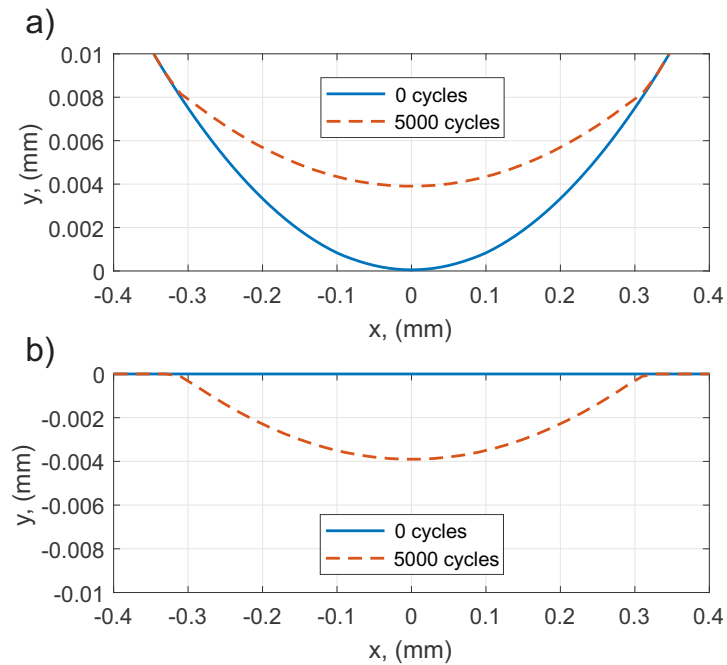


Figure 4.10: Worn profile under gross sliding conditions ( $P = 120$  N/mm,  $u_x = 10$   $\mu$ m,  $R = 6$  mm): (a) pad, (b) specimen.

## 4.4 Experimental data available

Aiming to investigate the influence of wear under fretting fatigue conditions (partial slip), the experimental data provided by (Ferry, 2017) is assessed and used as reference for comparison with the numerical results. In her work, besides evaluating the applicability of the nonlocal intensity factors presented in Section 3.1 when those are used to define crack initiation frontiers under fretting conditions, the size effect in fretting fatigue problems was also investigated. In this case, two types of experimental campaigns were evaluated. In one of them (Group-2a of tests) <sup>1</sup>, the aim was to investigate the effect of the volume of material being stressed under the contact. In this group-2a tests, the stress gradient inward the contact and the area of the slip zones were the same for all the experiments. In the other set of experiments (Group-2b of tests), the goal was to verify the influence of damaged area on the tests while the stress gradient was kept the same. The contact geometry considered was the cylinder on plane one. For more details concerning pads and specimens manufacturing and specifications, see (Ferry, 2017).

The stress gradient inward the contact moving away from the trailing edge was evaluated via MWCM (Subsection 2.5.5.3), where it can be expressed as:

$$I_{MWCM} = \tau_a + \left( \frac{\sigma_{-1} - \sigma_0}{2} \right) \frac{\sigma_{n,amax}}{\tau_a} \quad (4.6)$$

Table 4.1: Group-2 fretting fatigue data for the Ti-6Al-4V (Ferry, 2017) (pad radius  $R = 70$  mm).

test	thickness (mm)	$\sigma_{b,max}/p_0$	$Q_{max}/\mu P$	$A_{th}^s$ (mm <sup>2</sup> )	$N_f^{exp}$
T1	8	0.45	0.68	7.43	218000
T2	13	0.6	0.46	7.37	167000
T3	8	0.3	0.65	7.01	672000
T4	13	0.46	0.44	6.99	443000
T5	8	0.6	0.46	4.53	207000
T6	8	0.40	0.42	4.08	529000
T7	13	0.40	0.42	6.62	538000

The data provided by (Ferry, 2017) is presented in Table 4.1, where  $\sigma_{b,max}$  is the maximum value reached by the bulk stress during a fretting cycle while  $Q_{max}$  is the maximum tangential load.  $A_{th}^s$  is the theoretical area of the slip zones and  $N_f^{exp}$  is the experimental number of cycles to failure. A pad radius  $R = 70$  mm was considered in the analysis. A peak pressure  $p_0 = 500$  MPa was kept in all tests. The numerical model and load sequence considered in the experiments are depicted in Figure 4.12, where more details will be given in the next section. Tests from 1 to 4 aimed to investigate the effect of the volume of material being stressed. For example, tests T1 and T2 were designed

<sup>1</sup>The nomenclature Group-2a is here used in order to be in accordance with the one utilized in (Ferry, 2017), where, in her work, Group-1 tests were intended to verify the accuracy of the nonlocal intensity factors (Section 3.1) in estimating fretting crack initiation frontiers.

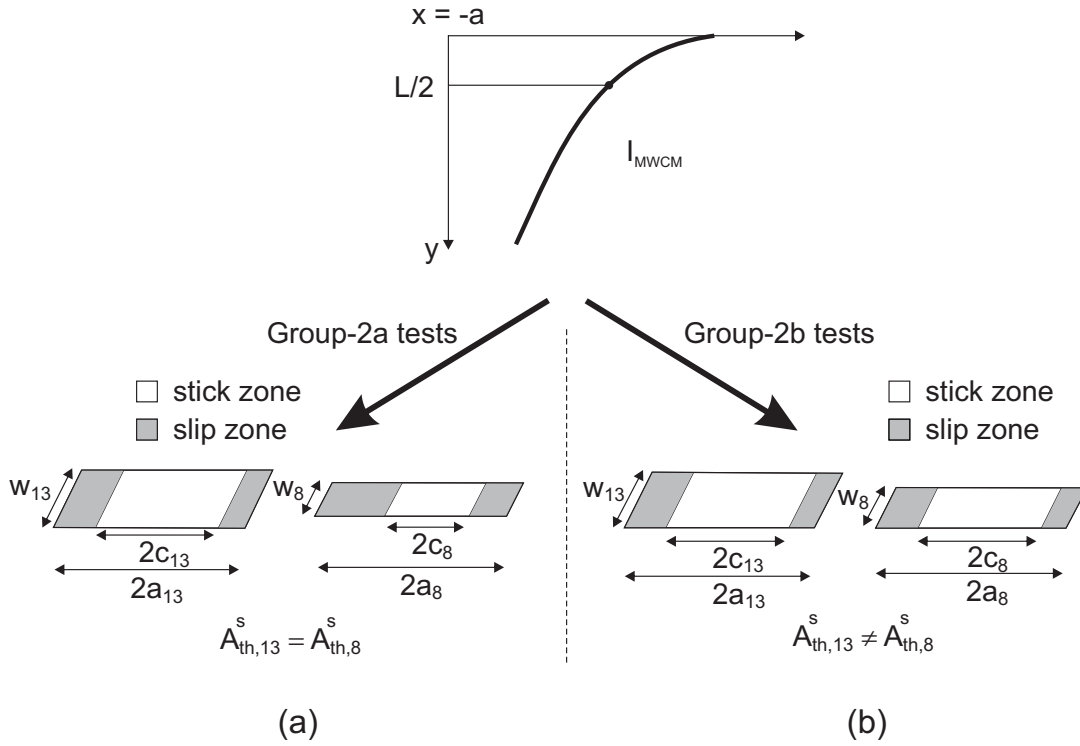


Figure 4.11: Schematic representation of the Group-2 tests: (a) Group-2a tests with the same slip zone areas for different contact widths, (b) Group-2b tests with different slip zone areas.

to have the same slip areas (Figure 4.11(a)) and the same stress gradient at the contact trailing edge ( $x = -a$ ), however with different volumes of material being stressed. This can be done by changing the specimens and pads thickness, i.e. from 8 to 13 mm. In order to keep the same slip areas between these two tests, the tangential load needs to be modified, once that it changes the length of the slip areas. Doing so, the bulk load also needs to be adequately changed in order to hold the same stress gradient for the two tests (T1 and T2). Same is required for tests T3 and T4, however in this case, loads are lower so that higher lives could be achieved during experiments.

On the other hand, tests T2, T5-T7 were intended to investigate the influence of the damaged area due to wear on fretting fatigue, Figure 4.11(b). In this setting, tests T2 and T5 have the same stress gradient nearby the contact edges, however, the size of the slip areas are different within these two tests. The same is valid for tests T6 and T7 but with a less severe stress gradient.

All these experiments were conducted in the facilities of the Fatigue, Fracture and Materials Research Group at the University of Brasilia. The experimental apparatus is presented in Figure 2.5 (Section 2.3). The material of the pads and specimens was the titanium alloy Ti-6Al-4V. Its basic properties are given in Table 4.2. The friction coefficient,  $\mu$ , is 0.5 (Bellecave et al., 2014).

Table 4.2: Mechanical properties of the Ti-6Al-4V alloy (Le Biavant-Guerrier, 2000).

Material	$E$ (GPa)	$\nu$	$\sigma_y$ (MPa)	$\sigma_{ut}$ (MPa)	$HV$
Ti-6Al-4V	119.4	0.286	850	1000	360

## 4.5 Finite element modelling of wear

To carry out the fretting fatigue simulations, the commercial FE software ABAQUS 6.14 was used (Abaqus, 2013). It allowed a faster and simpler implementation of the contact evolution approach assessed in this work. The FE model adopted in this work is illustrated in Figure 4.12. As depicted, a static normal load,  $P$ , presses a cylindrical pad of radius  $R$  against a flat specimen which is already subjected to a static mean bulk load. After that, a tangential load  $Q$  is applied to the pad in phase with an alternate bulk load. Note that the mean and the alternate bulk loads give rise to the mean ( $\sigma_m$ ) and alternate ( $\sigma_a$ ) bulk stresses, respectively. A central refined zone composed of linear quadrilateral elements is defined in a rectangular region surrounding the contact surfaces. The size of the elements in this area is around  $15 \mu\text{m}$ . Outside this region, a coarser mesh is formed by linear triangular elements. Plain strain elements are considered in the analysis. Concerning the contact aspects, the nodes on the refined region of the pad are defined as the slave ones while the master nodes are set on the specimen. The frictional contact constraints are imposed via the Lagrange multiplier approach (Subsection 3.3.2). The penalty method was not used here once that, in order to perform wear computations, exact slip solutions are needed inside the stick zones (the Penalty method allows some slip to take place even under stick conditions). Multi-point constraints are enforced on the upper surface of the pad so that rotation is prevented.

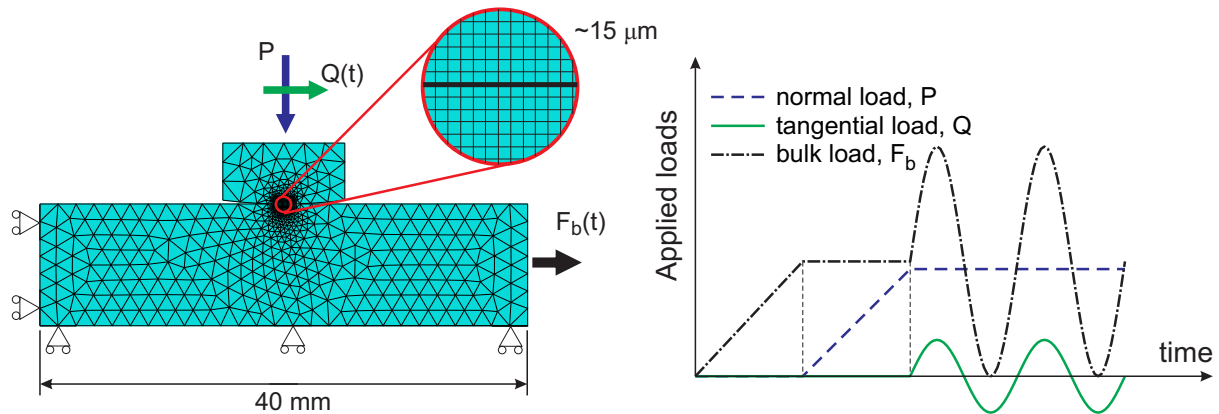


Figure 4.12: Finite element model used in order to carry out fretting fatigue/wear simulations.

To validate the FE model, a fretting fatigue problem neglecting wear effects was simulated and results were compared to the analytical solution of the problem (Section 2.7). Figure 4.13 depicts the normal and shear traction distributions along the contact when both the tangential and the bulk loads achieve their maximum value (load case test T2).

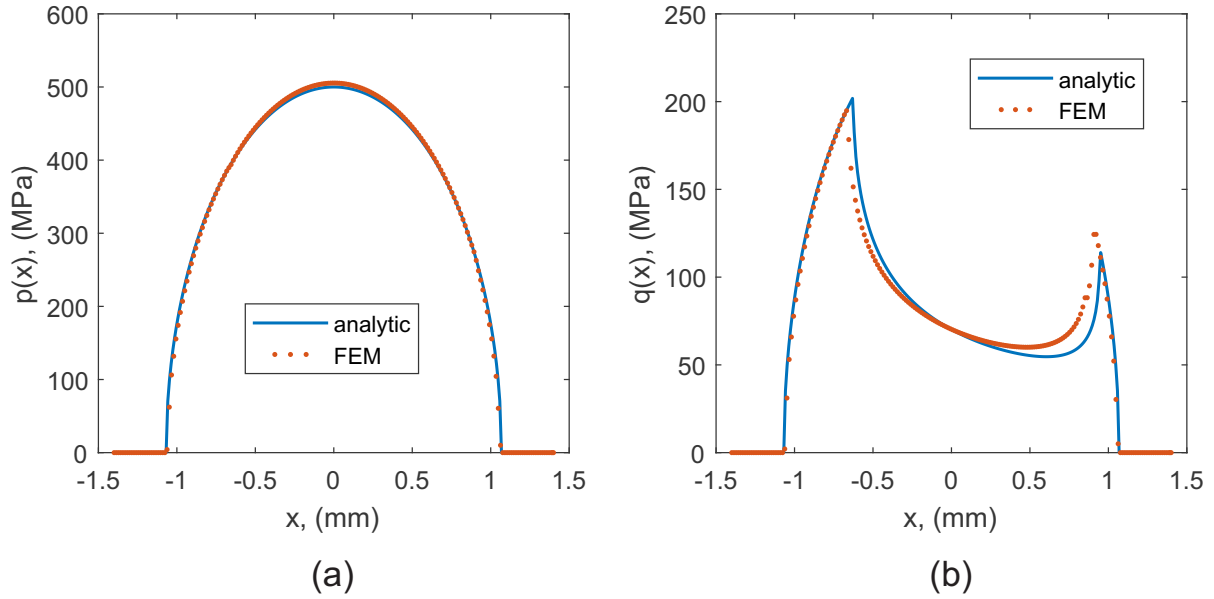


Figure 4.13: Comparison between analytical and FE solution: (a) pressure and (b) shear traction distribution (loading conditions from test T2 in Table 4.1).

As can be seen, a good agreement can be found between the FE predictions and analytical solution of the problem.

## 4.6 Multiaxial fatigue life assessment

The objective of this chapter is to investigate the effects of wear when estimating fatigue life under fretting conditions. The material investigated here is the Ti-6Al-4V. To calibrate the fatigue models presented in Subsection 2.5.5, the uniaxial fatigue data provided by (Kallmeyer et al., 2002) was used, see Figure 4.14. In this case, S-N curves for the Ti-6Al-4V were obtained considering uniaxial tests for different load ratios  $R_\sigma$ .

For instance, when considering the Smith, Watson and Topper (SWT) fatigue model, the fatigue data presented in Figure 4.14 can be expressed by means of its parameter, Eq. (2.11), as a function of the number of cycles to failure, Figure 4.15. Then, a two parameter power law can be used to fit the experimental data yielding:

$$I_{SWT} = 4.35N_f^{-0.093} + 2.45 \times 10^4 N_f^{-0.94} \quad (4.7)$$

Figure 4.16 illustrates the same procedure previously described, however using Findley's multiaxial fatigue parameter, which produces:

$$I_{FP} = 1.02 \times 10^5 N_f^{-0.64} + 363 N_f^{-0.031} \quad (4.8)$$

Note that the computation of  $I_{FP}$  demands the knowledge of the material parameter  $\gamma$  (see Eq. (2.10)), which for metals, in general, ranges between 0.2 and 0.3. The value of 0.3 was assumed in this work.

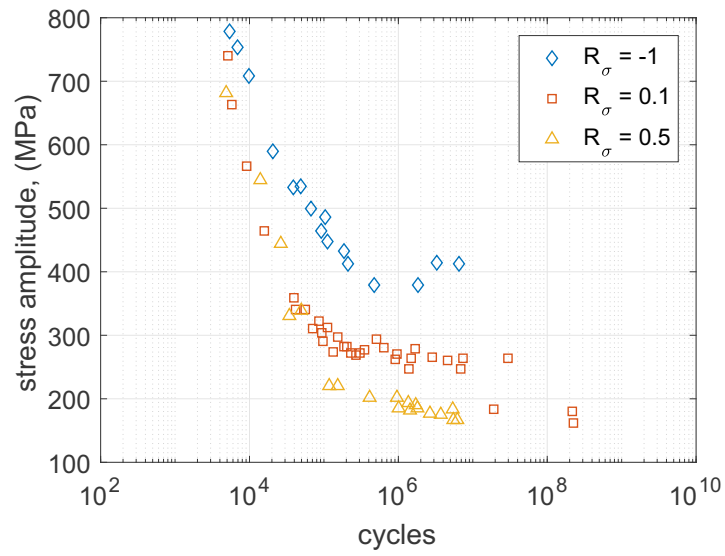


Figure 4.14: Uniaxial fatigue data for the Ti-6Al-4V (Kallmeyer et al., 2002).

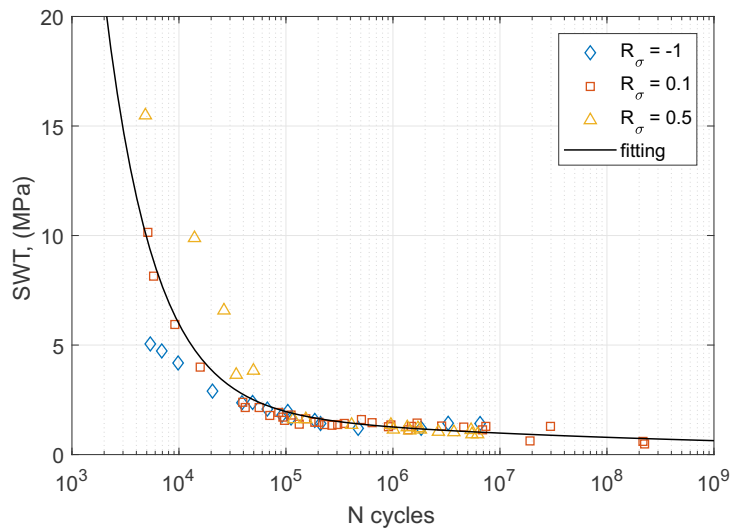


Figure 4.15: Uniaxial fatigue data for the Ti-6Al-4V (Kallmeyer et al., 2002) expressed in terms of the SWT parameter.



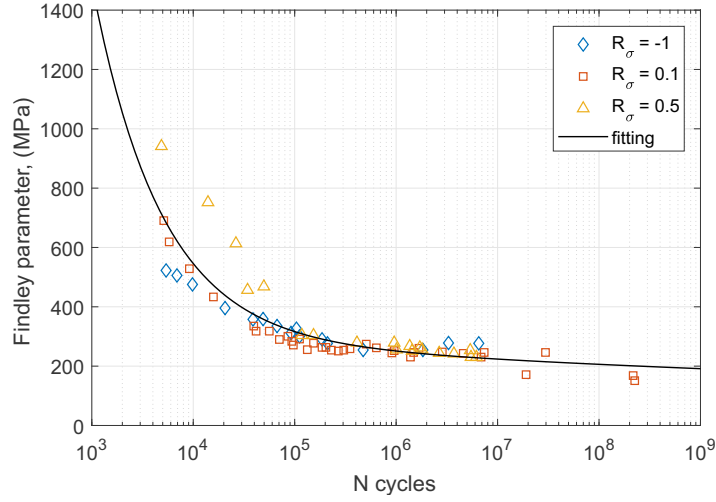


Figure 4.16: Uniaxial fatigue data for the Ti-6Al-4V (Kallmeyer et al., 2002) expressed in terms of the Findley parameter.

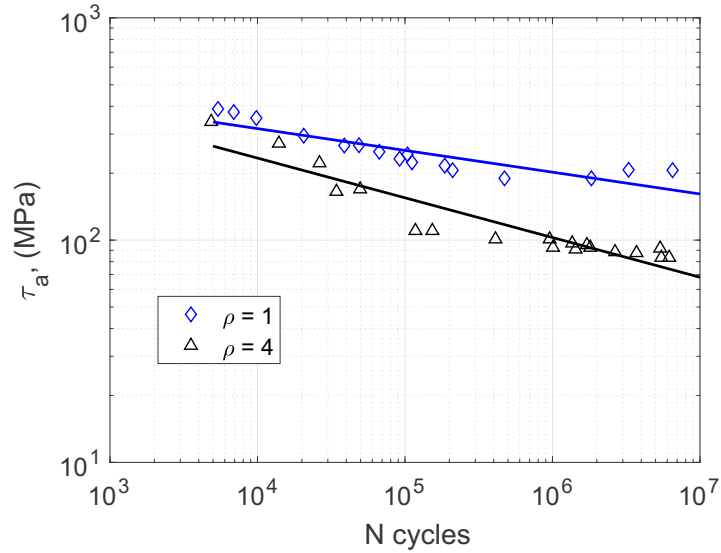


Figure 4.17: Uniaxial fatigue data for the Ti-6Al-4V (Kallmeyer et al., 2002) expressed in terms of the MWCM.

Finally, considering the Modified Wöhler Curve Method (MWCM), the following expressions were found:

$$N_f = 5 \times 10^6 \left[ \frac{\tau_{a,ref}(\rho)}{\tau_a} \right]^{\kappa_\tau(\rho)} \quad (4.9)$$

where

$$\tau_{a,ref}(\rho) = -32\rho + 205 \quad (4.10)$$

and

$$\kappa_\tau(\rho) = -0.0269\rho - 0.0711 \quad (4.11)$$

In order to obtain Eqs. (4.10) and (4.11) the interpolation strategy shown in Subsection 2.5.5.3 was applied to the uniaxial fatigue data corresponding to the load ratios  $-1$  ( $\rho = 1$ ) and  $0.5$  ( $\rho = 4$ ). Figure 4.17 depicts the two reference modified Wöhler curves investigated. In order to compute  $\tau_a$  used in the Findley and MWCM multiaxial fatigue criteria, the MRH has been used (see Appendix D). Note that these three multiaxial fatigue models considered presented a considerable dispersion for low cycle fatigue data. However, for high cycle fatigue, the regime assessed in this work, correlation with uniaxial data is quite fair.

Again, as this chapter aims to check if it is really worthwhile considering wear effects under partial slip conditions, three different models are used in an attempt to minimize the influence of the multiaxial fatigue criteria considered in the present investigation.

## 4.7 Results

Aiming to investigate the effects of wear under fretting fatigue conditions, two types of simulations were performed in this work. Firstly, wear effects were neglected in order to estimate fatigue life. In sequence, wear effects were considered following the procedures described in the previous sections. The friction dissipated energy equation (Eq. (4.2)) was considered in the analysis due to experimental availability of the energy wear coefficient  $\alpha$  for the Ti-6Al-4V, which was obtained from (Garcin et al., 2015), ( $\alpha = 1.43 \times 10^{-8}$  MPa $^{-1}$ ).

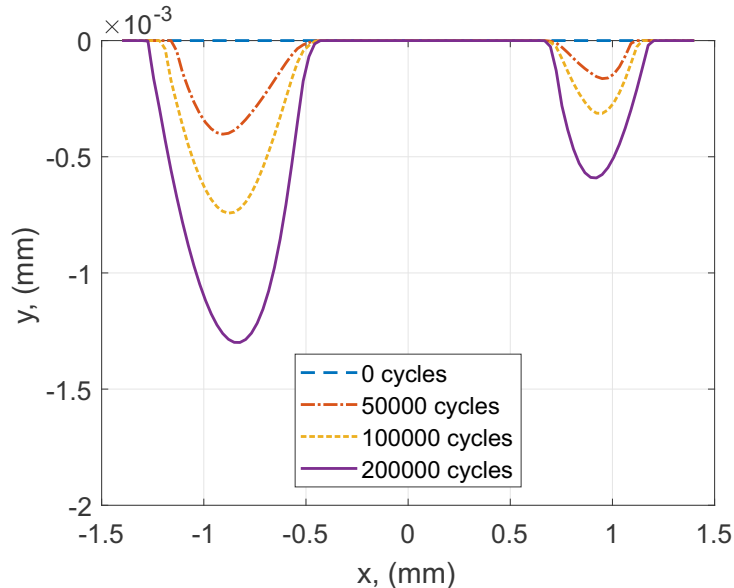


Figure 4.18: Specimen's worn profile for different number of fretting fatigue cycles considering loading conditions from test T1.

Figure 4.18 depicts the worn surface of the specimen for different number of cycles when the load conditions given by the test T1 are considered. Contact pressure distribution for different number of cycles are shown in Figure 4.19(a). On the other hand, Figure 4.19(b) depicts the shear traction distribution over the cycles. Pressure profiles are taken

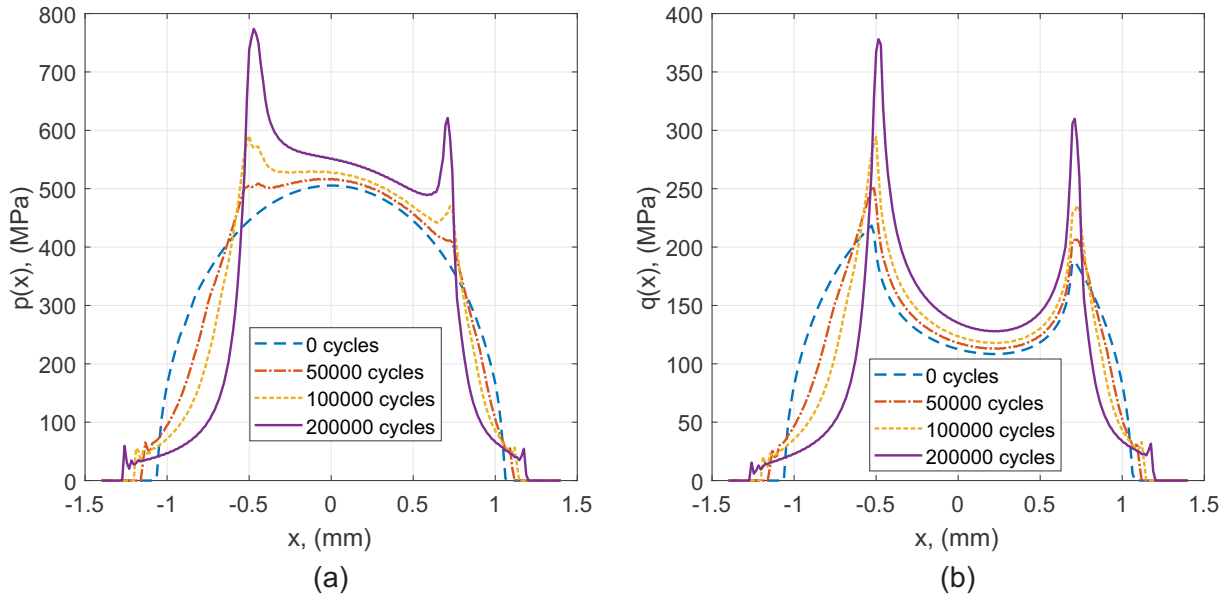


Figure 4.19: Contact traction distribution for different number of fretting fatigue cycles considering loading conditions from test T1: (a) pressure ( $Q(t) = 0$ ) and (b) shear traction ( $Q(t) = Q_{max}$ ).

before applying the tangential load, i.e.  $Q(t) = 0$ , whereas shear tractions are obtained when  $Q(t) = Q_{max}$ . As can be seen, the presence of the bulk load  $F_b$ , besides provoking an offset of the stick zone, makes the material removal more prominent on the left slip zone. As fretting cycles goes on, pressure distributions on the initial slip zones are reduced while stress distributions at the initial stick zones are increased in order to keep the force equilibrium. Peaks in the transitions between stick and slip zones are also observed. A similar trend is observed when loading conditions from the other tests (Table 4.1) are assessed.

Fatigue life was estimated by using each one of the three different multiaxial fatigue criteria given by Eqs. (4.7)-(4.9). Note that when wear is included in the analysis, the damage cumulation law presented in Section 4.2 is needed once that, due to the material removal and geometry modification, stress distributions are constantly changing. Since hot spot approaches are not well suited for contact problems (Araujo and Nowell, 2002; Araújo et al., 2007; Taylor, 2011), a nonlocal procedure based on the Theory of Critical Distances (point method) have been used in this work (see Section 2.6 for more details). A critical distance parameter  $L = 30 \mu\text{m}$  was adopted in this work (Bellevue et al., 2014).

When neglecting wear effects, stresses/strains can be readily obtained considering a point  $L/2$  vertically distant from the contact trailing edge and life can be estimated through multiaxial fatigue criteria, Figure 4.20. However, when wear takes place, the hot spot point at the contact surface is continually changing. In this case, in order to estimate fatigue life, the procedure adopted here is to compute the damage parameter defined by Eq. (4.4) and check when it achieves the value of 1 (failure). However, failure is only considered when this point is at least  $L/2$  distant from the contact surface, Figure 4.21. This procedure was conducted in order to incorporate the stress gradient in the life estimation procedure. If stresses were considered too close from the contact surface, life

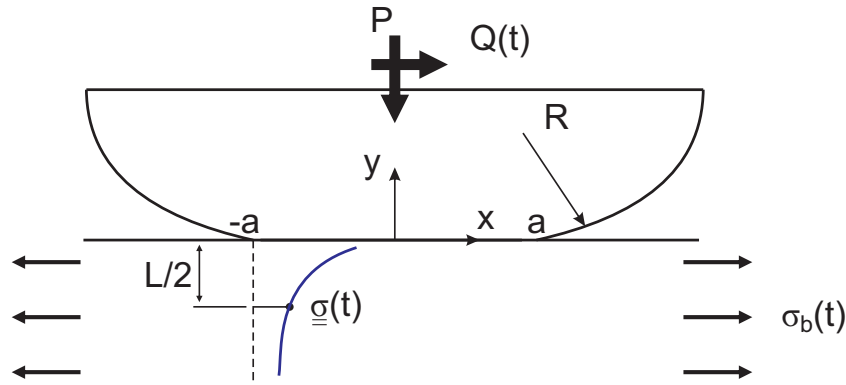


Figure 4.20: TCD applied to fretting problems when wear effects are neglected.

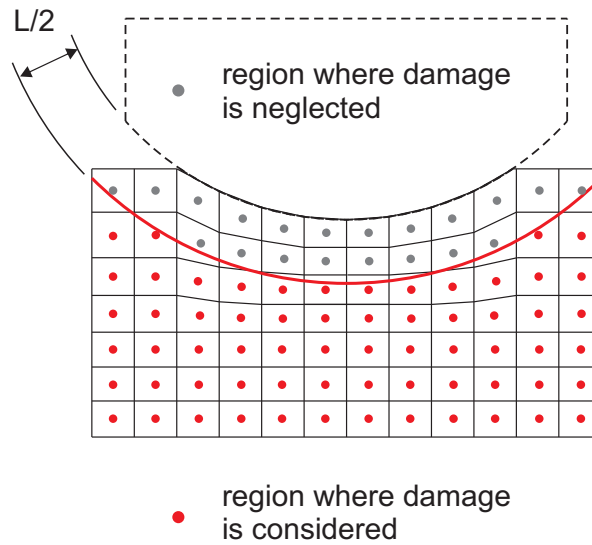


Figure 4.21: TCD applied to fretting problems when wear is taken into account.

estimates would be systematically underestimated.

Table 4.3 summarizes the life estimate for the experimental data presented in Table 4.1 when wear effects are taken into account. Life results are provided considering each one of the multiaxial fatigue criteria presented in Section 4.6, i.e. SWT ( $N_f^{SWT}$ ), Findley ( $N_f^{FP}$ ) and MWCM ( $N_f^{MWC}$ ). The same is valid for Table 4.4 but neglecting wear effects, i.e. contact geometry is assumed to be the same all over the fretting cycles.

Note that tests conducted at the same loading levels but with different specimen thickness presented the same life estimates (T2/T5 and T6/T7). This is due to the fact that one carries out numerical simulations by assuming 2D plain strain elements. Besides, as can be seen in the experimental results and as pointed out by (Ferry, 2017), the specimen thickness does not have a great influence in terms of life when the same levels of loads are considered. In other words, components subjected to the same stress gradients nearby the contact edges will experience similar lives despite the size of the slip areas.

Regarding the dispersion when evaluating fatigue lives, at a first glance, both predictions considering and neglecting wear effects seem reasonably accurate, Figure 4.22. Only

Table 4.3: Life estimates considering wear effects.

Results considering wear							
test	thickness (mm)	$\sigma_{b,max}/p_0$	$Q_{max}/\mu P$	$N_f^{exp}$	$N_f^{SWT}$	$N_f^{FP}$	$N_f^{MWCM}$
T1	8	0.45	0.68	218000	271000	155000	132000
T2	13	0.6	0.46	167000	304000	174000	208000
T3	8	0.3	0.65	672000	405000	251000	192000
T4	13	0.46	0.44	443000	573000	328000	343000
T5	8	0.6	0.46	207000	304000	174000	208000
T6	8	0.40	0.42	529000	821000	447000	475000
T7	13	0.40	0.42	538000	821000	447000	475000

Table 4.4: Life estimates neglecting wear effects.

Results neglecting wear							
test	thickness (mm)	$\sigma_{b,max}/p_0$	$Q_{max}/\mu P$	$N_f^{exp}$	$N_f^{SWT}$	$N_f^{FP}$	$N_f^{MWCM}$
T1	8	0.45	0.68	218000	106000	75000	152000
T2	13	0.6	0.46	167000	122000	87000	237000
T3	8	0.3	0.65	672000	387000	187000	512000
T4	13	0.46	0.44	443000	452000	224000	733000
T5	8	0.6	0.46	207000	122000	87000	237000
T6	8	0.40	0.42	529000	1363000	465000	1441000
T7	13	0.40	0.42	538000	1363000	465000	1441000

a few cases lie outside the region defined by the factor of 2 lines. Besides, these cases are apparently more related to the multiaxial fatigue criterion used itself. In addition, Table 4.5 expresses the life estimate errors for each multiaxial fatigue criteria assessed in this work. In this setting, for the data here studied, when considering wear effects, the SWT model provided the least conservative results although all estimates had errors smaller 100 %. Findley and MWCM criteria lead to similar estimates, however with results a little more centred than the SWT ones and with a more conservative trend. On the other hand, when neglecting wear effects, estimates are in general more scattered than when considering wear. Additionally, except for tests T6 and consequently T7, where SWT and MWCM considerably overestimated the results, all other predictions got errors smaller than 100 %. Therefore, in spite of the results obtained considering wear effects are slightly better, neglecting wear does not seem to strongly affect multiaxial fatigue damage assessment still providing reasonable life predictions under partial slip conditions. Neglecting wear also simplifies the problem and significantly reduces its computational cost, which would be a key point if complex 3D components were being evaluated.

However, it is worth noting that, when considering wear effects, the fatigue damage tends to spread over a larger region and failure is predicted to happen inside the slip zone. For the load configuration T1, for example, failure is predicted close to the transition between the stick and the slip zone, Figure 4.23(a). On the other hand, when neglecting wear effects, failure is always predicted to take place near the contact trailing edge despite

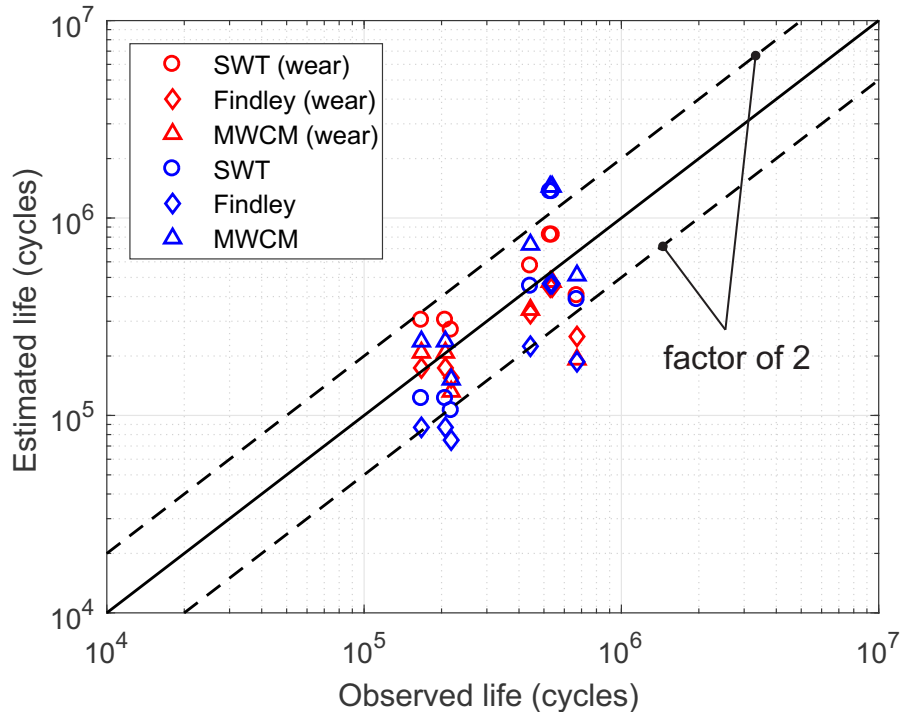


Figure 4.22: Estimated and observed fretting fatigue lives reported in (Ferry, 2017).

Table 4.5: Estimated errors considering (a) and neglecting wear effects (b).

test	SWT	Findley	MWCM
<b>(a) Errors (%) considering wear:</b>			
T1	24	-29	-39
T2	82	4	25
T3	-40	-63	-71
T4	29	-26	-23
T5	47	-16	0
T6	55	-16	-10
T7	53	-17	-12
<b>(b) Errors (%) neglecting wear:</b>			
T1	-51	-66	-30
T2	-27	-48	42
T3	-42	-72	-24
T4	2	-49	65
T5	-41	-58	14
T6	158	-12	172
T7	153	-14	168
*Errors (%) are defined as the difference between the estimated lives and the experimental ones divided by the experimental observations.			

the load configuration assessed, Figure 4.23(b).

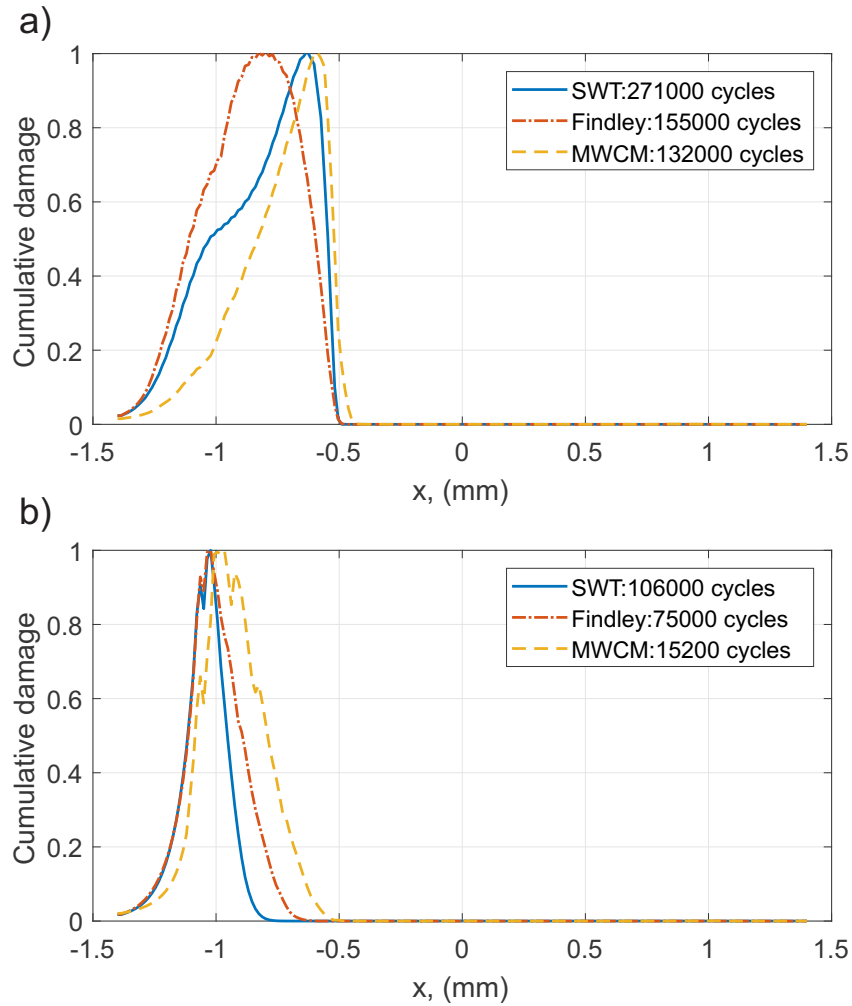


Figure 4.23: Damage distribution inward the contact at  $L/2$  for the load configuration T1: (a) considering and (b) neglecting wear effects.

The author is aware that wear simulations carried out in this work did not take into account third body effects (Ding et al., 2007; Basseville et al., 2011) and variations of the friction coefficient (Yue and Wahab, 2017). Another important point is that, when performing wear simulations under partial slip conditions, cracks would have appeared at some point, and this would be responsible for modifying the contact stress distributions even more. However, in the view of the dispersion involved in fatigue, simplifications assumed in this work seem to be reasonable. It is also worth noting that, the material here considered was an aeronautical Ti-6Al-4V alloy, which has some interesting properties, for instance, high mechanical properties such as its hardness, corrosion resistance and fine surface finishing, which all along contributed to low wear rates (Waterhouse, 1992). In this setting, further investigations should also be employed to materials more susceptible to wear.

## 4.8 Chapter highlights

In this chapter, the influence of considering wear on the simulation of fretting fatigue problems under partial slip conditions was investigated. For so, life estimates taking into account and neglecting wear were both carried out. Results were compared to experimental data for a Ti-6Al-4V titanium alloy (Ferry, 2017). To estimate fatigue life, three different multiaxial fatigue criteria were assessed (SWT, Findley and MWCM). In addition, in order to account for the stress gradient effect inherent to contact problems, the Theory of Critical Distances (TCD) has been considered. Wear was computed on a nodal basis by using the dissipated friction energy criterion (Fouvry et al., 2003). The updating of the contacting surfaces through the fretting cycles was achieved by using a remeshing technique, once that it has proven to be more reliable than the adaptive meshing (UMESHMOTION) in the framework of this work.

Results have shown that, considering wear effects slightly improve the quality of the results where these are less scattered than the ones obtained neglecting wear. However, wear modelling is computationally speaking much more expensive, once that, many fretting cycles need to be simulated during the analysis. When considering wear, the SWT multiaxial fatigue criterion provided less conservative results than the shear stress based models, i.e. Findley and MWCM. When wear is neglected, MWCM and SWT overestimated the fatigue life in one more than 150% for one of the loading conditions assessed. In addition, when wear is regarded, failure is predicted inside the slip zone towards the location of the initial transition between stick and slip zones. Nevertheless, neglecting wear systematically indicates failure at the contact trailing edge.



# Chapter 5

## Conclusion and perspectives

### 5.1 Main conclusions

In this work, which was divided in two parts, firstly, an enrichment-based (X-FEM) approach was used in order to capture the strong stress gradient close to the contact surfaces in fretting simulations performed on coarse meshes. The results were compared with reference solutions obtained using refined standard FE simulations. The modes used to enrich the simulations were obtained through a crack analogy approach (Montebello et al., 2016; Giannakopoulos et al., 1998, 2000). The results have shown that, by using the enrichment technique, the computational cost of such simulations can be considerably reduced, once that, without losing accuracy, one can work with meshes up to 10 times coarser than those considered in the standard FEM. The methodology also proved itself effective when gross slip is taken into account.

The nonlocal intensity factors presented in Section 3.1 proved to be good indicators of the contact status, suggesting that they may be used to obtain precise information about local contact parameters, as the position of the contact edges, allowing a more precise application of the enrichment technique for moving contact surfaces. In this context, only an initial guess about the position of the contact edge needs to be known. The main challenge for further studies in this setting consists in testing the enrichment technique presented in this work in a 3D framework, which will be certainly the case for future cooperation with SAFRAN. Besides, studies are still in progress in an attempt to link local contact quantities with the nonlocal intensity factors  $I^s$ ,  $I^a$  and  $I^c$ , (Rousseau et al., 2018).

In the second part of this thesis, the influence of considering wear effects when estimating fretting fatigue life was also investigated. Available fretting fatigue data for a Ti-6Al-4V alloy were confronted with both: life estimates taking into account the contact/stress evolution due to material removal and life estimates where these effects are neglected (simplifying approach often adopted). Numerical simulations were carried out through the standard FEM. Results have shown that, considering wear effects allow us to slightly improve the accuracy of life predictions, where results were less scattered when compared to estimates obtained when wear is disregarded. In order to estimate the fatigue life, the TCD has been used in association with three different multiaxial fatigue criteria (SWT, Findley and MWCM). When considering wear effects, all the models provided

errors smaller than 85 % which is quite good in terms of fatigue. Additionally, the SWT normal stress based criterion led to less conservative estimates when compared to Findley and MWCM approaches (shear stress based models). On the other hand, neglecting wear effects led to more scattered estimates. However, only for one of the load configurations here assessed, SWT and MWCM multiaxial fatigue criteria provided errors around 160 %, while the other cases studied yielded errors less than 75 % in the estimates. In this setting, for the experimental data that one has assessed, i.e. fretting fatigue conditions under partial slip regime, neglecting wear effects in terms of material removal does not seem to strongly decrease the accuracy of life predictions, which on the other hand saves a lot of computational cost mainly if we are dealing with complex real components. Note that many fretting cycles need to be evaluated when simulating wear, which is not the case when it is disregarded. In this case, only the information from one cycle is needed.

## 5.2 Suggestions for future work

Concerning the enrichment technique presented in Chapter 3, spatial reference fields used in order to enrich the displacement field close to the contact edges under fretting conditions were obtained for the cylinder on plane contact configuration. It would be interesting to apply similar methodologies to the ones here presented in order to validate the applicability of it for generic geometric configurations, for example, when considering flat punch pads with rounded edges, or even complete contacts. The latter, has the advantage that the position of the contact edges is easily known despite the mesh refinement, however, the strong stress singularity nearby the contact edges may lead to challenges for instance when applying the mechanical field decomposition presented in Section 3.1. Another geometric related applicability that should be verified is the assessment of the enrichment technique here considered for 3D analyses. Even though this work was more focused on the use of the spatial reference fields in order to enrich simulations carried out on coarse meshes, a promising branch also related to the crack analogue here explored is the use of the nonlocal intensity factors presented in Section 3.1 aiming to define crack initiation boundaries, which was already the object of study in (Ferry et al., 2017) and is one of the aims of Guillaume Rousseau (Rousseau et al., 2018) who is currently conducting his PhD at the ENS Paris-Saclay.

It is also worth noting that, the enrichment-based approach assessed in this work demands a previous knowledge of the problem's solution behaviour in critical zones. For more complex cases, for instance the ones involving elastoplastic analyses or material inhomogeneities, solutions behaviour are not readily available. However, this issue can be overcome by using multi-modelling techniques such as the Arlequin method (Ben Dhia, 1998; Ben Dhia and Jamond, 2010; Néron et al., 2016), which consists in the superposition of local models with a global one. In this case, the superposition technique is based on an energy formulation, where it is distributed among the various models used. To the author's opinion, this is a promising branch that could be investigated in future works.

With respect to the fretting fatigue life estimate considering wear effects, more sophisticated models which include friction coefficient variation, third body effects and the inclusion of propagating cracks would be interesting in an attempt to understand better the failure mechanisms involved in such problems. Even elasto-plastic analysis may become necessary in cases where stress concentrations due to geometric modifications surpass the

material elastic regime. In addition, HCF fretting tests under partial slip conditions with different materials would be very interesting, specially for those more susceptible to wear when compared to the Ti-6Al-4V here investigated.

Concerning fatigue life estimate, this work considered a very simple uncouple damage model (Miner's rule), although the present analysis would also profit the use of more recent and sophisticated coupled or uncoupled damage models (Hojjati-Talemi et al., 2014; Zhang et al., 2012; Shen et al., 2015).

# Bibliography

- Abaqus (2013). *ABAQUS User's Manuals, Version 6.13*. Dassault Systemes Simulia Corp.
- Araújo, J. A. and Nowell, D. (1999). Analysis of pad size effects in fretting fatigue using short crack arrest methodologies. *International Journal of Fatigue*, 21(9):947–956.
- Araujo, J. A. and Nowell, D. (2002). The effect of rapidly varying contact stress fields on fretting fatigue. *International Journal of Fatigue*, 24(7):763–775.
- Araujo, J. A., Nowell, D., and Vivacqua, R. C. (2004). The use of multiaxial fatigue models to predict fretting fatigue life of components subjected to different contact stress fields. *Fatigue & Fracture of Engineering Materials & Structures*, 27(10):967–978.
- Araújo, J. A., Susmel, L., Pires, M. S. T., and Castro, F. C. (2017). A multiaxial stress-based critical distance methodology to estimate fretting fatigue life. *Tribology International*, 108:2–6.
- Araújo, J. A., Susmel, L., Taylor, D., Ferro, J. C. T., and Ferreira, J. L. A. (2008). On the prediction of high-cycle fretting fatigue strength: Theory of critical distances vs. hot-spot approach. *Engineering Fracture Mechanics*, 75(7):1763–1778.
- Araújo, J. A., Susmel, L., Taylor, D., Ferro, J. C. T., and Mamiya, E. N. (2007). On the use of the theory of critical distances and the modified wöhler curve method to estimate fretting fatigue strength of cylindrical contacts. *International Journal of Fatigue*, 29(1):95–107.
- Archard, J. F. (1953). Contact and rubbing of flat surfaces. *Journal of applied physics*, 24(8):981–988.
- Baietto, M. C., Pierres, E., Gravouil, A., Berthel, B., Fouvry, S., and Trolle, B. (2013). Fretting fatigue crack growth simulation based on a combined experimental and xfm strategy. *International Journal of Fatigue*, 47:31–43.
- Basquin, O. H. (1910). The exponential law of endurance tests. In *Proc Am Soc Test Mater*, volume 10, pages 625–630.
- Basseville, S., Hériprié, E., and Cailletaud, G. (2011). Numerical simulation of the third body in fretting problems. *Wear*, 270(11-12):876–887.
- Bellecave, J., Pommier, S., Nadot, Y., Meriaux, J., and Araújo, J. A. (2014). T-stress based short crack growth model for fretting fatigue. *Tribology International*, 76:23–34.

- Ben Dhia, H. (1998). Multiscale mechanical problems: the arlequin method. *Comptes Rendus de l'Academie des Sciences Series IIB Mechanics Physics Astronomy*, 12(326):899–904.
- Ben Dhia, H. and Jamond, O. (2010). On the use of xfm within the arlequin framework for the simulation of crack propagation. *Computer methods in applied mechanics and engineering*, 199(21-22):1403–1414.
- Ben Dhia, H. and Torkhani, M. (2008). Modeling of wear in the arlequin framework.
- Bramhall, R. (1973). *Studies in fretting fatigue*. PhD thesis, University of Oxford.
- Campbell, F. C. (2008). *Elements of metallurgy and engineering alloys*. ASM International.
- Carpinteri, A., de Freitas, M., and Spagnoli, A. (2003). The influence of static mean stresses applied normal to the maximum shear planes in multiaxial fatigue. *Biaxial/Multiaxial Fatigue and Fracture*, 31:123.
- Castro, F. C., Araújo, J. A., Mamiya, E. N., and Zouain, N. (2009). Remarks on multiaxial fatigue limit criteria based on prismatic hulls and ellipsoids. *International Journal of Fatigue*, 31(11-12):1875–1881.
- Cattaneo, C. (1938). Sul contatto di due corpi elastici: distribuzione locale degli sforzi. *Rend. Accad. Naz. Lincei*, 27(6):342–348.
- Cavalcante, B., Shaterzadeh-Yazdi, M., Sollero, P., Albuquerque, E. L., and Doca, T. (2017). Analysis of a cattaneo-mindlin problem using the boundary element method. *Tribology International*, 108:194–201.
- Champaney, L., Cognard, J., and Ladeveze, P. (1999). Modular analysis of assemblages of three-dimensional structures with unilateral contact conditions. *Computers & Structures*, 73(1-5):249–266.
- Chatterjee, A. (2000). An introduction to the proper orthogonal decomposition. *Current science*, pages 808–817.
- Chinesta, F., Ladeveze, P., and Cueto, E. (2011). A short review on model order reduction based on proper generalized decomposition. *Archives of Computational Methods in Engineering*, 18(4):395.
- Ciavarella, M. (2003). A crack-likenotch analogue for a safe-life fretting fatigue design methodology. *Fatigue & Fracture of Engineering Materials & Structures*, 26(12):1159–1170.
- Ciavarella, M., Dini, D., and Demelio, G. P. (2001). Fretting fatigue, surface damage or fatigue phenomenon. In *10th International Conference on Fracture, Honolulu*.
- Ciavarella, M. and Hills, D. A. (1999). Brief note: Some observations on oscillating tangential forces and wear in general plane contacts. *European Journal of Mechanics-A/Solids*, 18(3):491–497.

- Cognard, J.-Y., Dureisseix, D., Ladevèze, P., and Lorong, P. (1996). Expérimentation d'une approche parallèle en calcul des structures. *Revue Européenne des Éléments Finis*, 5(2):197–220.
- Creager, M. and Paris, P. C. (1967). Elastic field equations for blunt cracks with reference to stress corrosion cracking. *International Journal of Fracture Mechanics*, 3(4):247–252.
- Cruzado, A., Leen, S. B., Urchegui, M. A., and Gómez, X. (2013). Finite element simulation of fretting wear and fatigue in thin steel wires. *International Journal of Fatigue*, 55:7–21.
- Dang Van, K., Griveau, B., and Message, O. (1989). On a new multiaxial fatigue limit criterion: theory and application. In *Biaxial and Multiaxial Fatigue (EGF3)*.
- de Pannemaecker, A., Fouvry, S., and Buffiere, J. Y. (2015). Reverse identification of short–long crack threshold fatigue stress intensity factors from plain fretting crack arrest analysis. *Engineering Fracture Mechanics*, 134:267–285.
- Ding, J., Leen, S. B., and McColl, I. R. (2004). The effect of slip regime on fretting wear-induced stress evolution. *International journal of fatigue*, 26(5):521–531.
- Ding, J., McColl, I. R., Leen, S. B., and Shipway, P. H. (2007). A finite element based approach to simulating the effects of debris on fretting wear. *Wear*, 263(1-6):481–491.
- Dini, D., Nowell, D., and Dyson, I. N. (2006). The use of notch and short crack approaches to fretting fatigue threshold prediction: Theory and experimental validation. *Tribology international*, 39(10):1158–1165.
- Doca, T. and Pires, F. A. (2017). Finite element modeling of wear using the dissipated energy method coupled with a dual mortar contact formulation. *Computers & Structures*, 191:62–79.
- Dubourg, M. C., Chateauminois, A., and Villechaise, B. (2003). In situ analysis and modeling of crack initiation and propagation within model fretting contacts using polymer materials. *Tribology International*, 36(2):109–119.
- Eden, E. M., Rose, W. N., and Cunningham, P. L. (1911). The endurance of metals: experiments on rotating beams at university college, london. *Proceedings of the Institution of Mechanical Engineers*, 81(1):839–974.
- El Haddad, M. H., Smith, K. N., and Topper, T. H. (1979). Fatigue crack propagation of short cracks. *Journal of Engineering Materials and Technology*, 101(1):42–46.
- Endo, K. and Goto, H. (1976). Initiation and propagation of fretting fatigue cracks. *Wear*, 38(2):311–324.
- Fadag, H., Mall, S., and Jain, V. (2008). A finite element analysis of fretting fatigue crack growth behavior in ti-6al-4v. *Engineering Fracture Mechanics*, 75(6):1384–1399.
- Ferry, B. (2017). *Study of the stress gradient effect and the size effect in fretting fatigue*. PhD thesis, Université Paris-Saclay and University of Brasilia.

- Ferry, B., Araújo, J. A., Pommier, S., and Demmou, K. (2017). Life of a ti-6al-4v alloy under fretting fatigue: Study of new nonlocal parameters. *Tribology International*, 108:23–31.
- Findley, W. N. (1958). *A theory for the effect of mean stress on fatigue of metals under combined torsion and axial load or bending*. Number 6. Engineering Materials Research Laboratory, Division of Engineering, Brown University.
- Fouvry, S., Gallien, H., and Berthel, B. (2014). From uni-to multi-axial fretting-fatigue crack nucleation: Development of a stress-gradient-dependent critical distance approach. *International Journal of Fatigue*, 62:194–209.
- Fouvry, S., Liskiewicz, T., Kapsa, P., Hannel, S., and Sauger, E. (2003). An energy description of wear mechanisms and its applications to oscillating sliding contacts. *Wear*, 255(1-6):287–298.
- Fouvry, S., Nowell, D., Kubiak, K., and Hills, D. A. (2008). Prediction of fretting crack propagation based on a short crack methodology. *Engineering Fracture Mechanics*, 75(6):1605–1622.
- Fuenmayor, F. J., Giner, E., and Tur, M. (2005). Extraction of the generalized stress intensity factor in gross sliding complete contacts using a path-independent integral. *Fatigue & Fracture of Engineering Materials & Structures*, 28(12):1071–1085.
- Garcin, S., Fouvry, S., and Heredia, S. (2015). A fem fretting map modeling: Effect of surface wear on crack nucleation. *Wear*, 330:145–159.
- Gerber, W. (1874). Relation between the superior and inferior stresses of a cycle of limiting stress. *Zeit. Bayerischen Arch. Ing.-Vereins*.
- Giacoma, A., Dureisseix, D., Gravouil, A., and Rochette, M. (2014). A multiscale large time increment/fas algorithm with time-space model reduction for frictional contact problems. *International Journal for Numerical Methods in Engineering*, 97(3):207–230.
- Giannakopoulos, A. E., Lindley, T. C., and Suresh, S. (1998). Aspects of equivalence between contact mechanics and fracture mechanics: theoretical connections and a life-prediction methodology for fretting-fatigue. *Acta materialia*, 46(9):2955–2968.
- Giannakopoulos, A. E., Lindley, T. C., Suresh, S., and Chenut, C. (2000). Similarities of stress concentrations in contact at round punches and fatigue at notches: implications to fretting fatigue crack initiation. *Fatigue and Fracture of Engineering Materials and Structures*, 23(7):561–572.
- Giner, E., Sabsabi, M., Ródenas, J. J., and Fuenmayor, F. (2014). Direction of crack propagation in a complete contact fretting-fatigue problem. *International Journal of Fatigue*, 58:172–180.
- Giner, E., Sukumar, N., Denia, F. D., and Fuenmayor, F. J. (2008a). Extended finite element method for fretting fatigue crack propagation. *International Journal of Solids and Structures*, 45(22-23):5675–5687.

- Giner, E., Sukumar, N., Fuenmayor, F. J., and Vercher, A. (2008b). Singularity enrichment for complete sliding contact using the partition of unity finite element method. *International journal for numerical methods in engineering*, 76(9):1402–1418.
- Giner, E., Tur, M., Vercher, A., and Fuenmayor, F. J. (2009). Numerical modelling of crack–contact interaction in 2d incomplete fretting contacts using x-fem. *Tribology International*, 42(9):1269–1275.
- Goh, C. H., McDowell, D. L., and Neu, R. W. (2006). Plasticity in polycrystalline fretting fatigue contacts. *Journal of the Mechanics and Physics of Solids*, 54(2):340–367.
- Goodman, J. (1899). *Mechanics applied to engineering*. Longmans, Green.
- Gordelier, S. C. and Chivers, T. C. (1979). A literature review of palliatives for fretting fatigue. *Wear*, 56(1):177–190.
- Gough, H. J. (1949). Engineering steels under combined cyclic and static stresses. *Proceedings of the Institution of Mechanical Engineers*, 160(1):417–440.
- Gough, H. J. and Pollard, H. V. (1935). The strength of metals under combined alternating stresses. *Proceedings of the institution of mechanical engineers*, 131(1):3–103.
- Gravouil, A., Pierres, E., and Baietto, M. C. (2011). Stabilized global–local x-fem for 3d non-planar frictional crack using relevant meshes. *International Journal for Numerical Methods in Engineering*, 88(13):1449–1475.
- Haigh, B. P. (1917). Experiments on the fatigue of brasses. *Journal of the Institute of Metals*, 18:55–86.
- Hannel, S., Fouvry, S., Kapsa, P., and Vincent, L. (2001). The fretting sliding transition as a criterion for electrical contact performance. *Wear*, 249(9):761–770.
- Hattori, T., Nakamura, M., and Watanabe, T. (2003). Simulation of fretting-fatigue life by using stress-singularity parameters and fracture mechanics. *Tribology international*, 36(2):87–97.
- Hertz, H. (1882). Über die berührung fester elastischer körper. *Journal für die reine und angewandte Mathematik*, 92:156–171.
- Hills, D. A. and Nowell, D. (1994). *Mechanics of Fretting-Fatigue*. Kluwer Academic Publishers.
- Hills, D. A., Nowell, D., and O’Connor, J. J. (1988). On the mechanics of fretting fatigue. *Wear*, 125(1-2):129–146.
- Hojjati-Talemi, R., Wahab, M. A., and De Baets, P. (2014). Finite element simulation of phase difference effects on fretting fatigue crack nucleation behaviour. *Proceedings of the Institution of Mechanical Engineers, Part J: Journal of Engineering Tribology*, 228(4):470–479.
- Jin, O. and Mall, S. (2004). Effects of slip on fretting behavior: experiments and analyses. *Wear*, 256(7-8):671–684.
- Johnson, K. L. (1987). *Contact mechanics*. Cambridge university press.



- Kallmeyer, A. R., Krgo, A., and Kurath, P. (2002). Evaluation of multiaxial fatigue life prediction methodologies for ti-6al-4v. *Journal of engineering materials and technology*, 124(2):229–237.
- Khoei, A. R. (2014). *Extended finite element method: theory and applications*. John Wiley & Sons.
- Kikuchi, N. and Oden, J. T. (1988). *Contact problems in elasticity: a study of variational inequalities and finite element methods*, volume 8. siam.
- Laborde, P., Pommier, J., Renard, Y., and Salaün, M. (2005). High-order extended finite element method for cracked domains. *International Journal for Numerical Methods in Engineering*, 64(3):354–381.
- Ladevèze, P. (2012). *Nonlinear computational structural mechanics: new approaches and non-incremental methods of calculation*. Springer Science & Business Media.
- Ladevèze, P., Passieux, J. C., and Néron, D. (2010). The latin multiscale computational method and the proper generalized decomposition. *Computer Methods in Applied Mechanics and Engineering*, 199(21-22):1287–1296.
- Laursen, T. A. (2013). *Computational contact and impact mechanics: fundamentals of modeling interfacial phenomena in nonlinear finite element analysis*. Springer Science & Business Media.
- Le Biavant-Guerrier, K. (2000). *Etude de l'amorçage de fissures de fatigue dans le Ti-6Al-4V*. PhD thesis, Ecole Centrale Paris.
- Liang, Y., Lee, H., Lim, S., Lin, W., Lee, K., and Wu, C. (2002). Proper orthogonal decomposition and its applications part i: Theory. *Journal of Sound and vibration*, 252(3):527–544.
- Madge, J. J. (2009). *Numerical modelling of the effect of fretting wear on fretting fatigue*. PhD thesis, University of Nottingham.
- Madge, J. J., Leen, S. B., McColl, I. R., and Shipway, P. H. (2007a). Contact-evolution based prediction of fretting fatigue life: effect of slip amplitude. *Wear*, 262(9-10):1159–1170.
- Madge, J. J., Leen, S. B., and Shipway, P. H. (2007b). The critical role of fretting wear in the analysis of fretting fatigue. *Wear*, 263(1-6):542–551.
- Mamiya, E. N. and Araújo, J. A. (2002). Fatigue limit under multiaxial loadings: on the definition of the equivalent shear stress. *Mechanics Research Communications*, 29(2-3):141–151.
- Mamiya, E. N., Araújo, J. A., and Castro, F. C. (2009). Prismatic hull: a new measure of shear stress amplitude in multiaxial high cycle fatigue. *International Journal of Fatigue*, 31(7):1144–1153.
- Martins, L. H. L., Rossino, L. S., Filho, W. B., and Araújo, J. A. (2008). Detailed design of fretting fatigue apparatus and tests on 7050-t7451 al alloy. *Tribology-Materials, Surfaces & Interfaces*, 2(1):39–49.

- Matsuishi, M. and Endo, T. (1968). Fatigue of metals subjected to varying stress. *Japan Society of Mechanical Engineers, Fukuoka, Japan*, 68(2):37–40.
- McColl, I. R., Ding, J., and Leen, S. B. (2004). Finite element simulation and experimental validation of fretting wear. *Wear*, 256(11-12):1114–1127.
- McDowell, J. (1952). Fretting corrosion tendencies of several combinations of materials. In *Symposium on fretting corrosion*. ASTM International.
- Meggiolaro, M. A. and de Castro, J. T. P. (2015). The moment of inertia method to calculate equivalent ranges in non-proportional tension–torsion histories. *Journal of Materials Research and Technology*, 4(3):229–234.
- Mindlin, R. D. (1949). Compliance of elastic bodies in contact. *J. appl. Mech.*, 16:259–268.
- Miner, M. A. (1945). Cumulative damage in fatigue. *Journal of Applied Mechanics*, 12:A159–A164.
- Moës, N., Dolbow, J., and Belytschko, T. (1999). A finite element method for crack growth without remeshing. *Int. J. Numer. Meth. Engng*, 46:131–150.
- Moës, N., Gravouil, A., and Belytschko, T. (2002). Non-planar 3d crack growth by the extended finite element and level setpart i: Mechanical model. *International Journal for Numerical Methods in Engineering*, 53(11):2549–2568.
- Montebello, C. (2015). *Analysis of the stress gradient effect in Fretting-Fatigue through a description based on nonlocal intensity factors*. PhD thesis, Université Paris-Saclay.
- Montebello, C., Pommier, S., Demmou, K., Leroux, J., and Meriaux, J. (2016). Analysis of the stress gradient effect in fretting-fatigue through nonlocal intensity factors. *International Journal of Fatigue*, 82:188–198.
- Munoz, S., Proudhon, H., Dominguez, J., and Fouvry, S. (2006). Prediction of the crack extension under fretting wear loading conditions. *International Journal of Fatigue*, 28(12):1769–1779.
- Muskhelishvili, N. I. (1953). *Some basic problems of the mathematical theory of elasticity*. P. Noordhoff.
- Navarro, C., Muñoz, S., and Dominguez, J. (2008). On the use of multiaxial fatigue criteria for fretting fatigue life assessment. *International Journal of fatigue*, 30(1):32–44.
- Néron, D., Ben Dhia, H., and Cottureau, R. (2016). A decoupled strategy to solve reduced-order multimodel problems in the pgd and arlequin frameworks. *Computational Mechanics*, 57(4):509–521.
- Néron, D. and Ladevèze, P. (2010). Proper generalized decomposition for multiscale and multiphysics problems. *Archives of Computational Methods in Engineering*, 17(4):351–372.
- Nesládek, M., Španiel, M., Jurenka, J., Ružička, J., and Kuželka, J. (2012). Fretting fatigue—experimental and numerical approaches. *International Journal of Fatigue*, 44:61–73.

- Nishioka, K. and Hirakawa, K. (1969a). Fundamental investigations of fretting fatigue: part 2, fretting fatigue testing machine and some test results. *Bulletin of JSME*, 12(50):180–187.
- Nishioka, K. and Hirakawa, K. (1969b). Fundamental investigations of fretting fatigue: part 3, some phenomena and mechanisms of surface cracks. *Bulletin of JSME*, 12(51):397–407.
- Nishioka, K. and Hirakawa, K. (1969c). Fundamental investigations of fretting fatigue: part 4, the effect of mean stress. *Bulletin of JSME*, 12(51):408–414.
- Nishioka, K. and Hirakawa, K. (1969d). Fundamental investigations of fretting fatigue: Part 5, the effect of relative slip amplitude. *Bulletin of JSME*, 12(52):692–697.
- Nishioka, K. and Kenji, H. (1972). Fundamental investigations of fretting fatigue: Part 6, effects of contact pressure and hardness of materials. *Bulletin of JSME*, 15(80):135–144.
- Nowell, D. (1988). *An analysis of fretting fatigue*. PhD thesis, University of Oxford.
- Palmgren, A. (1924). Die lebensdauer von kugellagern. *Zeitschrift des Vereines Duetsher Ingenieure*, 68:339–341.
- Papanikos, P., Meguid, S. A., and Stjepanovic, Z. (1998). Three-dimensional nonlinear finite element analysis of dovetail joints in aeroengine discs. *Finite elements in analysis and design*, 29(3):173–186.
- Pierres, E., Baietto, M.-C., and Gravouil, A. (2011). Experimental and numerical analysis of fretting crack formation based on 3d x-fem frictional contact fatigue crack model. *Comptes Rendus Mécanique*, 339(7-8):532–551.
- Pierres, E., Baietto, M. C., Gravouil, A., and Morales-Espejel, G. (2010). 3d two scale x-fem crack model with interfacial frictional contact: Application to fretting fatigue. *Tribology International*, 43(10):1831–1841.
- Pommier, S., Lopez-Crespo, P., and Decreuse, P. Y. (2009). A multi-scale approach to condense the cyclic elastic-plastic behaviour of the crack tip region into an extended constitutive model. *Fatigue & Fracture of Engineering Materials & Structures*, 32(11):899–915.
- Rajasekaran, R. and Nowell, D. (2006). Fretting fatigue in dovetail blade roots: experiment and analysis. *Tribology International*, 39(10):1277–1285.
- Ribeaucourt, R. (2006). *Gestion du contact avec frottement le long des faces de fissures dans le cadre de la méthode X-FEM. Application à la fatigue tribologique*. PhD thesis, INSA de Lyon.
- Ribeaucourt, R., Baietto, M. C., and Gravouil, A. (2007). A new fatigue frictional contact crack propagation model with the coupled x-fem/latin method. *Computer Methods in Applied Mechanics and Engineering*, 196(33):3230–3247.
- Rodríguez-Tembleque, L., Abascal, R., and Aliabadi, M. (2011). A boundary elements formulation for 3d fretting-wear problems. *Engineering analysis with boundary elements*, 35(7):935–943.

- Rossino, L. S., Castro, F. C., Bose Filho, W. W., and Araújo, J. A. (2009). Issues on the mean stress effect in fretting fatigue of a 7050-t7451 al alloy posed by new experimental data. *International Journal of Fatigue*, 31(11):2041–2048.
- Rousseau, G., Montebello, C., Guilhem, Y., and Pommier, S. (2018). A novel approach to predict fretting fatigue crack initiation. In *MATEC Web of Conferences*, volume 165, page 11003. EDP Sciences.
- Ruiz, C., Boddington, P. H. B., and Chen, K. C. (1984). An investigation of fatigue and fretting in a dovetail joint. *Experimental mechanics*, 24(3):208–217.
- Shen, F., Hu, W., and Meng, Q. (2015). A damage mechanics approach to fretting fatigue life prediction with consideration of elastic–plastic damage model and wear. *Tribology International*, 82:176–190.
- Silva, M. Z. (2016). Estudo da influência do desgaste na falha prematura de componentes de linhas de ancoragem. Master’s thesis, University of Brasilia.
- Smith, R. N., Watson, P., and Topper, T. H. (1970). A stress-strain parameter for the fatigue of metals. *Journal of Materials*, 5(4):767–788.
- Socie, D. F. and Marquis, G. B. (2000). *Multiaxial fatigue*. Society of Automotive Engineers Warrendale, PA.
- Soderberg, C. R. (1939). Factor of safety and working stress. *Trans Am Soc Mech Eng*, 52:13–28.
- Sukumar, N., Chopp, D. L., Moës, N., and Belytschko, T. (2001). Modeling holes and inclusions by level sets in the extended finite-element method. *Computer methods in applied mechanics and engineering*, 190(46):6183–6200.
- Sukumar, N., Moës, N., Moran, B., and Belytschko, T. (2000). Extended finite element method for three-dimensional crack modelling. *International Journal for Numerical Methods in Engineering*, 48(11):1549–1570.
- Sum, W. S., Williams, E. J., and Leen, S. B. (2005). Finite element, critical-plane, fatigue life prediction of simple and complex contact configurations. *International Journal of Fatigue*, 27(4):403–416.
- Susmel, L. (2008). Multiaxial fatigue limits and material sensitivity to non-zero mean stresses normal to the critical planes. *Fatigue & Fracture of Engineering Materials & Structures*, 31(3-4):295–309.
- Susmel, L. (2009). *Multiaxial notch fatigue*. Elsevier.
- Susmel, L. and Lazzarin, P. (2002). A bi-parametric wöhler curve for high cycle multiaxial fatigue assessment. *Fatigue & Fracture of Engineering Materials & Structures*, 25(1):63–78.
- Susmel, L. and Taylor, D. (2007). A novel formulation of the theory of critical distances to estimate lifetime of notched components in the medium-cycle fatigue regime. *Fatigue & Fracture of Engineering Materials & Structures*, 30(7):567–581.

- Susmel, L. and Taylor, D. (2008). The modified wöhler curve method applied along with the theory of critical distances to estimate finite life of notched components subjected to complex multiaxial loading paths. *Fatigue & Fracture of Engineering Materials & Structures*, 31(12):1047–1064.
- Susmel, L., Taylor, D., et al. (2006). Can the conventional high-cycle multiaxial fatigue criteria be re-interpreted in terms of the theory of critical distances. *Structural Durability & Health Monitoring*, 2(2):91–108.
- Szolwinski, M. P. and Farris, T. N. (1996). Mechanics of fretting fatigue crack formation. *Wear*, 198(1-2):93–107.
- Talemi, R. H. and Wahab, M. A. (2012). Finite element analysis of localized plasticity in al 2024-t3 subjected to fretting fatigue. *Tribology transactions*, 55(6):805–814.
- Taylor, D. (1999). Geometrical effects in fatigue: a unifying theoretical model. *International Journal of Fatigue*, 21(5):413–420.
- Taylor, D. (2011). Applications of the theory of critical distances in failure analysis. *Engineering Failure Analysis*, 18(2):543–549.
- Tomlinson, G. A. (1927). The rusting of steel surfaces in contact. *Proceedings of the Royal Society of London. Series A, Containing Papers of a Mathematical and Physical Character*, 115(771):472–483.
- Trollé, B., Gravouil, A., Baietto, M. C., and Nguyen-Tajan, T. M. L. (2012). Optimization of a stabilized x-fem formulation for frictional cracks. *Finite Elements in Analysis and Design*, 59:18–27.
- Tsai, C. and Mall, S. (2000). Elasto-plastic finite element analysis of fretting stresses in pre-stressed strip in contact with cylindrical pad. *Finite elements in analysis and design*, 36(2):171–187.
- Vingsbo, O. and Söderberg, S. (1988). On fretting maps. *Wear*, 126(2):131–147.
- Wang, Z., Jin, X., Keer, L. M., and Wang, Q. (2012). A numerical approach for analyzing three-dimensional steady-state rolling contact including creep using a fast semi-analytical method. *Tribology Transactions*, 55(4):446–457.
- Warlow-Davies, E. J. (1941). Fretting corrosion and fatigue strength: brief results of preliminary experiments. *Proceedings of the Institution of Mechanical Engineers*, 146(1):32–38.
- Waterhouse, R. B. (1992). Fretting wear in asm handbook, friction lubrication, and wear thecnology. *ASM International*, 18:242–256.
- Wittkowsky, B. U., Birch, P. R., Dominguez, J., and Suresh, S. (2000). An experimental investigation of fretting fatigue with spherical contact in 7075-t6 aluminum alloy. In *Fretting fatigue: current technology and practices*. ASTM International.
- Wöhler, A. (1870). *Über die Festigkeits-versuche mit Eisen und Stahl*.
- Wriggers, P. (1995). Finite element algorithms for contact problems. *Archives of Computational Methods in Engineering*, 2(4):1–49.

- Wright, G. P. and O'Connor, J. J. (1972). The influence of fretting and geometric stress concentrations on the fatigue strength of clamped joints. *Proceedings of the Institution of Mechanical Engineers*, 186(1):827–835.
- Yastrebov, V. A. (2013). *Numerical methods in contact mechanics*. John Wiley & Sons.
- Yue, T. and Wahab, M. A. (2017). Finite element analysis of fretting wear under variable coefficient of friction and different contact regimes. *Tribology International*, 107:274–282.
- Zhang, T., McHugh, P., and Leen, S. (2012). Finite element implementation of multiaxial continuum damage mechanics for plain and fretting fatigue. *International Journal of Fatigue*, 44:260–272.
- Zhou, Z. R. and Vincent, L. (1995). Mixed fretting regime. *Wear*, 181:531–536.

# Appendix A

## Velocity fields and spatial reference fields computation

As presented in Section 3.1, the velocity field in the vicinity of the contact edges can be partitioned into a product of spatial reference fields associated to the local geometry of the problem and nonlocal intensity factors associated to the macroscopic loads, Eq. (3.1). In this case, the velocity field is computed with respect to a reference frame attached to the contact edges, Fig. A.1.

$$\underline{v}_{R'}(t) = \underline{v}_R(t) - \underline{v}_{R'R}(t) \quad (\text{A.1})$$

For the sake of notation simplicity, the velocity field computed with respect to the contact edges  $\underline{v}_{R'}(t)$  appears only as  $\underline{v}$  in this work.

As mentioned in Section 3.1, the spatial modes  $\underline{d}^s$  and  $\underline{d}^a$  are computed extracting the velocity field (relative to the contact edge) in some strategic time steps of the load history depicted in Fig. 3.2 (learning phase to generate reduced-order model). In this case:

$$\begin{aligned} \underline{d}^s(\underline{x}) &= \underline{v}(\underline{x}, t_s) \\ \underline{d}^a(\underline{x}) &= \underline{v}(\underline{x}, t_a) \end{aligned} \quad (\text{A.2})$$

Note that  $t_s$  is the time instant where a small perturbation is introduced to the normal load  $P$  while the tangential load  $Q$  is null. On the other hand,  $t_a$  is the time step where

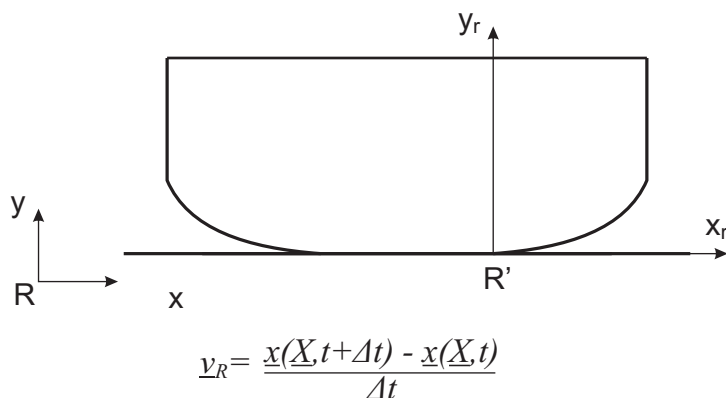


Figure A.1: Reference frame velocity field computation.

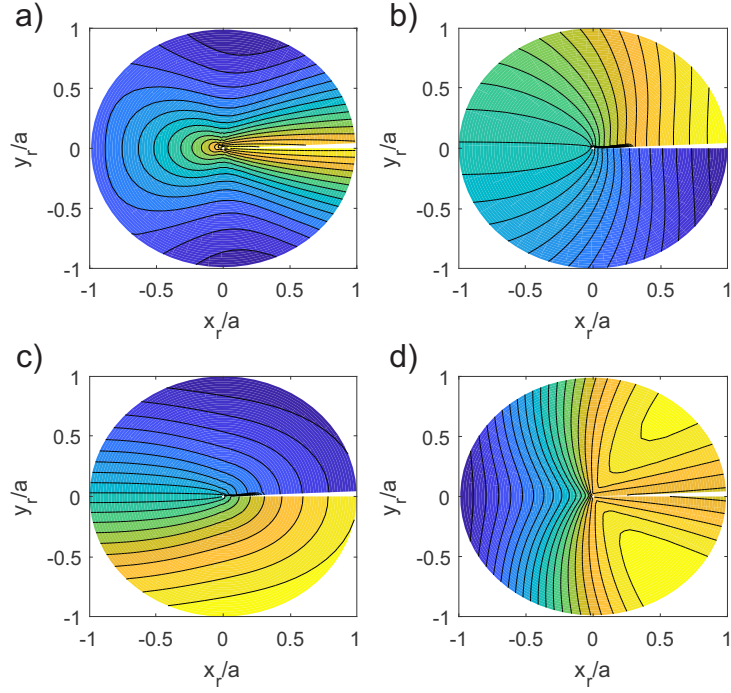


Figure A.2: Spatial fields extracted from FE modelling: (a)  $\underline{d}^s$  on the x direction, (b)  $\underline{d}^s$  on the y direction, (c)  $\underline{d}^a$  on the x direction,  $\underline{d}^a$  on the y direction.

the tangential load  $Q$  starts being reversed (full stick condition) whereas the normal load is kept constant. Doing so, the effects of the normal and tangential loads can be taken into account separately. It is worth mentioning that when these fields are computed in polar coordinates (Eqs. 3.6 and 3.7), they are further normalized in order to be comparable to the displacement field obtained at the crack tip during a elastic loading phase either  $K_I = 1 \text{ MPa } \sqrt{m}$  or  $K_{II} = 1 \text{ MPa } \sqrt{m}$ , Figs. 3.3 and 3.4. A 2D distribution of those spatial reference fields extracted from a FE computation can be found in Fig. A.2. The coordinate system, normalized with respect to the contact semi-width, is expressed in the reference system fixed at the contact edge. The problem solved is depicted in Fig. 3.2. The normal load applied to the pad was  $P = 227 \text{ N/mm}$  and the tangential load  $Q = 169 \text{ N/mm}$ . The small perturbation in the normal load (time instant  $t_s$ ) was equal to  $0.05P$ . The contact parts are elastically similar with the following material properties:  $E = 200 \text{ MPa}$  and  $\nu = 0.3$ . The friction coefficient in the slip zones was assumed as  $\mu = 0.9$ . Linear elastic regime was always assumed.



# Appendix B

## Proper orthogonal decomposition

The proper orthogonal decomposition (POD) works as the basis for the modal decomposition of a set of functions, such as data obtained from experiments or heavy numerical computations (Chatterjee, 2000; Liang et al., 2002). One of the most notorious properties of this method is its optimality: it provides the most efficient way of capturing the dominant terms of a high-dimensional problem with, often, only a few modes.

Suppose that one wants to approximate a certain function  $u(\underline{x}, t)$  over some time-space domain of interest  $[0, T] \times \Omega$ . This function can be approximated as a linear combination of the form:

$$u(\underline{x}, t) \approx \sum_{i=1}^K a_i(t) \phi_i(\underline{x}) \quad (\text{B.1})$$

It is natural to expect that this approximation becomes exact as  $K \rightarrow \infty$ . In order to obtain the approximation functions  $a_i(t)$  and  $\phi_i(\underline{x})$  one has to solve a minimization problem:

$$\left\| u(\underline{x}, t) - \sum_{i=1}^K a_i(t) \phi_i(\underline{x}) \right\|_{L^2} \rightarrow \min \quad (\text{B.2})$$

Notice that the representation of Eq. (B.1) is not unique. On the POD basis, the choice of  $\phi_i(\underline{x})$  is constrained by the following orthonormal property:

$$\int_{\Omega} \phi_i(\underline{x}) \phi_j(\underline{x}) d\Omega = \delta_{ij} \quad (\text{B.3})$$

In this case, the determination of  $a_i(t)$  becomes as simple as then

$$a_i(t) = \int_{\Omega} u(\underline{x}, t) \phi_i(\underline{x}) d\Omega \quad (\text{B.4})$$

Having in mind the numerical application of this work, only the discrete theory of the POD will be presented. Therefore, let us assume that we have a set of  $N$ -dimensional vectors (say,  $M$  of them) stored in a matrix  $\mathbf{U}$ , where  $N$  represents the number of spatial degrees of freedom and  $M$  the number of time snapshots. In this case, the aim is to

find the most accurate description of  $\mathbf{U}$  in some subspace  $W$  with dimension  $K < N$ . Denoting by  $\phi_1, \phi_2, \dots, \phi_K$  the orthonormal basis of  $W$  then each vector from the original set can be approximated as:

$$\mathbf{U} \approx \sum_{j=1}^K \phi_j \mathbf{a}_j^T \quad (\text{B.5})$$

or in terms of the columns of  $\mathbf{U}$

$$\mathbf{u}_i \approx \sum_{j=1}^K a_{ij} \phi_j, \quad i = 1, \dots, M \quad (\text{B.6})$$

The total error of this approximation is given by:

$$Er = \sum_{i=1}^M \left\| \mathbf{u}_i - \sum_{j=1}^K a_{ij} \phi_j \right\|_{L^2}^2 \quad (\text{B.7})$$

Expanding Eq. (B.7):

$$Er = \sum_{i=1}^M \|\mathbf{u}_i\|^2 - 2 \sum_{i=1}^M \sum_{j=1}^K a_{ij} \mathbf{u}_i^T \phi_j + \sum_{i=1}^M \sum_{j=1}^K a_{ij}^2 \quad (\text{B.8})$$

In order to minimize the error, let one first derive Eq. (B.8) with respect to  $a_{ij}$ .

$$\frac{\partial Er}{\partial a_{kl}} = -2 \mathbf{u}_k^T \phi_l + 2 a_{kl} \quad (\text{B.9})$$

where, optimum values for  $a_{kl}$  are given by

$$a_{kl} = \mathbf{u}_k^T \phi_l \quad (\text{B.10})$$

Replacing Eq. (B.10) in Eq. (B.8) and performing a few manipulations:

$$Er = \sum_{i=1}^M \|\mathbf{u}_i\|^2 - \sum_{j=1}^K \phi_j^T \left( \sum_{i=1}^M \mathbf{u}_i \mathbf{u}_i^T \right) \phi_j = \sum_{i=1}^M \|\mathbf{u}_i\|^2 - \sum_{j=1}^K \phi_j^T \mathbf{C} \phi_j \quad (\text{B.11})$$

where  $\mathbf{C}$  is the so-called correlation matrix:

$$\mathbf{C} = \mathbf{U} \mathbf{U}^T \quad (\text{B.12})$$

The problem now consists in minimizing the error expressed by Eq. (B.11) when it is subjected to the following equality constraint:

$$\phi_j^T \phi_j = 1, \quad j = 1, \dots, K \quad (\text{B.13})$$

This optimization problem can be solved using the Lagrange multipliers method which converts the problem into

$$\sum_{i=1}^M \|\mathbf{u}_i\|^2 - \sum_{j=1}^K \phi_j^T \mathbf{C} \phi_j + \sum_{j=1}^K \lambda_j (\phi_j^T \phi_j - 1) \rightarrow \min \quad (\text{B.14})$$

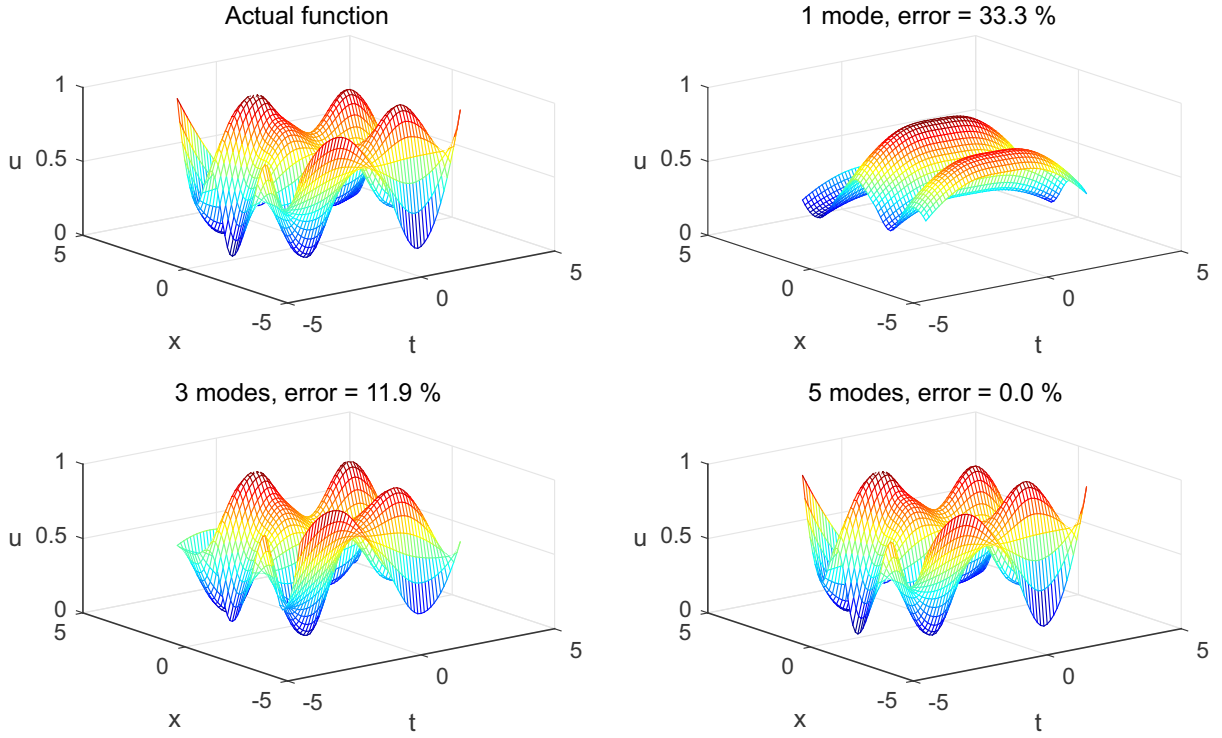


Figure B.1: POD application example.

Then equalizing to zero the first derivative of Eq. (B.14) with respect to  $\phi_j$  one has the following relation

$$\mathbf{C}\phi_j = \lambda_j\phi_j \quad (\text{B.15})$$

which is satisfied when  $\phi_j$  and  $\lambda_j$  are the eigenvectors and the eigenvalues, respectively, of the correlation matrix  $\mathbf{C}$ .

Once that the basis  $\phi_j$  are obtained, the coefficients  $\mathbf{a}_j$  can be determined as:

$$\mathbf{a}_j = \mathbf{U}^T \phi_j \quad (\text{B.16})$$

Fig. B.1 depicts an application of the use of the POD in order to describe a complex field using less degrees of freedom. In this context, a 2D function was generated performing a cubic interpolation on random values distributed along the  $(t, x)$  plane. As can be seen, despite the complexity of the function analysed, only a few modes are capable of describing it properly.

# Appendix C

## Enrichment technique formulation

As already presented in Subsection 3.2, in order to model the displacement field close to the contact edges, the asymptotic functions extracted from the crack analogy (see Section 3.1) are used:

$$\psi_\alpha = \left\{ \sqrt{r} \sin \frac{\theta}{2}, \sqrt{r} \cos \frac{\theta}{2}, \sqrt{r} \sin \frac{\theta}{2} \sin \theta, \sqrt{r} \cos \frac{\theta}{2} \sin \theta \right\} \quad (\text{C.1})$$

The distribution of these four asymptotic functions are shown in Figure C.1, where the reference frame adopted is depicted in Figure C.2. Thus, the enriched displacement field discretization for the fretting problem can be written as:

$$\underline{u}(\underline{x}) = \sum_{i \in I} N_i(\underline{x}) \underline{u}_i + \sum_{j \in J} N_j(\underline{x}) \sum_{\alpha} \psi_\alpha(\underline{x}) \underline{b}_{j,\alpha} \quad (\text{C.2})$$

where  $I$  is the set of all nodes and  $J$  is the set of enriched ones. In this relation,  $\underline{u}_i$  are the standard degrees of freedom associated to the node  $i$  and  $\underline{b}_{j,\alpha}$  are the additional degrees of freedom associated to enrichment function  $\psi_\alpha$  at the node  $j$ .  $N_i$  denotes standard linear shape functions.

Globally, the extended FE approximation of the displacement field, Eq. (C.2), can be summarized as:

$$\underline{u}(\underline{x}, t) = \mathbf{N}^{std}(\underline{x}) \mathbf{U}(t) + \mathbf{N}^{enr}(\underline{x}) \mathbf{A}(t) \quad (\text{C.3})$$

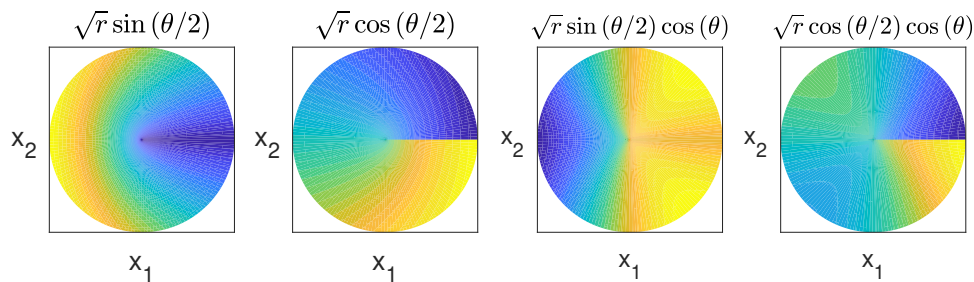


Figure C.1: Schematic view of the asymptotic fretting enrichment functions.

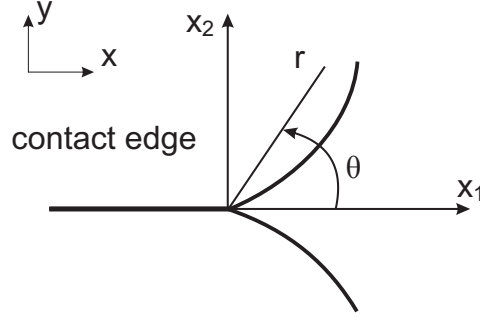


Figure C.2: Reference frame contact edge.

Accordingly, the strain vector corresponding to the approximate displacement field expressed in Eq. (C.3) can be written in terms of the standard and enriched nodal values:

$$\underline{\varepsilon}(\underline{x}, t) = \mathbf{B}^{std}(\underline{x})\mathbf{U}(t) + \mathbf{B}^{enr}(\underline{x})\mathbf{A}(t) \quad (\text{C.4})$$

where the strain vector in 2-D plain strain conditions can be defined as:

$$\underline{\varepsilon} \equiv \begin{bmatrix} \varepsilon_{xx} \\ \varepsilon_{yy} \\ 2\varepsilon_{xy} \end{bmatrix} \quad (\text{C.5})$$

The terms  $\mathbf{B}^{std}$  and  $\mathbf{B}^{enr}$  involve spatial derivatives of  $\mathbf{N}^{std}$  and  $\mathbf{N}^{enr}$ , respectively. In this setting,  $\mathbf{B}^{std} \equiv \mathbf{L}\mathbf{N}^{std}$  and  $\mathbf{B}^{enr} \equiv \mathbf{L}\mathbf{N}^{enr}$ , with  $\mathbf{L}$  denoting the matrix differential operator.

$$\mathbf{L} = \begin{bmatrix} \partial/\partial x & 0 \\ 0 & \partial/\partial y \\ \partial/\partial y & \partial/\partial x \end{bmatrix} \quad (\text{C.6})$$

Recalling the weak form of a contact problem between two elastic bodies under small deformation one has (Section 3.3):

$$\sum_{i=1}^2 \left( \int_{\Omega^{(i)}} \underline{\underline{\sigma}}^{(i)} : \underline{\underline{\varepsilon}}(\underline{u}^{*(i)}) d\Omega - \int_{\Gamma_{\sigma}^{(i)}} \underline{f}_{ext}^{(i)} \cdot \underline{u}^{*(i)} d\Gamma - \int_{\Gamma_c^{(i)}} \underline{f}_c^{(i)} \cdot \underline{u}^{*(i)} d\Gamma \right) = 0, \quad (\text{C.7})$$

$$\forall \underline{u}^{*(i)} \in \mathcal{V}_0^{(i)}$$

For a matter of convenience, for the development of the discretized governing equations, the summation and the superscript indices ( $i$ ) will be dropped from Eq. (C.7). Thus, assuming that the test function  $\underline{u}^*$  can be considered in the same approximating space as the displacement field defined in Eq. (C.3), one can rewrite the weak formulation of the problem in its discretized form as:

$$[\mathbf{U}^{*T} \quad \mathbf{A}^{*T}] \left( \int_{\Omega} \mathbf{B}^T \mathbf{D} \mathbf{B} d\Omega \begin{bmatrix} \mathbf{U} \\ \mathbf{A} \end{bmatrix} - \int_{\Gamma_{\sigma}} \mathbf{N}^T \underline{f}_{ext} d\Gamma - \int_{\Gamma_c} \mathbf{N}^T \underline{f}_c d\Gamma \right) = 0 \quad (\text{C.8})$$

$$\forall \mathbf{U}^{*T}, \mathbf{A}^{*T} \mid \mathbf{U}^{*T}, \mathbf{A}^{*T} = 0 \text{ on } \Gamma_d$$

where  $\mathbf{N} = [\mathbf{N}^{std} \ \mathbf{N}^{enr}]$  and  $\mathbf{B} = [\mathbf{B}^{std} \ \mathbf{B}^{enr}]$  (note  $\Gamma_d$  is the set of surfaces where Dirichlet boundary conditions are prescribed). The discrete system of equations can be finally expressed as:

$$\begin{bmatrix} \int_{\Omega} \mathbf{B}^{stdT} \mathbf{D} \mathbf{B}^{std} d\Omega & \int_{\Omega} \mathbf{B}^{stdT} \mathbf{D} \mathbf{B}^{enr} d\Omega \\ \int_{\Omega} \mathbf{B}^{enrT} \mathbf{D} \mathbf{B}^{std} d\Omega & \int_{\Omega} \mathbf{B}^{enrT} \mathbf{D} \mathbf{B}^{enr} d\Omega \end{bmatrix} [\mathbf{U}] = \begin{bmatrix} \int_{\Gamma_{\sigma}} \mathbf{N}^{stdT} \underline{f}_{ext} d\Gamma + \int_{\Gamma_c} \mathbf{N}^{stdT} \underline{f}_c d\Gamma \\ \int_{\Gamma_{\sigma}} \mathbf{N}^{enrT} \underline{f}_{ext} d\Gamma + \int_{\Gamma_c} \mathbf{N}^{enrT} \underline{f}_c d\Gamma \end{bmatrix} \quad (\text{C.9})$$

This nonlinear problem due to the contact interactions may be solved using the procedure exposed in Subsection 3.3.3, even tough, for the sake of brevity, the enrichments aspects are not considered there.

Defining  $\mathbf{N}_i^{std} = N_i \mathbf{I}$  and  $\mathbf{N}_{i,\alpha}^{enr} = N_i \psi_{\alpha}(\underline{x}_i) \mathbf{I}$ , with  $\mathbf{I}$  denoting a  $2 \times 2$  identity matrix, the matrices  $\mathbf{B}^{std}$  and  $\mathbf{B}^{enr}$  can be defined for the X-FEM formulation using the enriched displacement field for the nodes  $i$  as:

$$\mathbf{B}_i^{std} = \begin{bmatrix} \partial N_i / \partial x & 0 \\ 0 & \partial N_i / \partial y \\ \partial N_i / \partial y & \partial N_i / \partial x \end{bmatrix} \quad (\text{C.10})$$

$$\mathbf{B}_{i,\alpha}^{enr} = \begin{bmatrix} \partial(N_i \psi_{\alpha}(\underline{x})) / \partial x & 0 \\ 0 & \partial(N_i \psi_{\alpha}(\underline{x})) / \partial y \\ \partial(N_i \psi_{\alpha}(\underline{x})) / \partial y & \partial(N_i \psi_{\alpha}(\underline{x})) / \partial x \end{bmatrix} \quad (\text{C.11})$$

where the derivative of the asymptotic fretting functions is

$$\frac{\partial}{\partial \underline{x}} (N_i \psi_{\alpha}(\underline{x})) = \frac{\partial N_i}{\partial \underline{x}} \psi_{\alpha}(\underline{x}) + N_i \frac{\partial \psi_{\alpha}(\underline{x})}{\partial \underline{x}} \quad (\text{C.12})$$

in which  $\partial \psi_{\alpha}(\underline{x}) / \partial \underline{x}$  can be obtained firstly using a transformation from polar to Cartesian coordinates in a reference frame  $(x_1, x_2)$  attached at the contact edge of the problem in study, Figure C.2.

$$\begin{aligned} \frac{\partial \psi_{\alpha}}{\partial x_1} &= \frac{\partial \psi_{\alpha}}{\partial r} \frac{\partial r}{\partial x_1} + \frac{\partial \psi_{\alpha}}{\partial \theta} \frac{\partial \theta}{\partial x_1} \\ \frac{\partial \psi_{\alpha}}{\partial x_2} &= \frac{\partial \psi_{\alpha}}{\partial r} \frac{\partial r}{\partial x_2} + \frac{\partial \psi_{\alpha}}{\partial \theta} \frac{\partial \theta}{\partial x_2} \end{aligned} \quad (\text{C.13})$$

where  $\partial r / \partial x_1 = \cos \theta$ ,  $\partial r / \partial x_2 = \sin \theta$ ,  $\partial \theta / \partial x_1 = -\sin \theta / r$  and  $\partial \theta / \partial x_2 = \cos \theta / r$ . Hence, the local derivatives of the enrichment functions  $\psi_{\alpha}$  can be obtained using the relation expressed by Eq. (C.13).

$$\begin{aligned} \frac{\partial \psi_1}{\partial x_1} &= -\frac{1}{2\sqrt{r}} \sin \frac{\theta}{2}, \quad \frac{\partial \psi_1}{\partial x_2} = \frac{1}{2\sqrt{r}} \cos \frac{\theta}{2} \\ \frac{\partial \psi_2}{\partial x_1} &= \frac{1}{2\sqrt{r}} \cos \frac{\theta}{2}, \quad \frac{\partial \psi_2}{\partial x_2} = \frac{1}{2\sqrt{r}} \sin \frac{\theta}{2} \\ \frac{\partial \psi_3}{\partial x_1} &= \frac{1}{2\sqrt{r}} \sin \frac{\theta}{2} (2 \sin^2 \theta - \cos \theta), \quad \frac{\partial \psi_3}{\partial x_2} = \frac{1}{2\sqrt{r}} \cos \theta (\cos \frac{\theta}{2} - 2 \sin \frac{\theta}{2} \sin \theta) \\ \frac{\partial \psi_4}{\partial x_1} &= \frac{1}{2\sqrt{r}} \cos \frac{\theta}{2} (2 \sin^2 \theta + \cos \theta), \quad \frac{\partial \psi_4}{\partial x_2} = \frac{1}{2\sqrt{r}} \cos \theta (\sin \frac{\theta}{2} - 2 \cos \frac{\theta}{2} \sin \theta) \end{aligned} \quad (\text{C.14})$$

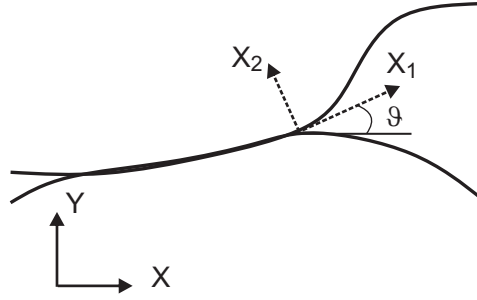


Figure C.3: Schematic view of the asymptotic fretting enrichment functions.

Finally, the derivative of the enrichment functions with respect to the global coordinate system  $(x, y)$  can be obtained by

$$\begin{aligned} \frac{\partial \psi_\alpha}{\partial x} &= \frac{\partial \psi_\alpha}{\partial x_1} \frac{\partial x_1}{\partial x} + \frac{\partial \psi_\alpha}{\partial x_2} \frac{\partial x_2}{\partial x} \\ \frac{\partial \psi_\alpha}{\partial y} &= \frac{\partial \psi_\alpha}{\partial x_1} \frac{\partial x_1}{\partial y} + \frac{\partial \psi_\alpha}{\partial x_2} \frac{\partial x_2}{\partial y} \end{aligned} \tag{C.15}$$

where  $\partial x_1/\partial x = \cos \vartheta$ ,  $\partial x_2/\partial x = -\sin \vartheta$ ,  $\partial x_1/\partial y = \sin \vartheta$  and  $\partial x_2/\partial y = \cos \vartheta$ , being  $\vartheta$  the angle between  $x_1$  (local coordinate system) and  $x$  (global coordinate system), Figure C.3.

# Appendix D

## Maximum Rectangular Hull (MRH)

Consider a rectangular geometry circumscribing the closed shear stress path given by  $\Theta$ , Figure D.1. This rectangle is tangent to the stress path  $\Theta$  at the points:

$$p_i = \max_t[\tau_i(\omega, t)], \quad i = 1, 2 \quad (\text{D.1})$$

and

$$q_i = \min_t[\tau_i(\omega, t)], \quad i = 1, 2 \quad (\text{D.2})$$

where both belong to the curve  $\Theta$ .  $\tau_i(\omega, t)$  represents the  $i^{\text{th}}$  component of the shear stress  $\underline{\tau}(t)$  projected on the plane  $\Delta$  in terms of a orthonormal basis oriented by an angle  $\omega$ , Figure D.1.

For each angle  $\omega$ , the amplitude of the  $i^{\text{th}}$  component of the stress history can be defined as:

$$d_i(\omega) = \frac{1}{2}(p_i - q_i) \quad (\text{D.3})$$

Therefore, the shear stress amplitude through the MRH can be defined as:

$$\tau_a = \max_w \sqrt{d_1(\omega)^2 + d_2(\omega)^2} \quad (\text{D.4})$$

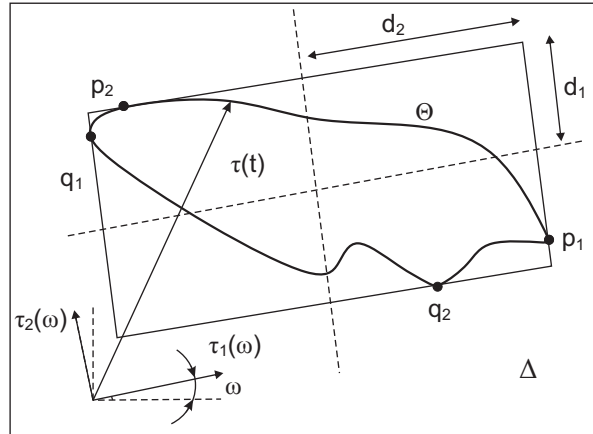


Figure D.1: Maximum Rectangular Hull (MRH) method.